

CLEAN SKY 2



JTI-CS2-2020-CFP11-THT-13: Sustainability of Hybrid-Electric Aircraft System Architectures



GAUGING THE ENVIRONMENTAL SUSTAINABILITY
OF ELECTRIC AIRCRAFT SYSTEMS

D2.1

Deliverable No.	GENESIS D2.1
Deliverable Title	Short-term technology analysis covering all main technologies in T2.1 - T2.6
Deliverable Date	30/11/2021
Version	1.0
Deliverable Type	Report
Dissemination level	Public
Link to scientific publication and/or repository	NA
Written By	Bruno Lemonie (BFH), Thomas Wannemacher (PMFC) Nils Baumann (PMFC), Alexe Guiguemde (MHT), Zhangqi Wang (ACC), Mario Distasio (UNINA), Manuela Ruocco (SMARTUP), Christian Bentheimer (FAU-LEE)

Checked by	Alexis Laurent (DTU), Karen Saavedra Rubio (DTU), Nils Thonemann (DTU)
Contact person	C.B. (christian.bentheimer@fau.de)
Status	Submitted
	 <p>This project has received funding from the Clean Sky 2 Joint Undertaking (JU) under grant agreement No 101007968. The JU receives support from the European Union’s Horizon 2020 research and innovation programme and the Clean Sky 2 JU members other than the Union. This deliverable only reflects the author's view; the JU is not responsible for any use that may be made of the information it contains.</p>

About project GENESIS

In a global context, where modern societies need to move towards more environmental sustainability, the aviation sector has an important role to play. Transition to reduce its environmental footprint (i.e., impacts on ecosystems, human health, and natural resources) stemming from activities in the entire value chain of aircraft has become high on political and industrial agenda. This transition must go hand in hand with the technological transformation of aircraft systems, moving away from the use of fossil-based fuels to alternative energy sources, like biofuels, hydrogen, or electricity via batteries.

Project GENESIS, funded by the EU Commission under the Clean Sky 2 Programme, aims to tackle some of these challenges. GENESIS stands for “Gauging the environmental sustainability of electric and hybrid aircraft”. Its main purpose is to develop a technology and sustainability roadmap to support the ambitions of the European aviation industry for transitioning towards environmentally sustainable and competitive electric and hybrid aircraft systems. Several powertrain technology alternatives are explored, including conventional, batteries, fuel cells and hybrid combinations of them, all with three time perspectives over the period 2025-2055.

Organized around a multidisciplinary and complementary expertise of its consortium members, GENESIS has the following key objectives (each reflecting the WP1-3 structure of GENESIS):

1. Develop a conceptual design, associated with top level aircraft requirements and scenarios, for all-electric and hybrid 50 PAX regional class aircraft.
2. Perform technology foresight analyses on key elements of the aircraft system, focusing on the powertrain architecture and energy storage alternatives.
3. Build life cycle inventories for each relevant technology process within the aircraft life cycle (from resource extraction, through manufacturing and use, up to end-of-life), and use them to perform prospective life cycle assessments of future aircraft system configurations and scenarios.

Overview and role of this deliverable within the GENESIS project

This document describes the short-term technology analysis for all main technologies in T2.1 - T2.6. GENESIS is an ambitious and innovative project that aims to gauge electric aircraft's environmental sustainability in a foresight perspective and provide a technology roadmap for a sustainable transition toward electric aircraft systems. The main task of WP2 is to perform technology foresight analyses on key elements of the powertrain structure and support systems in three time perspectives (short-term 2025-2035; medium-term 2035-2045, and long-term 2045-2055). This document focuses on the short-term (2025-2035) technology foresight evaluations for the powertrain components and the energy storage, including ground-based energy supply. The technology foresight analysis highlights knowledge gaps, technological challenges, and potential solutions to meet 50 passenger regional aircraft requirements. The analyses will feed back into the aircraft conceptual design for potential refinements. They will also serve as inputs for the generation of LCI data and economic evaluation.

Table of contents

Executive Summary	11
1. Introduction.....	13
1.1. Structure and objectives	13
1.2. Basic aircraft configuration and powertrain architecture	15
2. Battery technology analysis	19
2.1. Introduction	19
2.2. Electric and hybrid aircrafts	19
2.3. Historical evolution of Li-ion.....	20
2.4. Chemistries.....	20
2.5. Structure	22
2.5.1. Cell level	22
2.5.2. Battery pack level.....	22
2.6. Recycling methodology.....	23
2.7. Battery technology selection	23
3. Fuel cell technology analysis	25
3.1. Introduction	25
3.2. Technologies	25
3.2.1. Alkaline fuel cell - AFC.....	25
3.2.2. Direct methanol fuel cell - DMFC	25
3.2.3. Molten carbonate fuel cell - MCFC	26
3.2.4. Phosphoric acid fuel cell - PAFC.....	26
3.2.5. Solid oxide fuel cell - SOFC	26
3.2.6. Polymer electrolyte membrane fuel cells - PEMFC	26
3.3. Overview of the performances	33
3.4. Fuel cell technology selection	34
3.5. Hydrogen storage	35
3.5.1. Gaseous state storage	36
3.5.2. Liquid state storage	38
3.5.3. Solid storage - hydrides.....	39
4. Turbine / ICE generator set analysis	42
4.1. Introduction	42
4.2. Methodology	43
4.2.1. Pressure ratios	45
4.2.2. Polytropic efficiencies and basic flow path modelling	45
4.2.3. Cooling air requirement	49

4.2.4.	Miscellaneous input variables	51
4.2.5.	Dry mass calculation	52
4.2.6.	Main dimensions estimation	53
4.2.7.	Costs estimation	53
4.2.8.	Engine limitations	54
4.2.9.	Emissions	55
4.2.10.	Alternative fuels	56
4.3.	Validation and testing for the short-term scenario	57
4.3.1.	Validation.....	57
4.3.1.	Short-term scenario analysis	58
4.4.	Generation of a surrogate engine model.....	64
4.5.	Conclusions	66
5.	Power electronics technology analysis	67
5.1.	Introduction	67
5.2.	Choice of HV DC bus voltage.....	68
5.2.1.	Creepage and clearance distances	68
5.2.2.	Influence on power distribution cables	69
5.2.3.	Derating due to cosmic radiation	69
5.2.4.	Derating due to switch-off overvoltage	69
5.2.5.	Breakdown voltage ratings of power semiconductors	69
5.2.6.	Power electronics topology (multilevel converters vs. two-level converters).....	70
5.2.7.	Conclusion	71
5.3.	Choice of power semiconductors	71
5.4.	Motor and generator traction drive inverters.....	74
5.4.1.	Introduction.....	74
5.4.2.	Calculation of power losses	74
5.4.3.	Six-phase vs. three-phase motor and inverter configuration.....	76
5.4.4.	DC link capacitor	78
5.4.5.	Design analysis results for the motor and generator inverter systems.....	79
5.5.	Bidirectional battery DC/DC converter.....	83
5.6.	Unidirectional fuel cell DC/DC converter.....	86
5.7.	DC/AC grid converter	86
5.8.	Isolating DC/DC converter for low voltage supply.....	88
5.9.	Conclusions	91
6.	Electric drive technology analysis	92
6.1.	Introduction	92
6.2.	Configuration of primary and secondary drive train components.....	93

6.3. Design analysis results for the electric drive train	95
7. On-ground energy supply technology analysis.....	100
7.1. Introduction	100
7.2. Basic technologies for electric on-ground energy supply	100
7.3. Dimensioning of charging converters	103
7.4. Grid Topology	104
8. Conclusions and outlook.....	106
9. References.....	108

List of figures and tables

Figure 1. Electric architecture of a hybrid electric aircraft powertrain, with mapping of key technology components and supporting infrastructure to their respective partners in WP2.....	11
Figure 2. Overall methodology and interaction in the GENESIS project	13
Figure 3. Conceptual framework of GENESIS, with interconnections between specific objectives (SO)	14
Figure 4. Electric architecture of a hybrid electric aircraft powertrain, with mapping of key technology components and supporting infrastructure to their respective partners in WP2.....	14
Figure 5. Concept of NASA's X-57 Maxwell aircraft with distributed electric propulsion [2]	16
Figure 6. Powertrain and power electronics architecture for the short-term period (2025-2035) [3]	17
Figure 7. Power flow during the take-off phase [3]	17
Figure 8. Power flow during the climb phase [3].....	18
Figure 9. Power flow during the cruise phase [3].....	18
Figure 10. Histograms of specific energy for regional, narrow-body, and wide-body aircraft, illustrating the uncertainty stemming from aircraft design parameters. Larger (and longer-range) aircraft require a higher specific energy than do smaller (and shorter-range) aircraft	19
Figure 11: Li-ion cells shape – cylindrical (left), pouch (middle), and prismatic (right) [13]	22
Figure 12. Overview of the operating principle for different FC technologies [22]	25
Figure 13. Basic structure and typical hierarchy of a typical fuel cell application for any drive train	27
Figure 14. Basic components of a PEMFC stack	28
Figure 15. Design principles and typical materials PEMFC stack components	28
Figure 16. Typical scope of a PEMFC system with system boundaries in a target application.....	31
Figure 17. U/I characteristic or polarization curve of a fuel cell.....	33
Figure 18. Hydride and non-hydride forming elements in the periodic system of elements [54].....	40
Figure 19. PW127 engine configuration [57]	43
Figure 20. Radial compressor polytropic efficiency versus nondimensional specific speed and technology level according to [64] (left), and EIS correction according to [63] (right)	46
Figure 21. HP turbine normalized polytropic efficiency versus mean stage loading and technology level, derived from [63].....	47
Figure 22. LP and power turbine normalized polytropic efficiency versus mean stage loading and technology level, derived from [63].....	48
Figure 23. HP turbine EIS correction for polytropic efficiency, derived from [63].....	48
Figure 24. LP and free turbine EIS correction for polytropic efficiency, derived from [63]	48
Figure 25. HP turbine relative cooling air correction, as derived from [63]	49
Figure 26. Series of steps for the modelling of the flow path following the combustion chamber	49
Figure 27. Burner efficiency versus EIS, mainly according to [68].....	51
Figure 28. Engine dry mass linear regression law with respect to entry mass flow rate	52
Figure 29. Engine overall length linear regression with respect to shaft power.....	53
Figure 30. SFC contour plot for technology level 0.4 and 0 % biofuel blending ratio	59
Figure 31. Dry mass contour plot for technology level 0.4 and 0 % biofuel blending ratio	60
Figure 32. Maximum diameter contour plot for technology level 0.4 and 0 % biofuel blending ratio.....	60
Figure 33. Production cost (375 th engine) contour plot for technology level 0.4 and 0 % biofuel blending ratio	60
Figure 34. SFC contour plot for technology level 0.4 and 50 % biofuel blending ratio	61
Figure 35. SFC contour plot for technology level 0.4 and 100 % biofuel	61
Figure 36. SFC contour plot for technology level 0.6 and 0 % biofuel blending ratio	62
Figure 37. Dry mass contour plot for technology level 0.6 and 0 % biofuel blending ratio	63
Figure 38. Maximum diameter contour plot for technology level 0.6 and 0 % biofuel blending ratio.....	63
Figure 39. Production cost (375 th engine) contour plot for tech level 0.6 and 0 % biofuel blending ratio.....	63
Figure 40. SFC contour plot for technology level 0.6 and 50 % biofuel blending ratio	64
Figure 41. SFC contour plot for technology level 0.6 and 100 % biofuel blending ratio	64
Figure 42. Overview of possible power electronics converters for all time frames.....	67
Figure 43. Inverter legs of different inverter topologies: 2L, NPC-3L, ANPC-3L, and FLC-3L	70
Figure 44. Comparison of material properties.....	72
Figure 45. Calculation of voltage drop for bipolar and unipolar semiconductors	74
Figure 46. Three-phase topology with paralleled devices (top) and six-phase topology (bottom).....	76
Figure 47. Gate driver loop for three-phase configuration (left) and six-phase configuration (right)	77
Figure 48. Half-bridge DC/DC converter	83
Figure 49. Three times interleaved halfbridge DC/DC converter.....	83
Figure 50. DC/AC grid converter.....	86
Figure 51. LLC resonant converter.....	88

Figure 52. Phase-shifted full-bridge (PSFB) converter.....	89
Figure 53. Basis structure of the 10 kW isolating DC/DC converter for low voltage supply.....	89
Figure 54. Mechanical design of the 10 kW isolating DC/DC converter for low voltage supply with housing (top) and without housing (bottom).....	90
Figure 55. Overview of radial AC machines	92
Figure 56. Reuse of secondary electric drive train components to build up the primary electric drive train	94
Figure 57. Winding scheme of the secondary electric machine.....	98
Figure 58. Orientation of the permanent magnets inside the rotor (left) and mechanical design of the secondary electric machine without housing (right).....	98
Figure 59. Mechanical design of the secondary electric machine with housing and rotor shaft	98
Figure 60. Mechanical design of the primary electric machine as a stacked version of two secondary electric machines	99
Figure 61. Basic principle of an AC based grid	101
Figure 62. Basic principle of a DC based grid.....	101
Figure 63. Power supply with highlighted rectifying stage	102
Figure 64. Dual-Active-Bridge converter.....	104
Figure 65. LLC resonant converter	104
Figure 66. Overview grid topologies	105
Figure 67. GENESIS activities and time plan	107
Table 1. Summary of the main recommended technologies for the short-term perspective.....	12
Table 2. Partner contributions	15
Table 3. Power demand of powertrain components for different time frames [1].....	15
Table 4. Overview of battery chemistries [4] [10] [11] [12]	21
Table 5. Evolution of characteristics for Li-ion cells [19]	24
Table 6. Summary of the FCs' characteristics [23] [31] [32] [33] [34] [35]	33
Table 7. Hydrogen properties [41].....	35
Table 8. Hydrogen storage overview [42].....	35
Table 9. H2 content in different liquids under STP [53]	39
Table 10. Different technologies of material-based storage [42].....	39
Table 11. PW127E engine data	44
Table 12. Set of conditions for the design point.....	45
Table 13. Maximum limiting temperature assumptions for the calculation of the required amount of cooling air (assumed from [66] and [67]).....	50
Table 14. Cooling factor reference values (according to [65]) adopted to define a technological trend inside the GasTurb rubber engine model.....	50
Table 15. Lower and upper boundaries adopted for the modelling of pressure losses and spool mechanical efficiencies	51
Table 16. Lookup table for the burner efficiency.....	51
Table 17. Dataset used for the generation of the regression model for the engine dry mass	52
Table 18. Ratios for engine dimensions with respect to LP impeller and power turbine last stage diameters.....	53
Table 19. Set of mechanical limitations assumed for the analyses	54
Table 20. Set of temperature limitations assumed for the analyses.....	55
Table 21. Radial compressor limitations, taken from [64].....	55
Table 22. EI for CO ₂ , H ₂ O, and SO ₂ , according to [76].....	55
Table 23. Input values for the LHV and CO ₂ EI of the fuels examined for GENESIS, mainly derived from indications included in [77].....	56
Table 24. Set of input data to the rubber engine model for the PW127E engine.....	57
Table 25. Output cycle and derived variable results for the reference engine	57
Table 26. Obtained values for the main output variables for a gas turbine engine designed for the short-term scenario, assuming a value for the technology factor equal to 0.4 and a 0 % blending ratio for the adopted fuel	59
Table 27. Effect of alternative fuels on the fuel consumption for the short-term scenario, for a technology factor equal to 0.4	59
Table 28. Obtained values for the main output variables for a gas turbine engine designed for the short-term scenario, assuming a value for the technology factor equal to 0.6 and a 0 % blending ratio for the adopted fuel, with a comparative with respect to technology level 0.4 and the reference engine.....	62
Table 29. Effect of alternative fuels on the fuel consumption for the short-term scenario, for a technology factor equal to 0.6.....	62
Table 30. Input for the parametric study for the short-term scenario of GENESIS.....	65
Table 31. Training results for the surrogate engine model of the short-term scenario	65

Table 32. Power electronics components for the short-term period.....	68
Table 33. Altitude correction factor according to IEC EN60664.....	68
Table 34. Creepage and clearance distances for different HV DC bus voltages.....	69
Table 35. Minimum breakdown voltage ratings for different DC link voltages.....	70
Table 36. Suitable devices for different DC link voltages and converter topologies.....	70
Table 37. Comparison of material properties.....	71
Table 38. Comparison of Si MOSFETs, Si IGBTs, and SiC MOSFETs properties [89]	73
Table 39. Some examples for market available SiC MOSFETs with low on-resistance values.....	73
Table 40. Values for the scaling factor r_{max}	78
Table 41. Characteristics of half-bridge power module CAB760M12HM3 from Wolfspeed	79
Table 42. Results of technology analysis for secondary electric machine and inverter with 600 kW nominal power for short-term time frame (2025-2035)	80
Table 43. Results of technology analysis for primary electric machine and inverter with 1200 kW nominal power for short-term time frame (2025-2035)	81
Table 44. Key parameters of the 6-phase 600 kW inverter from Wolfspeed [96].....	82
Table 45: Summary of MOSFET losses.....	85
Table 46. Results of technology analysis for the DC/AC grid inverter.....	87
Table 47. Examples for 28V power demand for two regional aircraft	88
Table 48. Comparison between LLC and PSFB converter [100].....	89
Table 49. Key parameters of the 10 kW isolating DC/DC converter for low voltage supply	90
Table 50. Results of the technology analysis for all power electronics converters for the short-term horizon (2025-2035)	91
Table 51. Comparison of different AC machine types [101]	93
Table 52. Power demand of electric machines for different time frames	94
Table 53. Mechanical parameters for the secondary drive train for the short-term period (2025-2035)	96
Table 54. Mechanical parameters for the primary drive train for the short-term period (2025-2035).....	96
Table 55. Results of technology analysis for 6-phase secondary electric machine for the operating point “Take off” for the short-term period (2025-2035)	97
Table 56 Electrical parameters of the aircraft battery system	103
Table 57. Summary of the main recommended technologies for the short-term perspective.....	107

List of abbreviations

Abbreviation	Meaning
AC	Alternating Current
ACC	Accurec Recycling GmbH
AFC	Alkaline Fuel Cell
ANPC	Active Neutral Point Clamped
APU	Auxiliary Power Unit
ARMS	Ampere Root Mean Square
BEMF	Back Electromotive Force
BEV	Battery Electric Vehicle
BFH	Bern University of Applied Science / Berner Fachhochschule
BMS	Battery Management System
BPP	Bipolar Plate
CCM	Catalyst-Coated Membrane
CCM	Continuous Conduction Mode
CCS	Combined Charging System
CO	Carbon Monoxide
DAB	Dual Active Bridge
DC	Direct Current
DEP	Distributed Electric Propulsion
DMFC	Direct Methanol Fuel Cell
EI	Emission Index
EIS	Entry Into Service
EM	Electric Motor
EMC	Electromagnetic Compatibility
EMI	Electromagnetic Interference
ESL	Equivalent Series Inductance
ESR	Equivalent Series Resistance
EU	European Union
EV	Electric Vehicle
FAU-LEE	Friedrich Alexander University - Lehrstuhl für Leistungselektronik
FB	Full-Bridge
FC	Fuel Cell
FCCU	Fuel Cell Control Unit
FCEV	Fuel Cell Electric Vehicle
FHV	Fuel Heating Valve
FLC	Flying Capacitor
FT	Fischer-Tropsch
GDL	Gas diffusion layers
GENESIS	Gauging the ENvironmental Sustainability of electrIc aircraft Systems
GT	Gas Turbine
HC	Hydrocarbons
HDPE	High-Density Polyethylene

HEFA	Hydro-processed Esters and Fatty Acids
HMI	Human Machine Interface
HP	High Pressure
HV	High Voltage
ICE	Internal Combustion Engine
IEC	International Electrotechnical Commission
IGBT	Insulated-Gate Bipolar Transistor
IM	Induction Motor
IMSC	Induction Motor Squirrel Cage
IMSR	Induction Motor Slip Ring
IPMSM	Interior Permanent Magnet Synchronous Motor
ISA	International Standard Atmosphere
ISO	International Organization for Standardization
KOH	Potassium Hydroxide
LCA	Life Cycle Assessments
LCI	Life Cycle Inventories
LCO	Lithium Cobalt Oxide
LFP	Lithium Iron Phosphate
LHV	Lower Heating Value
LMO	Lithium Manganese Oxide
LNG	Liquid Natural Gas
LNO	Lithium Nickel Oxide
LP	Low Pressure
LT	Lithium Titanate
LTO	Lithium Titanate Oxide
LV	Low Voltage
MCFC	Molten Carbonate Fuel Cell
MCS	Megawatt Charging System
MEA	Membrane Electrode Assembly
MHT	MAHYTEC
MIE	Minimum Ignition Energy
MJ	Megajoule
MOF	Metal-Organic Framework
MOSFET	Metal Oxide Semiconductor Field-Effect Transistors
MPL	Microporous Layer
MTOW	Maximum Take-Off Weight
MW	Megawatt
NASA	National Aeronautics and Space Administration
NCA	Nickel Cobalt Aluminium
NCR	Nickel Cobalt Rechargeable
NGV	Nozzle Guide Vanes
NMC	Nickel Manganese Cobalt
NO _x	Nitrogen Oxides
NPC	Neutral Point Clamped

OCV	Open Circuit Voltage
OPR	Overall Pressure Ratio
PAFC	Phosphoric Acid Fuel Cell
PAX	Passenger
PEMFC	Polymer Electrolyte Membrane Fuel Cell
PFC	Power Factor Compensation
PLECS	Piecewise Linear Electrical Circuit Simulation
PMFC	Proton Motor Fuel Cell GmbH
PMSM	Permanent Magnet Synchronous Motor
PSFB	Phase-Shifted Full-Bridge
PT	Power Turbine
PWM	Pulse-Width Modulation
RM	Reluctance Motor
RMS	Root Mean Square
SEI	Solid Electrolyte Interphase
SESM	Separately Excited Synchronous Motor
SFC	Specific Fuel Consumption
SL	Sea Level
SMARTUP	Startup Engineering S.r.l
SOFC	Solid Oxide Fuel Cell
SPD	Shaft Power Delivered
SPK	Synthetic Paraffinic Kerosene
SPMSM	Surface Permanent Magnet Synchronous Motor
SRM	Switched Reluctance Motor
STP	Standard Temperature and Pressure
SynRM	Synchronous Reluctance Motor
T	Task
TLAR	Top-level Aircraft Requirements
TPRD	Thermally-Activated Pressure Relief Device
TRL	Technology Readiness Level
UAV	Unmanned Aerial Vehicles
UNINA	University of Naples Federico II
VDC	DC Voltage
VDS	Drain-Source Voltage
VRMS	Voltage Root Mean Square
WBG	Wide-Band gap
WP	Work Package
ZCS	Zero Current Switching
ZVS	Zero Voltage Switching

Executive Summary

The deliverable D2.1 “Short-term technology analysis covering all main technologies in T2.1 - T2.6” is a public document of the GENESIS project, produced in the context of Work Package 2 (WP2). GENESIS is an ambitious and innovative project that aims to gauge electric aircraft's environmental sustainability in a foresight perspective and provide a technology roadmap for a sustainable transition toward electric aircraft systems. The main task of WP2 is to perform technology foresight analyses on key elements of the powertrain structure and support systems in three time perspectives (short-term 2025-2035, medium-term 2035-2045, and long-term 2045-2055). This document focuses on the short-term (2025-2035) technology foresight evaluations for the powertrain components and the energy storage, including ground-based energy supply. The technology foresight analysis highlights knowledge gaps, technological challenges, and potential solutions to meet the requirements for a 50 passenger regional aircraft. The analyses will feed back into the aircraft conceptual design for potential refinements. They will also serve as inputs for the generation of LCI data and economic evaluation.

The electric architecture of a hybrid electric aircraft powertrain with all key technology components mapped to their respective partner and the supportive infrastructure needed during its operation is shown in Figure 1. Here, the system boundaries and interconnections between the aircraft powertrain, energy storage, and the ground-based energy supply components are highlighted.

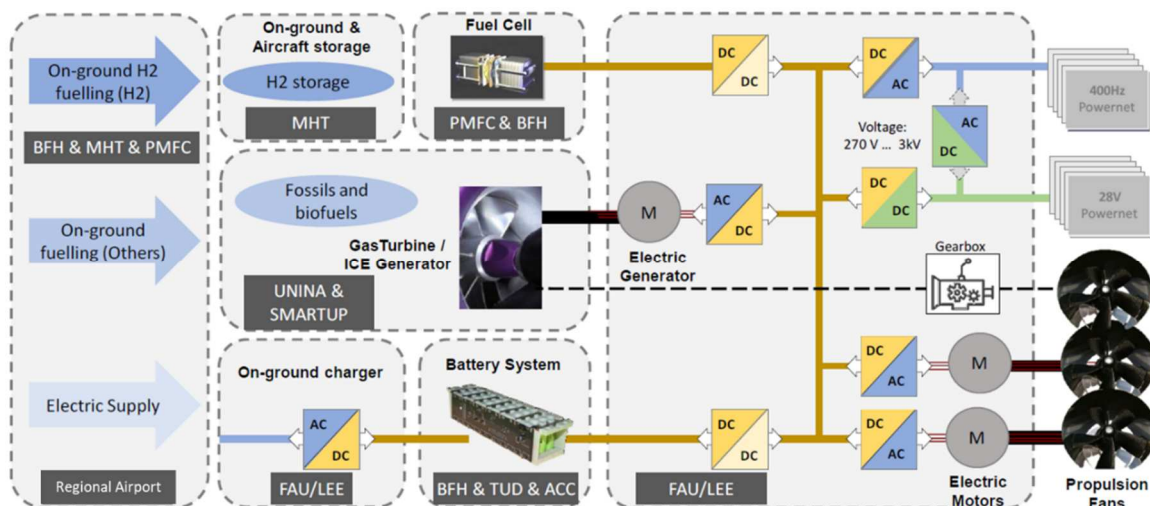


Figure 1. Electric architecture of a hybrid electric aircraft powertrain, with mapping of key technology components and supporting infrastructure to their respective partners in WP2

Each chapter of the deliverable is dedicated to one key element in the aircraft powertrain. Chapter 2 presents the battery technology analysis investigating different chemistries, battery structures, and recycling possibilities. Li-ion batteries with nickel manganese cobalt oxide (NMC) chemistry are found to be the primary solution. The energy density is expected to rise from 280 Wh/kg in 2025 to 400 Wh/kg in 2035, allowing a significant weight reduction over the years. However, that is lower than the needed energy density of 600 Wh/kg for a fully electric aircraft in the regional class. Therefore, a hybrid electric solution with a gas turbine is needed for the short-term perspective. Chapter 3 focuses on the fuel cell technology analysis, and six different fuel cell types are compared. Solid oxide fuel cells (SOFCs) and polymer electrolyte membrane fuel cells (PEMFCs) are the two most promising candidates. However, with a power density of 0.86 kW/kg, they lay below the minimum value of 2 kW/kg at which fuel cells can be utilized for an aircraft application. Fuel cell technology is not ready yet and will not be incorporated for the short-term analysis. Furthermore, the required hydrogen storage will also add a mass penalty for the tank (e.g., 2.15 tons for 150 kg of

gaseous hydrogen) to the aircraft. In this regard, different hydrogen storage possibilities in the gaseous, liquid, and solid state are also discussed in Chapter 3. Chapter 4 is centered on gas turbine engines and provides a rubber model and a surrogate model for a gas turbine engine for the short-term scenario with performance, emissions, weight, main dimensions, and cost evaluation. Validation of the model is also provided. Chapter 5 includes technology analysis for all power electronics converters. First, the choice of the HV DC bus voltage and power semiconductors is discussed. The voltage was set to 800 V and it was illustrated that silicon carbide wide-bandgap power semiconductors should be used for all power electronics converters. Then all converters, i.e., motor and generator traction drive inverter, bidirectional battery DC/DC converter, fuel cell DC/DC converter, DC/AC grid converter, and isolated DC/DC converter for low voltage supply are investigated in detail. For each converter type, the efficiency and power density values were determined. Chapter 6 explores the topic of electric drives. First, different types of AC machines are compared with the result that the permanent magnet synchronous machine (PMSM) is the best option for the short-term horizon. Furthermore, a possible design of the primary and secondary electric machines is presented. Finally, Chapter 7 describes the possibilities of the on-ground energy supply, focusing on the electric on-ground energy supply and ultra-fast DC charging stations. It is recommended to use a DC-based distribution grid in a (zonal structured) ring topology. The DC ultra-fast chargers need to provide a maximum output power of 780 kW, and they will be built with silicon carbide-based building blocks of 100 kW power. Table 1 shows a summary of the recommended main technologies for all key technology components for the short-term perspective.

Table 1. Summary of the main recommended technologies for the short-term perspective

Key technology components	Recommended main technologies for the short-term perspective	Main technical parameters and values
Batteries (Task 2.1)	Li-ion with nickel manganese cobalt oxide (NMC) chemistry	Energy density: 280 Wh/kg in 2025 to 400 Wh/kg in 2035
Fuel cells (Task 2.2)	None (power density too low)	Actual power density: 0.86 kW/kg Needed power density: > 2 kW/kg
Gas turbines (Task 2.3)	Conventional gas turbine sized according to the application with usage of up to 100 % biofuel	Fuel consumption: 0.23 kg/(kW*h) Dry mass: 285 kg Maximum diameter: 608 mm
Power electronics converters (Task 2.4)	Silicon carbide (SiC) power semiconductors, foil capacitors, multi-phase/interleaved topologies	HV DC bus voltage: 800 V Inverter efficiency: $\approx 99\%$ Inverter power density: 63 kW/kg
Electric drives (Task 2.5)	Multiphase permanent magnet synchronous machine (PMSM) with hairpin winding	Efficiency: $\approx 96\%$ Total power density: 6.4 kW/kg Mass for 600 kW motor: 86.5 kg
On-ground infrastructure (Task 2.6)	DC-based distribution grid in a (zonal structured) ring topology, silicon carbide-based DC fast charges	DC charging power: 2x 780 kW

1. Introduction

1.1. Structure and objectives

GENESIS is an ambitious and innovative project that aims to gauge electric aircraft's environmental sustainability in a foresight perspective and provide a technology roadmap for a sustainable transition toward electric aircraft systems. The project is structured in three work packages (WP). WP1 deals with basic concepts and requirement analysis. WP2 is centered on the performance of technology foresight analyses on key elements of the powertrain structure and support systems in three time perspectives (short-term 2025-2035, medium-term 2035-2045, and long-term 2045-2055). WP3 will build life cycle inventories (LCI) and provide prospective life cycle assessments (LCA). Figure 2 illustrates the key methodology aspects and the interactions between the work packages.

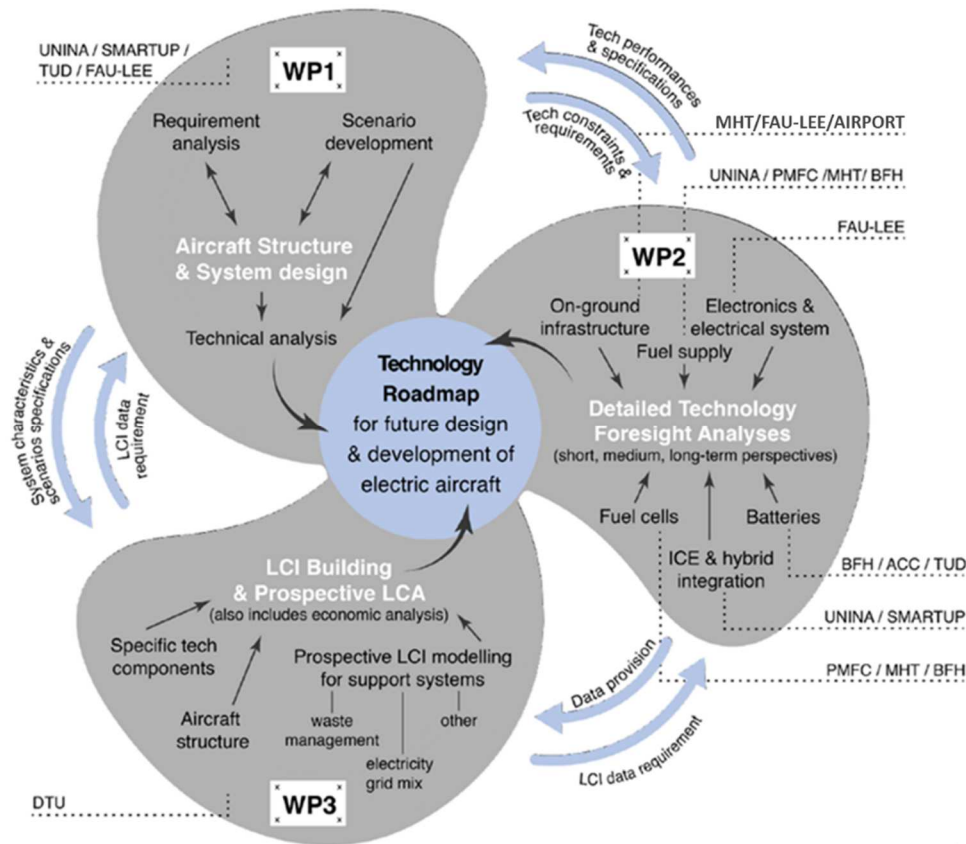


Figure 2. Overall methodology and interaction in the GENESIS project

Figure 3 provides an overview of the conceptual framework that interconnects the seven specific objectives (SO) of the GENESIS project. WP2 addresses SO-3, i.e., technology foresight analyses will highlight knowledge gaps, technological challenges, and potential solutions to meet 50 passenger regional aircraft requirements. The analyses will feed back into the aircraft conceptual design for potential refinements. They will also serve as inputs for the generation of LCI data (materials extraction, production, use, recycling, and disposal) and economic evaluation.

This deliverable D2.1, produced in the context of WP2, specifically focuses on the short-term (2025-2035) technology foresight evaluations for the powertrain components, energy storage, and on-ground energy supply. WP2 consists of six specific tasks (T2.1 to T2.6), each dealing with a technological key component of the electric aircraft system (batteries, fuel cells, gas turbines, power electronics, electric drives, and on-ground infrastructures).

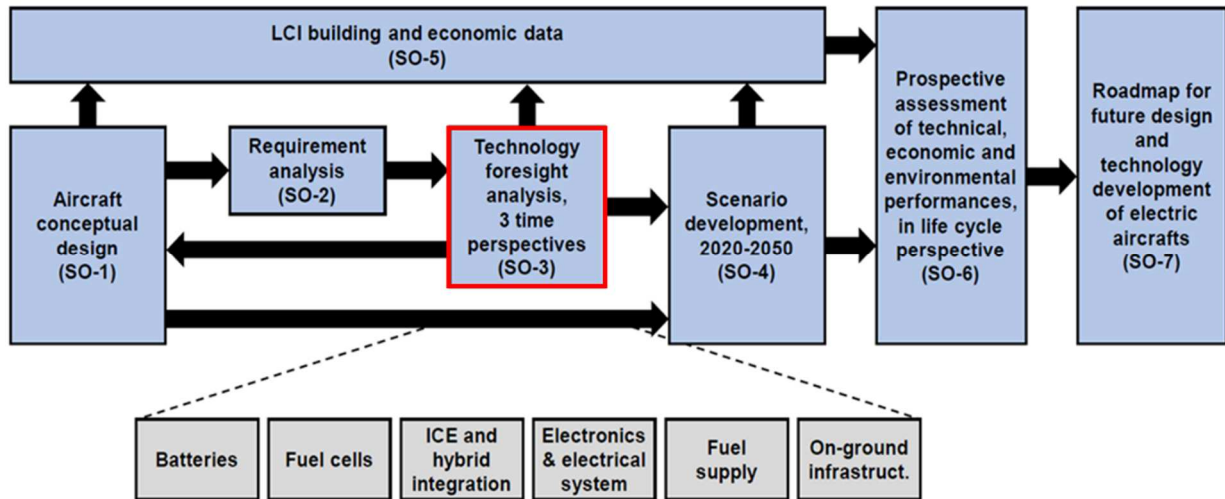


Figure 3. Conceptual framework of GENESIS, with interconnections between specific objectives (SO)

The electric architecture of a hybrid electric aircraft powertrain with all key technology components mapped to their respective partner and the supportive infrastructure needed during its operation is shown in Figure 4. Here, the system boundaries and interconnections between the aircraft powertrain, energy storage, and the ground-based energy supply components are highlighted.

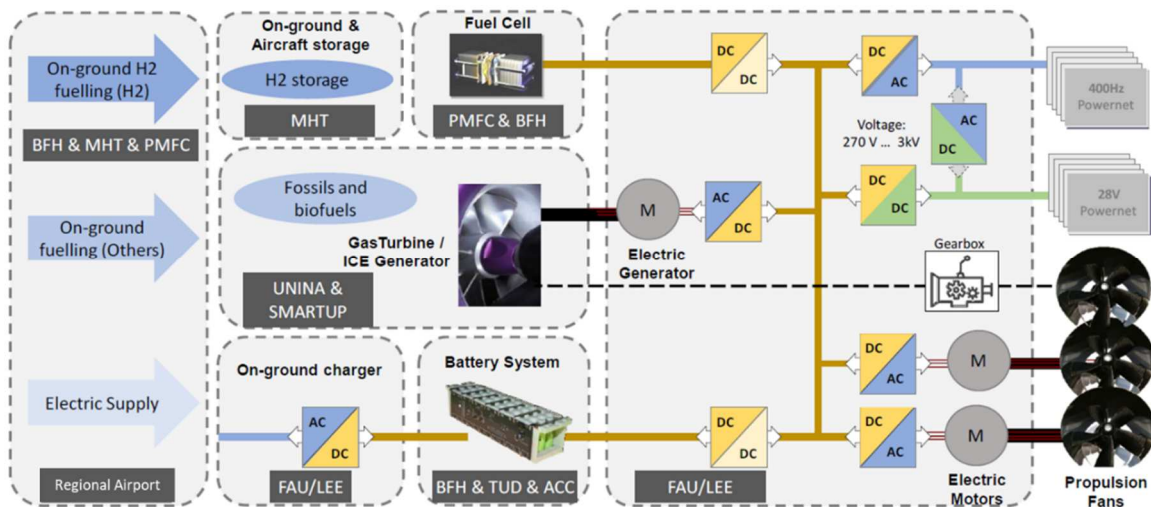


Figure 4. Electric architecture of a hybrid electric aircraft powertrain, with mapping of key technology components and supporting infrastructure to their respective partners in WP2

Each chapter of the deliverable is dedicated to one specific task and key element in the aircraft powertrain. Chapter 2 presents the battery technology analysis (task 2.1), investigating different chemistries, battery structures, and recycling possibilities. Chapter 3 focuses on the fuel cell technology analysis (task 2.2), and six different fuel cell types are compared. Hydrogen storage possibilities in the gaseous, liquid, and solid state are also discussed. Chapter 4 is centered on gas turbine engines (task 2.3) and describes an approach to model a gas turbine engine for the short-term scenario regarding performance emissions, weight, main dimensions, and costs. Validation of the model is also provided. Chapter 5 includes technology analysis for all power electronics converters (task 2.4). First, the choice of the HV DC bus voltage and power semiconductors is discussed. Then all converters, i.e., motor and generator traction drive inverter, bidirectional battery DC/DC converter, fuel cell DC/DC converter, DC/AC grid converter, and isolated DC/DC converter for low voltage supply are investigated in detail. Chapter 6 explores the electric drives (task 2.5) and provides a design

of the primary and secondary electric machines. Finally, Chapter 7 describes the possibilities of the on-ground energy supply (task 2.6), focusing on the electric on-ground energy supply and ultra-fast DC charging stations. Chapter 8 provides a conclusion and gives an outlook. Table 2 shows the contributions of all partners with the corresponding authors.

Table 2. Partner contributions

Chapter	Topic	Author (Partner)
1	Introduction	Christian Benteimer (FAU-LEE)
2.1 - 2.5, 2.7	Battery chemistries and structure	Bruno Lemonie (BFH)
2.1	Battery recycling methodology	Zhangqi Wang (ACC)
3.1 - 3.4	Fuel cell technologies	Bruno Lemonie (BFH)
3.2.6	PEM fuel cells	Thomas Wannemacher (PMFC), Nils Baumann (PMFC)
3.5	Hydrogen storage	Alexe Guiguemde (MHT)
4	Turbine / ICE generator set	Mario Distasio (UNINA), Manuela Ruocco (SMARTUP)
5.1-5.4, 5.6-5.9	Power electronics converters	Christian Benteimer (FAU-LEE)
5.5	Battery DC/DC converter	Michael Renner (FAU-LEE)
6	Electric drives	Christian Benteimer (FAU-LEE)
7.1	Introduction for on-ground energy supply	Christian Benteimer (FAU-LEE)
7.2 – 7.4	On-ground energy supply	Kilian Gosses (FAU-LEE)
8	Conclusions and outlook	Christian Benteimer (FAU-LEE)

1.2. Basic aircraft configuration and powertrain architecture

In the GENESIS deliverable D1.1, the basic top-level aircraft requirements (TLAR) for a hybrid electric 50 passenger regional class aircraft were defined. The requirements for the powertrain components are shown in Table 3. A safety margin for unpredicted mass penalties and assumptions about technology level was applied. For the short-term horizon (2025-2035), there will be two gas turbines and no fuel cell system. For the medium-term and long-term time frames, a fuel cell system and a bigger battery pack will be implemented to replace the gas turbines [1].

Table 3. Power demand of powertrain components for different time frames [1]

Powertrain Component	Number of units	Reference Power in kW		
		Short-Term Year 2025-2035	Medium-Term Year 2035-2045	Long-Term Year 2045-2055
Gas turbine	2	2400	0	0
Fuel cell system	2	0	1800	1400
Battery pack	2	550	1100	2000
Primary electric machine	2	1200	1200	1500
Secondary electric machine	8	600	600	750

In deliverable D1.1, it was concluded that for the short-term horizon, an architecture with distributed electric propulsion (DEP) and tip-mounted propellers is the most promising solution for the aircraft design [1]. The same configuration is also used in the NASA X-57 Maxwell technology demonstrator (see Figure 5). For the short-term time frame in the GENESIS project, the regional aircraft will have four small high lift motors (secondary electric machines) under each wing. These motors are only used during the take-off phase. At each wing tip, there is a big cruise motor (primary electric machine) that is used in all flight situations.

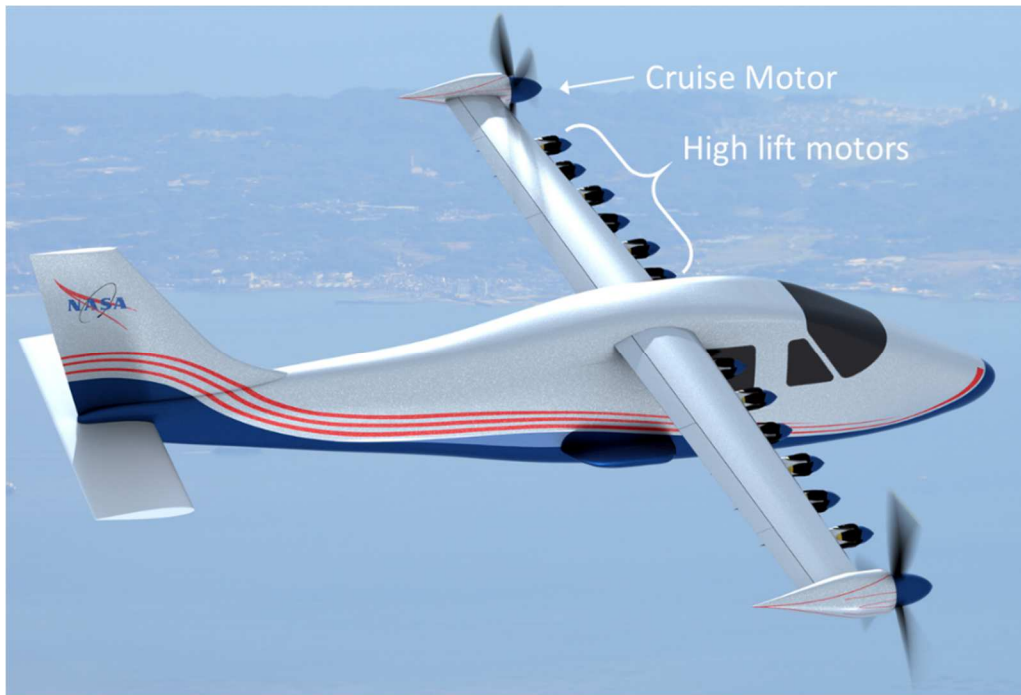


Figure 5. Concept of NASA's X-57 Maxwell aircraft with distributed electric propulsion [2]

For the electric powertrain, a serial/parallel partial hybrid configuration was chosen [1]. Figure 6 shows the basic aircraft configuration with the powertrain and power electronics components derived from the top-level aircraft requirements (TLAR) for the short-term period 2025-2035. It contains all existing power electronics systems and machines for one-half of the aircraft. The aircraft is symmetrically built, so the other half of the aircraft is identical. More details about the different power electronics converter and their function can be found in Chapter 5.

Figure 7 to Figure 9 show the power distribution and power flow during the take-off, the climbing, and the cruise phase. The power flow diagrams show that the electrical power coming from the battery system enters a bidirectional battery DC/DC converter, which transfers power from the battery with a maximum voltage of 1170 V to the internal 800V DC bus. From here, the DC/AC grid converter and the isolating DC/DC converter supply the 400 Hz and 28 V power nets, respectively. During take-off (see Figure 7), power is also transferred from the 800 V DC bus via the motor traction drive inverters to the electric motors, which will convert the electrical power into mechanical power to move the secondary propulsion fans. For the short-term perspective, the latter are only used during the take-off phase. The mechanical power of the gas turbine is delivered to a gearbox, which drives the primary propulsion fan. In the take-off phase (Figure 7), the gas turbine also drives the electric generator via the gearbox. In this case, the generator traction drive inverter supplies the electric energy from the generator to the internal 800V DC bus by rectifying the AC voltages. In the climb and cruise phase, the generator is used as a motor and electric energy from the battery system is also used to drive the main propulsion fan via the generator drive inverter and the battery DC/DC converter.

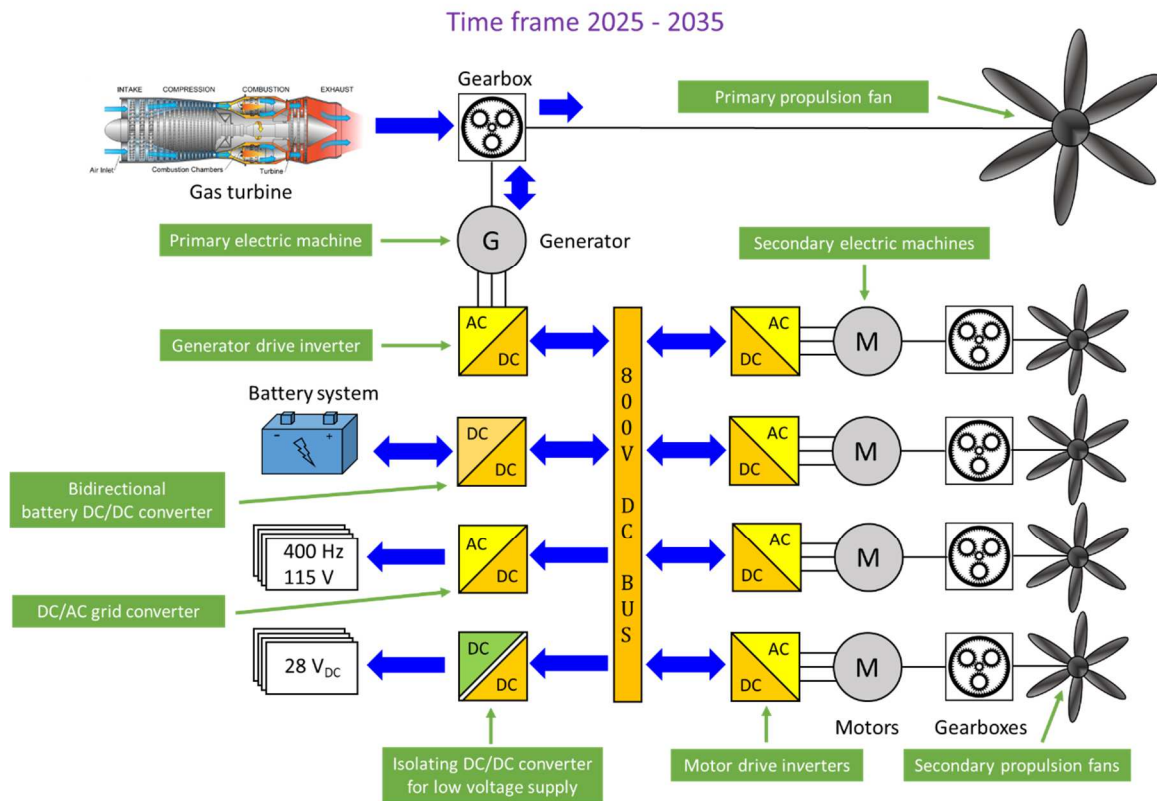


Figure 6. Powertrain and power electronics architecture for the short-term period (2025-2035) [3]

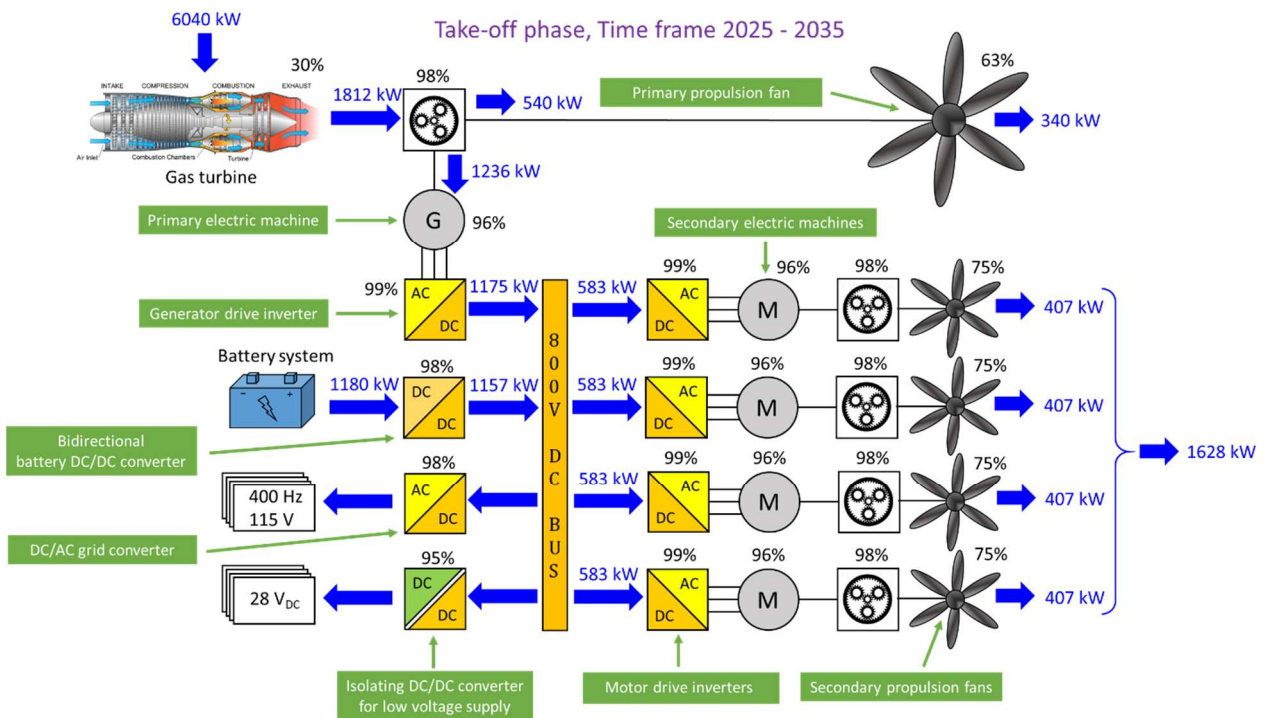


Figure 7. Power flow during the take-off phase [3]

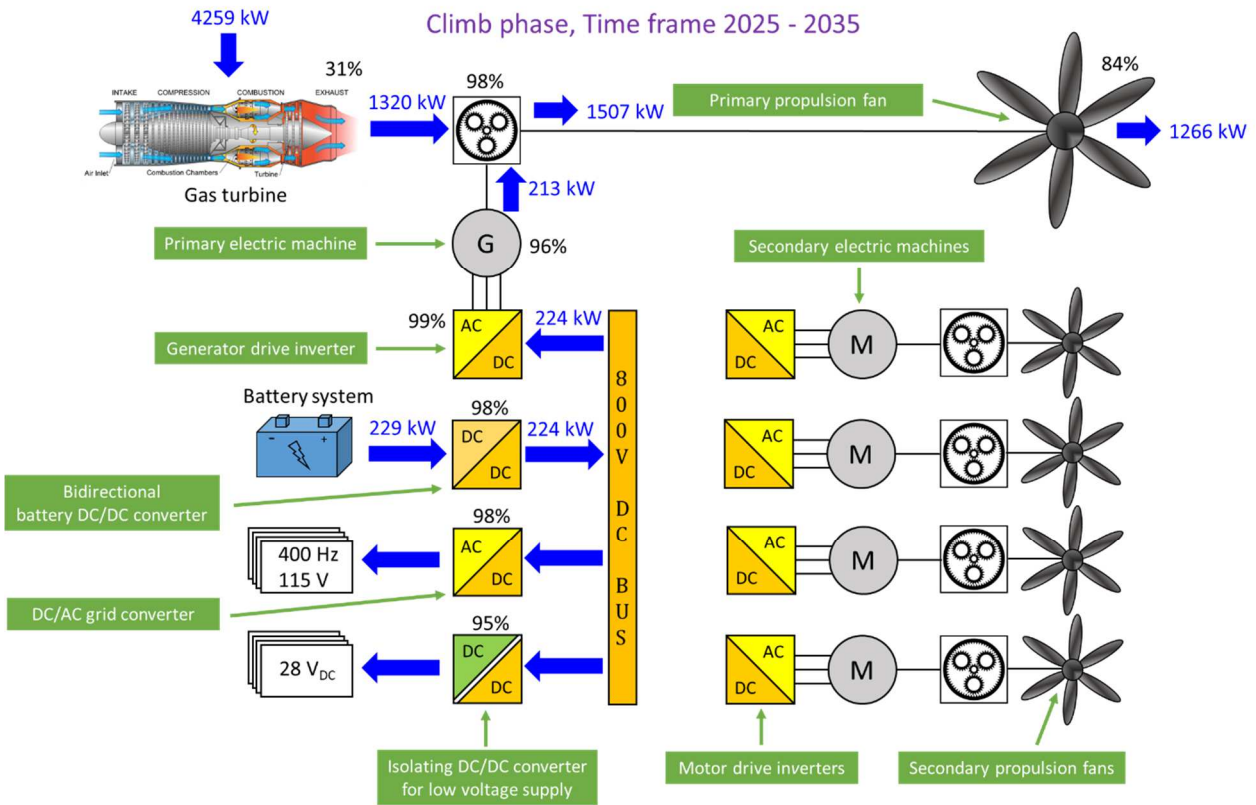


Figure 8. Power flow during the climb phase [3]

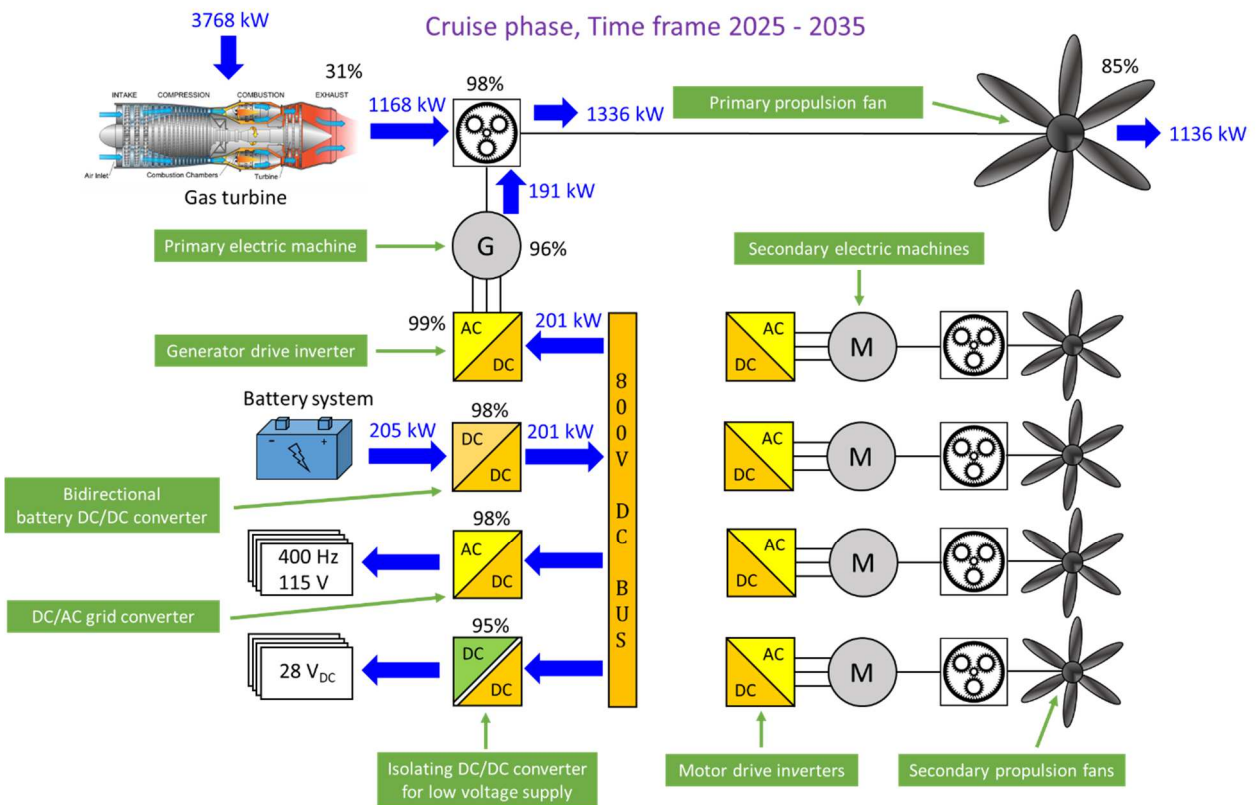


Figure 9. Power flow during the cruise phase [3]

2. Battery technology analysis

2.1. Introduction

Batteries are the enabler of the energy transition from fossil fuel to renewable energy. Almost every energy sector in the future will rely on this storage system to match the stochastic production to consumption and decrease the carbon footprint in everyday life. Since batteries, primarily lithium-ion-based (Li-ion) batteries, are currently the key component of the energy transition, there is a significant scientific and technological interest to push the development of this technology towards higher range, fast-charging ability, longer lifetime, and improved safety [4]. The widespread use of aircraft in both military and civilian applications have led the aeronautic field to be responsible for over 2.4% of the total fossil emissions in 2018 [5]. Energy sustainability is greatly needed, and therefore, the potential environmental benefits of hybrid electric regional aircraft have been assessed frequently (e.g., by J. Bogaert [6]). It was reported that in the case of an ATR72-600 capable of carrying 68 passengers, the implementation of a hybrid design could provide a 28% reduction in fuel mass and thus, decrease drastically the overall impact of the global aeronautic industry.

2.2. Electric and hybrid aircrafts

Initially, academics focused on unmanned aerial vehicles (UAVs) to validate and demonstrate the feasibility of the hybrid technology. The first investigations started in 2005 in UC Davis with a 13.6 kg UAV and a maximum take-off weight (MTOW) of 20 kg. Then, the research extended towards small hybrid aircraft for niche applications. For example, Ampaire EEL is a project from 2019 that developed a hybrid power airplane featuring a 180 kW electric motor and allows carrying a MTOW of 2100 kg. In both applications, the vast majority of the prototypes featured a hybrid system composed of an internal combustion engine (ICE) and an electric motor (EM). Typically, lithium-ion batteries were used thanks to their high energy density.

Nowadays, the focus lies in the transfer of knowledge from these projects to regional airliners. It is already known in literature that the batteries energy density necessary to enable electric aviation should be higher than 600 Wh/kg. According to Schäfer and co-authors, a lower-end battery pack specific energy requirement of 800 Wh/kg is needed for an Airbus A320 or Boeing 737-sized aircraft capable of 600 nautical mile (nmi) missions [7].

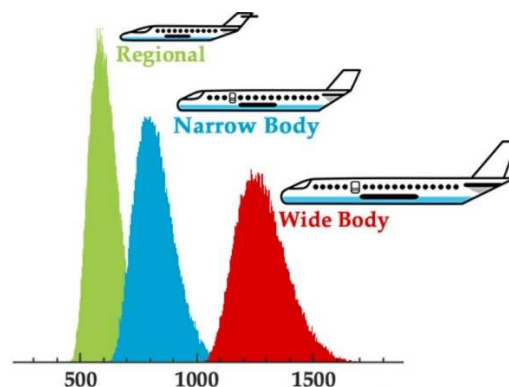


Figure 10. Histograms of specific energy for regional, narrow-body, and wide-body aircraft, illustrating the uncertainty stemming from aircraft design parameters. Larger (and longer-range) aircraft require a higher specific energy than do smaller (and shorter-range) aircraft ¹

¹ Reprinted with permission from “Performance Metrics Required of Next-Generation Batteries to Electrify Commercial Aircraft”, Bills et al. Copyright 2020 American Chemical Society

Recently, Bills and others [8] have differentiated the energy demand of battery energy densities based on three flight categories. Regional (30 passengers, 350 nmi range), narrow-body (150 passengers, 500 nmi range), and wide-body (300 passengers, 1000 nmi range) aircraft are considered. The energy density mean is about 600 Wh/kg for regional aircraft, 820 Wh/kg for narrow-body aircraft, and 1280 Wh/kg for wide-body aircraft (see Figure 10).

2.3. Historical evolution of Li-ion

Li-ion battery is a generic term that regroups batteries that use lithium as a charge carrier, and they show fundamental advantages over other chemistries. First, lithium has the lowest reduction potential, enabling Li-ion batteries to have the highest possible cell potential. Second, lithium is the third lightest element, allowing Li-ion batteries to reach high gravimetric and volumetric density. Third, Li-ion batteries also have the highest coulombic efficiency (CE) ratings in rechargeable batteries (above 99 %). CE describes the proportion of the total electric charge that is delivered by the battery to the total electric charge put into the battery over a complete cycle. Finally, a significant shortage of lithium is unlikely [9].

For all these reasons, Li-ion batteries are nowadays replacing lead-acid or nickel-based batteries in many applications. However, the concept of Li-ion battery was demonstrated in the early 1970s by Whittingham, and many different chemistries have since been developed to reach the current state of the art of Li-ion technology. The first single transition metal oxide battery lithium cobalt oxide (LiCoO₂: LCO) was successfully commercialized in 1991 by Sony [9]. LCO batteries show good performances, but they suffer from poor thermal stability and must be monitored during operation to ensure safe use. Lithium nickel oxide (LiNiO₂: LNO) was also a promising material for high voltages thanks to its lower cost of materials and high theoretical capacity. However, the formation of a self-passivation layer at the surfaces causes some significant issues. Finally, lithium manganese oxides (LiMn₂O₄: LMO) show low internal resistance, enabling fast charging and high currents. LMO also provides better thermal stability than LCO but, the capacity decreases by approximately 33%, and the lifetime is also reduced. To counteract specific drawbacks of each chemistry, the last decade has seen a growing interest in mixed transition metal cathodes, which combine technologies such as LMO and LNO to optimize the performances.

2.4. Chemistries

Different battery chemistries are associated with widely varying performances such as energy density and cycle life. As a result, the chemistry must be chosen according to requirements of applications to optimize battery usage [10]. For example, the improvements in terms of specific energy are driven by electric vehicle (EV) manufacturers, searching for more space- and weight-efficient batteries. Li-nickel manganese cobalt oxide (NMC) and Li-nickel cobalt aluminum (NCA) chemistries are nowadays the bests towards increasing energy density at an affordable cost. The highest specific energy batteries commercially available are NCA batteries, such as the Panasonic NCR18650A cells in current Tesla battery packs [11]. At the same time, NMC innovators are trying to realize a low-cobalt cathode. Indeed, cobalt is the source of many battery issues as it is an expensive material, and it has a significant environmental impact. Moreover, cobalt mine production and reserves are located mainly in Congo, raising questions about political stability and working conditions. First versions of NMC alloys were designed to contain one-third of each material (nickel, manganese, and cobalt). Researchers then decreased the proportion of cobalt and developed the NMC811 chemistry, which means that the alloy is composed of 80 % nickel, 10 % manganese, and 10 % cobalt. However, since cobalt acts as a battery stabilizer, low-cobalt chemistries tend to sacrifice stability and cycle life for cost and range improvements.

Regarding cycle life, it is known that fast charging and temperature strain have significant impacts on Li-ion batteries' lifetime. Li-iron phosphate (LFP) and Li-titanate (LTO anode coupled with an NMC cathode) show good cycle life. Still, they are not the main focus of recent manufacturing additions, as the cycle life comes at the expense of specific energy and cost. Most anodes are currently made of carbon (e.g., graphite) or LTO with some novel materials under development [4]. LTO anodes feature high discharge rate capability and better stability, while graphite ones have a higher specific capacity [Ah/kg].

A suitable combination of negative and positive electrode materials leads to a cost-effective and high-capacity battery. Indeed, the cell capacity is dictated by the specific capacity of both electrode materials in the cell. Table 4 describes the main characteristics of varying battery chemistry currently available on the market.

Table 4. Overview of battery chemistries [4] [10] [11] [12]

Chemistry Li-ion	Nickel Manganese Oxide NMC	Nickel Cobalt Aluminium Oxide NCA	Iron Phosphate LFP	Titanate Oxide LTO	Cobalt Oxide LCO	Manganese Oxide LMO
Nominal voltage [V]	3.70	3.60	3.3	2.40	3.60	3.70–3.80
Minimal voltage [V]	2.50	2.50	2.00	1.50	2.50	2.50
Specific energy [Wh/kg]	240	260	120	80	150–200	100–150
Cycle life	1000–2000	1000	1000–3000	5000-10'000	500–1000	300–700
Operational temperature range [°C]	[5:35]	[50:35]	[0:50]	[-40:50]	[0:30]	[5:35]
Temperature of thermal runaway [°C]	210	150	270	One of the safest batteries	150	250

The battery degradation mechanism also deeply influences key characteristics, which causes capacity loss and resistance increase over the lifetime. Battery degradation can be a severe problem in the automotive or aircraft industry affecting the vehicle's warranty period and compromising the reputation of the sector. Hence, fundamental understanding of degradation mechanisms is critical for developing reliable life-prediction methods for battery management systems (BMS).

Identifying the ageing mechanism in a Li-ion battery is the primary and most challenging goal. With a predictive control of battery degradation into BMS, more realistic power limits can be calculated so that the battery is optimally used (degradation limited) and not oversized. This can be realized by controlling the charge or discharge current for an application that can minimize degradation (e.g., solid electrolyte interphase (SEI) growth or lithium plating, among other physical phenomena).

2.5. Structure

2.5.1. Cell level

In addition to the chemistry, the shape of the battery cell has a significant impact on the performance and design of the battery pack. Three different formats are currently available on the market and can be seen in Figure 11.



Figure 11: Li-ion cells shape – cylindrical (left), pouch (middle), and prismatic (right) [13]

Cylindrical cells are popular thanks to their low cost, high energy density, and good mechanical stability. Standard sizes are available such as “18650” cells (18 mm in diameter and 65 mm in length). However, but the industry is currently shifting to “21700” cells (21 mm in diameter and 70 mm in length) to reduce the number of cells needed inside a battery pack, and therefore, increase the energy density of the overall battery pack. New development plans have been announced with the production of even bigger cells “4680” (46mm in diameter and 80 mm in length) by Tesla and Panasonic [14].

Prismatic cells use the volume more efficiently while being easier to handle and to assemble into battery packs. However, they are more expensive, difficult to manage thermally, and no standard sizes are available [15].

Finally, pouch cells are a minimalistic approach to packaging. The active material is simply stacked on top of each other and sealed by a flexible aluminium foil. This approach increases the packaging density and saves weight while allowing a large variety of shapes. The main drawbacks are that pouch cells do not offer safety features, standard sizes and are more sensitive to temperature cycles. Additionally, the automation of the production is more difficult which lead to higher costs.

2.5.2. Battery pack level

The battery manufacturing process usually goes from cell to module and then from module to pack [16]. This intermediate step divides the battery into separate and independent modules regrouping their battery management and diagnostic systems. Therefore, malfunctioning of the cells can be handled at the module level and facilitate the replacement of individual packs. The trade-off resides in additional terminal plates and internal connectors that account for additional volume and weight. Indeed, the cell usually accounts between 60 to 77% of the weight of the battery and thus, battery manufacturers are looking intensively to increase the volume and weight utilization of battery packs [17].

With this idea in mind, BYD Auto released a new product called “Blade battery”, increasing space utilization by 50 % (going from 40 to 60 %). Unlike conventional prismatic cells, the length of the blade battery is exceptionally long while the depth and height are short. These blades allow producing a battery pack composed of individual cells and skip the module step of the production. However, this innovation comes along with new challenges like a complex battery manufacturing process. In addition, other popular solutions can involve using bigger modules to reduce the number of interconnections and thus, save weight, and volume [18].

2.6. Recycling methodology

After reaching the end of life, the whole battery pack of the aircraft needs to be recycled. The volume of the aircraft battery pack is much larger than the conventional Li-ion batteries from laptops and EVs. The battery pack needs to be discharged and dismantled to a smaller size for further treatment. After size reduction, the batteries can be treated by conventional Li-ion battery recycling processes.

The current status of the Li-ion battery recycling process is composed of deactivation process, separation process, and metallurgical recovery process. The deactivation process can be carried out either thermally or mechanically. During thermal deactivation, batteries are heated up to 600°C. Organic components such as electrolytes and separators are evaporated or pyrolyzed. Without the electrolyte and separator, the mobility of Li-ion is limited, and thus, the cells are deactivated. In the mechanical deactivation process, the cell components are shredded under a controlled environment, such as an inert atmosphere or underwater, and then the electrolyte is separated. As a result, the cells are deactivated.

After deactivation, different components are separated for further recovery. The thermally deactivated cells are shredded and then separated using a multi-step sieving process and a magnetic separator. The outputs of these processes are the ferrous, the copper-aluminium (Cu/Al), and the black mass fractions. The separation process used afterward for the mechanically deactivated cells depends on the conditions applied during the deactivation process. When water is used during the deactivation process, the black mass fraction is immersed in solution while the big particles such as ferrous, separator, and Cu/Al foil can be separated by sieving. The black mass will be separated from the electrolyte-containing solution by filtration. When inert gas is used during the deactivation process, the electrolyte is evaporated and collected, and then the different components are separated by the dry separation process, which is similar to the one used for thermally deactivated cells.

The separated components are delivered to the corresponding recycling plants for further metallurgical recovery. The ferrous fraction is considered as waste iron. It is delivered to the iron smelter for iron recovery, the Cu/Al fraction is given to the copper smelter for copper recovery, and depending on the metal concentration, price as well as the location of subsequent process, the black mass is delivered to the cobalt and/or nickel smelter for cobalt and nickel recovery. In the end, all these components and materials will be used and produced again in the primary production processes.

2.7. Battery technology selection

Concerning the short-term perspective (2025-2035), the main limitations of batteries are their low energy and power densities compared to conventional fuels. These shortcomings are shared with the EV industry, and improvements in batteries are mainly pushed by the EV manufacturers thanks to the high-volume market of EVs.

Currently, the NMC and NCA chemistries are the leading choices for EVs. Both chemistries show very similar performances, characteristics, and degradation behavior. Nevertheless, NMC batteries are currently the focal point of the research due to the significant improvements in reducing the amount of cobalt which greatly improves the environmental and economic aspects. Therefore, NMC batteries are looking to be the primary solution for electric aircraft applications in the short-term horizon. The performance of Li-ion batteries has been increasing significantly in the last twenty years. Additionally, more research and development resources are allocated every year to improve the performance of these batteries as the demand grows exponentially. Table 5 shows the expected evolution of the characteristics for Li-ion batteries from 2020 to 2035.

Table 5. Evolution of characteristics for Li-ion cells [19]

Timeline	2020	2025	2030	2035
Expected specific energy [Wh/kg]	250	280	330	400
Expected specific power [W/kg]	500	560	660	800
Expected energy density [Wh/l]	550	650	750	950

3. Fuel cell technology analysis

3.1. Introduction

On the way to carbon neutrality, the airline industry proves to be a particularly difficult segment to decarbonize due to the inherent need for energy-dense fuels. Hydrogen has long been hailed as the future fuel for this application due to its high gravimetric energy density, almost three times that of kerosene [20]. Additionally, recent advances in materials science allowed Fuel Cells (FCs) to be designed with fewer moving parts and higher efficiencies and thus, to be considered as a viable option for powering electric aircraft.

3.2. Technologies

The Fuel cell terminology regroups every system “that converts the chemical energy of a fuel and oxidizing agent into electricity through a pair of redox reactions” [21]. Therefore, plenty of different FC systems have been developed over the years and are usually categorized by the type of electrolyte used in the system. Further classifications are established according to the purity level of the fuel and oxidant used or the working temperature. Figure 12 provides an overview of different FCs, including their types of fuels, oxidants, charge carriers, and operational temperature ranges.

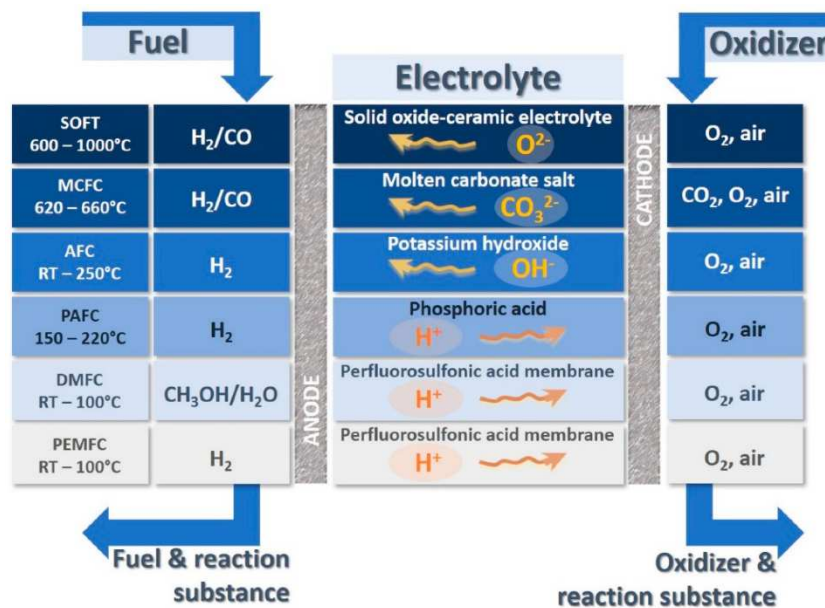


Figure 12. Overview of the operating principle for different FC technologies [22]

The main categories of FCs are briefly described below [23].

3.2.1. Alkaline fuel cell - AFC

AFCs employ alkaline electrolytes, mainly potassium hydroxide (KOH) diluted in water. They operate with pure hydrogen fuel, pure oxygen as oxidant, and mainly at low temperatures (60-90°C) while reaching an efficiency of up to 60 %. The main disadvantages rely upon the corrosiveness of the electrolyte and the carbon dioxide poisoning, referring to the adsorption of carbon dioxide by KOH, thus, reducing the conduction power of the electrolyte [24].

3.2.2. Direct methanol fuel cell - DMFC

DMFCs use a polymer membrane as an electrolyte and are often classified as a sub-category of polymer electrolyte membrane FCs (PEMFCs) because of their similar design and configuration.

They operate at low temperatures (60-130°C) and use fuels different from hydrogen. The main difference with PEMFC is that the waste product includes carbon dioxide. The main disadvantage is that they show the lowest efficiency (<40%) among fuel cells [24].

3.2.3. Molten carbonate fuel cell - MCFC

MCFCs employ molten carbonate salt as an electrolyte such as lithium or potassium carbonate [23]. They operate at high temperatures (~650°C) and have an efficiency of ~60 %. Furthermore, the efficiency can be significantly improved when the waste thermal energy is harnessed in a co-generation system to achieve ~80 %. The main disadvantage is its durability due to the electrolyte degradation attributed to the high operating temperature and the corrosive environment [25].

3.2.4. Phosphoric acid fuel cell - PAFC

PAFCs use liquid phosphoric acid as an electrolyte and operate at medium temperatures (150-200°C). The fuel-to-electricity efficiency is relatively low at 35 to 45 %, but higher values can be reached with combined heat and power applications. However, overall, the efficiency is found to be lower than other FC technologies. Other issues involve a heavy and expensive system due to the integration of corrosion-resistant components to mitigate the effect of the acid electrolyte [24] [25].

3.2.5. Solid oxide fuel cell - SOFC

SOFCs employ a nonporous “solid ceramic” electrolyte such as zirconium oxide stabilized with yttrium oxide and operate at high temperatures (600-1000°C). The oxygen air is fed to the positive electrode, and the mobility of the ions is initiated by the nonporous solid ceramic. Water is formed through the reaction at the negative electrode [23] [25].

The efficiency reached can be above 60 %, which comes close to the theoretical thermodynamic efficiency of 75 % [26]. Similarly, to MCFCs, the residual energy from the unused fuel and hot exhaust air can be harnessed by a gas-turbine-generator system to boost the system efficiency up to 85 % with co-generation. Additionally, the high-temperature process in SOFC allows direct internal reforming, which provides opportunities in using different kinds of fuels such as biogas or natural gas without the need for a noble catalyst. One of the main challenges with this technology is high-temperature corrosion which can be mitigated using an expensive protective layer [25].

Only recently, SOFC's have started to be considered as a viable power source option for aircraft. As a result, the research dedicated towards the development of SOFCs, to increase the power densities and efficiencies has raised. It was the 2nd most cited R&D topic in 2014 in the field of FC [27]. Additionally, many recent studies have started to address the replacement of auxiliary power units (APUs) in commercial airplanes by implementing SOFC gas turbine (SOFC-GT) systems [28]. However, no prototypes have yet been developed.

3.2.6. Polymer electrolyte membrane fuel cells - PEMFC

As described in the previous chapter, PEMFCs, or more precisely LT-PEMFCs (low temperature PEMFCs), are typically fueled with pure hydrogen and oxygen from ambient air at temperatures below 100 °C².

A complete fuel cell system as part of the power supply system or powertrain of an electric powered vehicle including air vehicles such as planes but also drones, ships etc. consists of the plain PEMFC stack, and additionally of several components for the so-called balance of plant (BoP) that support the stack. This includes an air module typically with a compressor, air filters and an intercooler to provide reaction air, a hydrogen circuit with a hydrogen supply unit and recirculation pump, a thermal management unit with heat exchangers and pumps dissipate reaction heat. Furthermore, usually power electronics for DC/DC conversion and a fuel cell control unit (FCCU) are necessary. This

² PEMFC with temperatures higher than 100 °C are high temperature (HT) systems. The corresponding technology is slightly different, usually those systems are used as residential μ -CHP operated with natural gas and a reformer unit.

structure of a PEMFC can be seen in Figure 13 and will be described in this chapter (as marked in the blue box, the components outside are described in the following chapters). A comprehensive overview of components and production is given in [29].

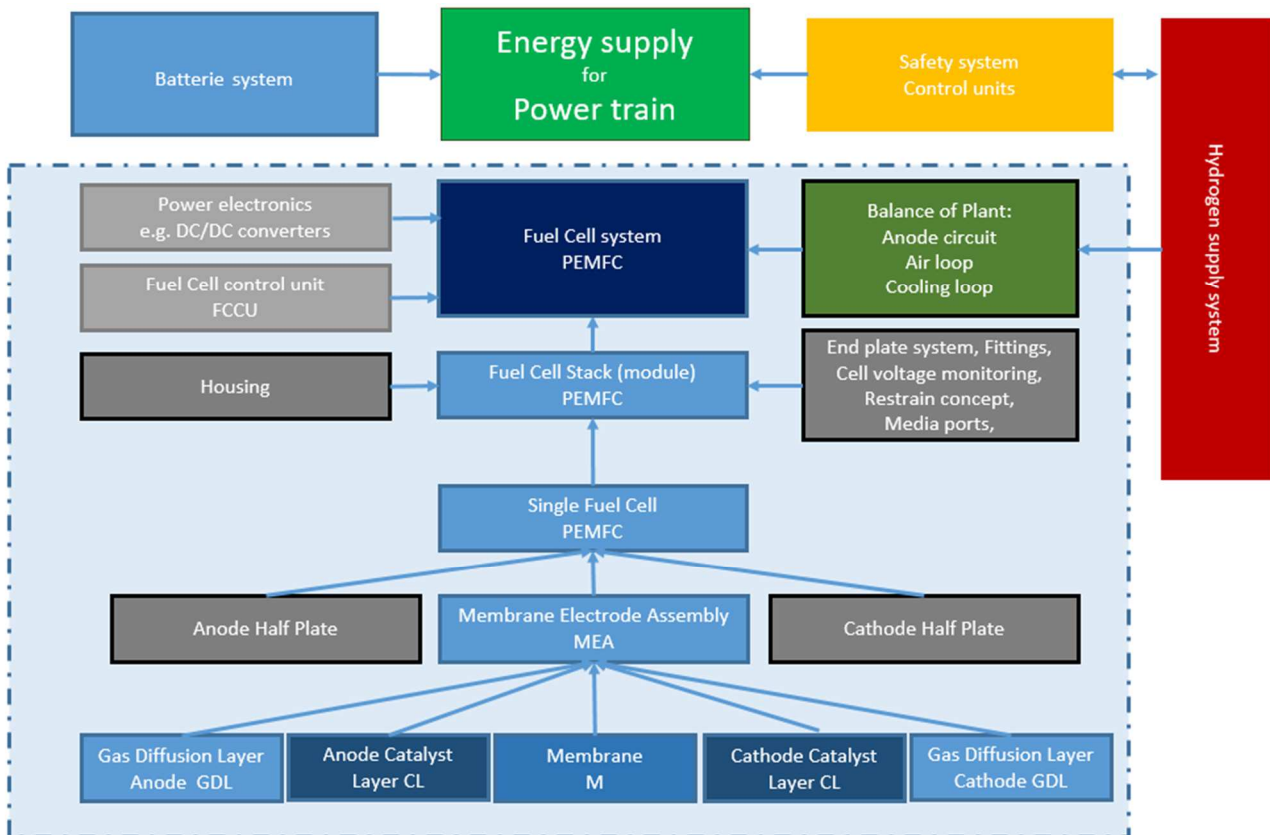


Figure 13. Basic structure and typical hierarchy of a typical fuel cell application for any drive train

The main feature of a PEMFC stack and also of the entire system is naturally its specific power. This depends largely on the size of the active cell area and the number of individual cells in the stack. In addition, the efficiency of the BoP and the power electronics also have a significant impact on the power of the overall system. Furthermore, the overall efficiency can be significantly increased beyond the purely electrical efficiency by using the waste heat. Additionally, the specific operating point of the PEMFC system also plays a major role.

Generally speaking, the output current of the stack is determined by its so-called active area of the cell. This refers to the part of the cell surface where the catalytic conversion of hydrogen and (atmospheric) oxygen takes place. In addition, the cells can also have areas that do not contribute to the reaction but are necessary for the supply and removal of the reaction media.

Since all cells within a PEMFC stack are electrically connected in series, the current in all cells is the same. Through the number of cells connected in series, the total voltage and thus the stack performance can be influenced and easily adapted to the framework conditions of the application. In addition, by connecting several stacks in series in a system, an even higher total power can be achieved.

A single cell consists of a so-called bipolar plate (BPP) with an anode and a cathode side, two gas diffusion layers (GDL) and a catalyst-coated membrane (CCM) between the GDLs. Normally, the CCM and GDL form the membrane electrode assembly (MEA). In addition, for safe and efficient operation, sufficient compression of the PEMFC stack must be ensured. To ensure uniform pressure

distribution within the cell stack as well as gas tightness, a suitable restraint system or clamping concept must be applied. This is shown in the following Figure 14.

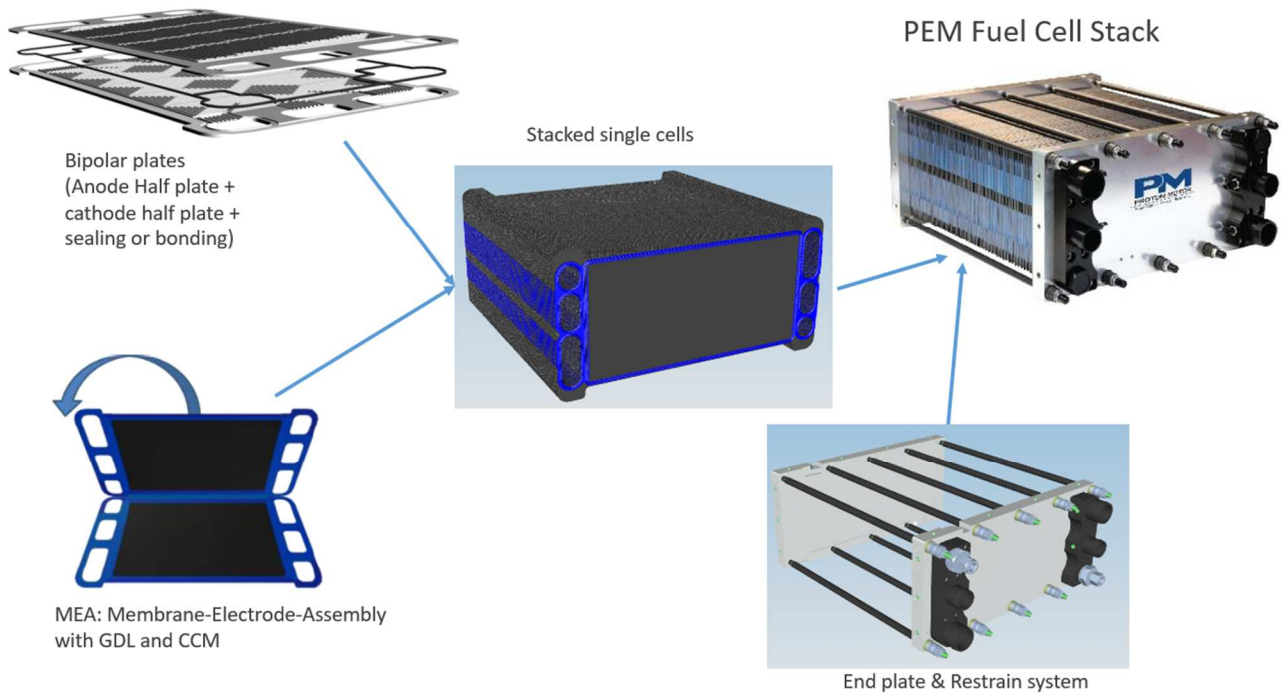


Figure 14. Basic components of a PEMFC stack

For the concrete implementation of the PEMFC stack itself, a variety of different design principles and concepts are available, which are also widely implemented in the market. In addition, a wide variety of component materials and concepts can be carried out for achieving the specific requirements of the individual applications (see Figure 15).

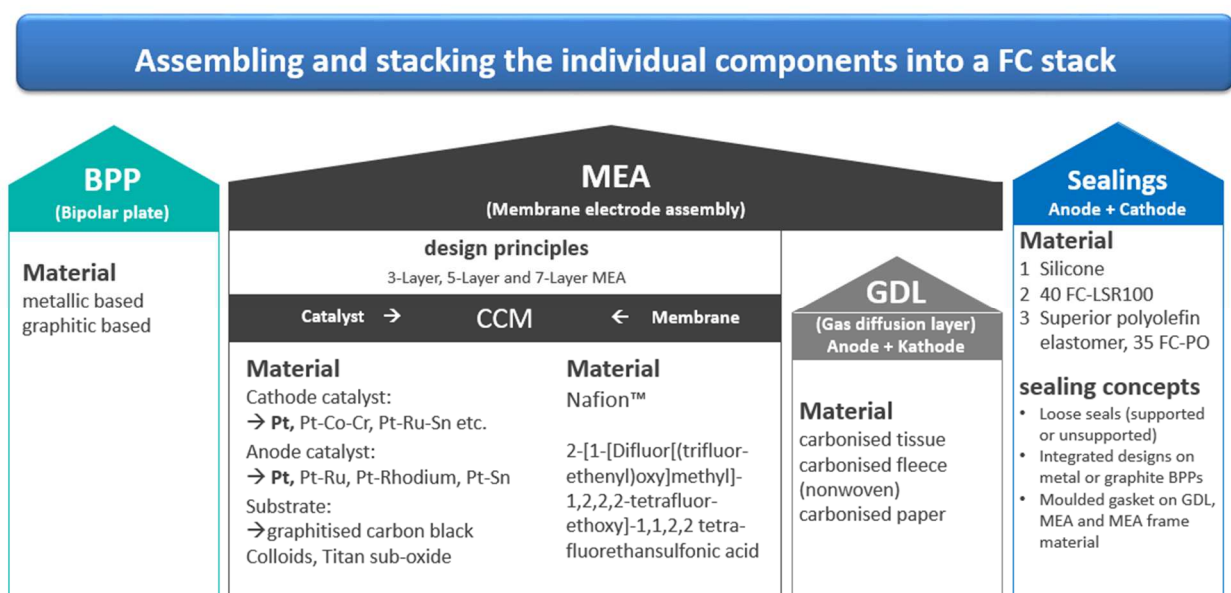


Figure 15. Design principles and typical materials PEMFC stack components

The core components of the LT-PEMFC are described below:

A) Bipolar plate (BPP)

The main tasks of the bipolar plates are the supply of the reaction gases to the electrochemically active layer, the removal of the reaction products, and the conduction of the produced current (electrons). In addition, the cooling of the cell by dissipating the heat of reaction is an important task to prevent overheating. These tasks are realized through channels of the so-called flow fields. The BPP usually contains an anode flow field for the supply of hydrogen, the cathode flow field for the supply of oxygen/reaction air and an intermediate cooling flow field in the case of liquid cooling³. As seen in Figure 15 often BPP are made from two half plates, which have to be bonded or joined or sealed.

The main distinguishing feature of PEMFCs is the bipolar plate concept (BPP). There are two fundamentally different concepts on the market, which in turn can be designed in a variety of different forms and material compositions:

- a) metal-based BPP
- b) graphite-based BPP

The specific concept has a considerable influence on the installation space and the service life of the PEMFC stack, which is briefly discussed below. More details can be found in [30].

On the one hand, graphite-based bipolar plates with a long lifetime of >15'000 to 20'000 operating hours are available. Their decisive disadvantage is a significantly lower volumetric power density due to their considerably higher thickness.

Metal-based BPPs, on the other hand, are much thinner and can therefore offer a higher volumetric power density. However, their lifetime is much shorter, only about 5'000 to 6'000 hours.

Both technologies have their specific advantages and disadvantages, and it is therefore essential to carefully select the most suitable technology for the application in question in advance.

However, this current state of the art is subject to constant further development of the components, and it is to be expected that especially in this area there will be a lot of potential (for both technologies) in the future.

B) Gas diffusion layer (GDL)

The GDL is the link between the CCM, where the chemical reaction takes place, and the bipolar plate, which is responsible for media supply and removal of the reaction products (also electricity and heat). The main task of the gas diffusion layer is to feed the reaction gases to the directly adjacent catalyst layer and to remove the reaction products (mainly water). In addition, electrical conduction and heat dissipation are of course equally important. This is achieved by a highly porous layer of carbonized paper, non-woven or woven fabric. Often GDLs are equipped with a hydrophobic treatment and a so-called microporous layer (MPL) between the GDL layer and the catalyst layer.

Due to their tasks of conducting both reaction media and electrical current to and from the CCM, a dilemma arises. On the one hand, the structure should be as highly porous and thus permeable as possible. On the other hand, electrical conduction in solid structures is subject to significantly lower ohmic losses. Therefore, especially for the GDL, the correct compression and pressure distribution in the fuel cell stack is important.

³ Usually, stacks with a power >3 kW are liquid cooled.

C) Catalyst coated membrane (CCM)

The CCM consists of a polymer electrolyte membrane and a catalyst layer on the anode and cathode side. The ionomer material has the task of guiding the protons generated from the hydrogen molecule on the anode side to react with the oxygen (from the air) on the catalyst layer on the cathode side. In addition, the material must be largely impermeable to gas and electrically insulating to minimize crossover of the gases and prevent an electrical short circuit. Nafion[®]-type polymers⁴ meet these requirements and are therefore frequently used. For good proton conduction, it is important that the membrane is saturated with as much liquid water as possible. In addition, a reinforcement of PTFE against mechanical stress is usually incorporated.

As described, a catalyst layer is applied to the surface of both sides of the membrane layer. Nowadays, these usually consist of a platinum catalyst on a carbon carrier. The task of this catalyst is to enable the electrochemical reactions by dissociating the molecules of the reactants hydrogen and oxygen on the surface of the catalyst into their corresponding ions. On the anode side, the hydrogen molecules are split into protons and electrons; on the cathode side, the protons are recombined with the electrons and oxygen from the air ($\text{H}_2 \rightarrow 2 \text{H}^+$; $\text{O}_2 \rightarrow 2 \text{O}^{2-}$).

Besides pure water, only waste heat is produced, which must be dissipated to prevent damage to the membrane.

For all these individual components, there are already a large number of commercially available products with a high degree of technical maturity available on the market today.

Through a clever selection, the PEMFC can also be tailored to the specific requirements of the respective application.

The continuous further development of these core components is the subject of major scientific and industrial research, and it is therefore to be expected that the next few years will see a significant increase in performance and lifetime, a reduction in dimensions and weight, and a drastic reduction in production costs.

These will be achieved not only through improvements in the selected materials, but also by increasing production volumes with the appropriate processes.

D) Balance of plant (BoP)

As shown before, beside the PEMFC stack itself, which is a kind of chemical reactor for converting chemical energy into electricity, a certain amount of additional components is needed. Usually, this process engineering and electrical conversion equipment is called balance of plant (BoP). This part requires a certain volume and weight and must not be forgotten when planning the fuel cell system into the target application, especially when space and weight requirements are restricted. In the following, the main components that are typically needed to operate a fuel cell will be briefly described. In the following Figure 16 a rough overview of a typical PEMFC system for an electric drive train is given as it is used at the project partner PROTON MOTOR.

⁴ Nafion[®] is a brand name of DuPont. CAS-No.: 31175-20-9; Systematic name: Ethanesulfonyl fluoride, 2-[1-[difluoro-[(trifluoroethenyl)oxy]methyl]-1,2,2,2-tetrafluoroethoxy]-1,1,2,2,-tetrafluoro-, with tetrafluoroethylene

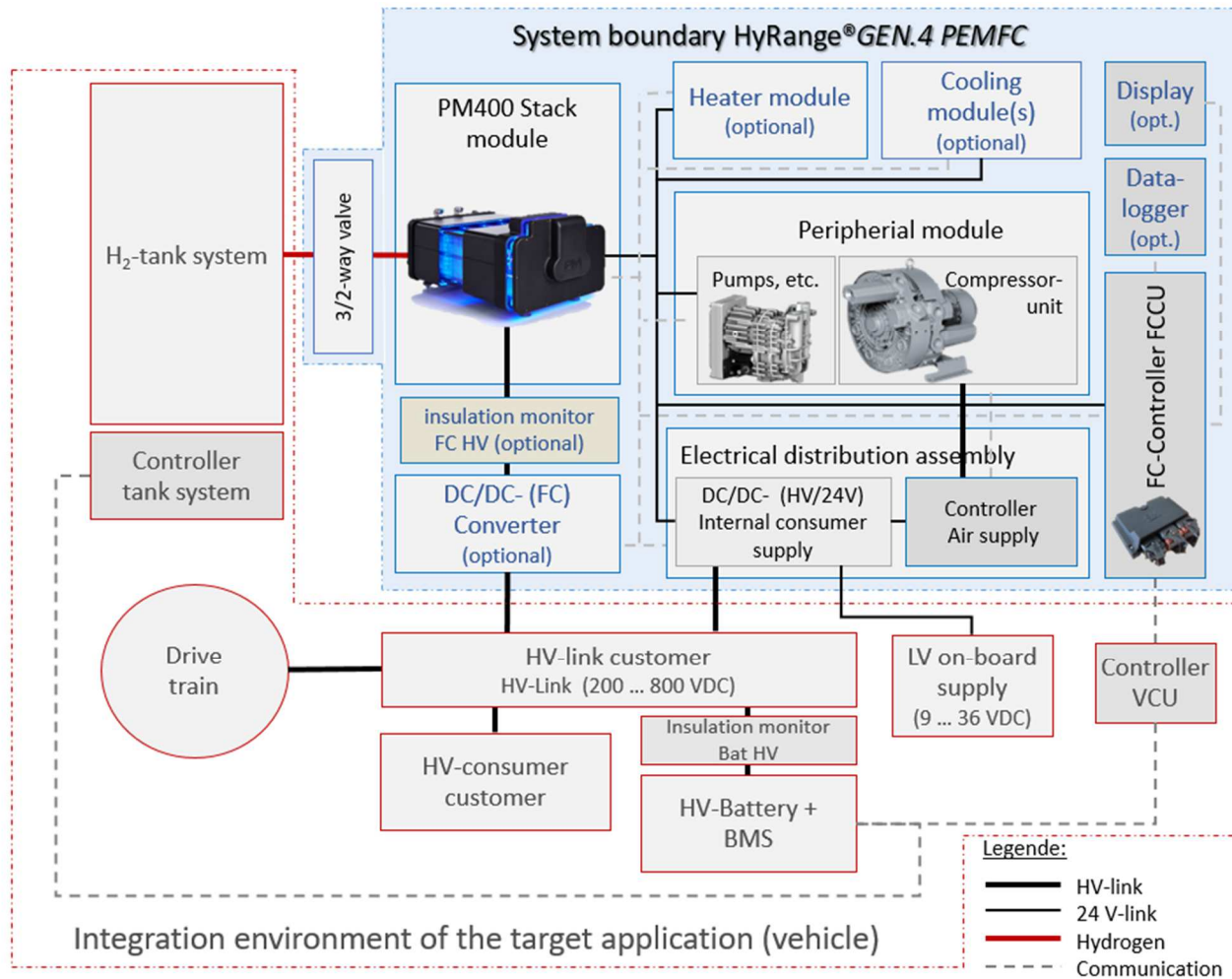


Figure 16. Typical scope of a PEMFC system with system boundaries in a target application

The peripheral components of the PEMFC (see blue frame) can be described according to the media processing loops.

E) Anode loop

The fuel cell is supplied with hydrogen fuel from a suitable tank system (as described in the following Chapter 3.5). In addition to the piping to the fuel cell, the intersection to the PEMFC is an inlet valve and a pressure reducer to reduce the tank pressure to the pressure level of the PEMFC. This can also be done via several pressure stages. H₂ inlet pressures are usually below 3 bar_g, often even below 1 bar_g, depending on the specific design. In addition to the hydrogen feed, the hydrogen loop often includes a recirculation pump to feed the hydrogen in a closed loop, as well as a water separator and a purge valve to remove accumulating inert gases (N₂) from the loop.

F) Reaction air and water processing

To supply the fuel cell with an adequate amount of reaction air, an air compressor (in case of smaller systems a blower may be sufficient) is typically used. To cool this reaction air to a moderate level, an intercooler may be necessary. As the interface to the air supply of the PEMFC, there is usually also an air filter in the air inlet to prevent negative effects of air pollutants on the stack. In the fuel cell

itself, a certain amount of atmospheric oxygen is consumed, and the oxygen-depleted air leaves the fuel cell at the cathode outlet. The electrochemical reaction in the cell produces pure water, most of which leaves the system in gaseous form with the cathode exhaust air. A water separator can separate condensed water in liquid form, which must be discharged.

G) Cooling loop

In addition to electrical energy and wastewater, the fuel cell also produces waste heat. For stack power outputs of more than 3 kW, this is usually conducted out of the stack via a liquid circuit. Due to the special requirements of the cooling medium (e.g., low electrical conductivity, chemical stability of all components against cooling liquid), two separate cooling circuits are often preferred: one for the PEMFC and one to dissipate heat to the environment. This requires pumps and heat exchangers as well as mixing and control valves that dissipate the heat via a heat sink and expansion tank. Ideally, the waste heat can be used, e.g., for the temperature control of a passenger compartment, but it can also be released unused into the environment via a re-cooler.

H) Power electronics

Usually, the PEMFC system supplies energy to a high voltage DC link (to charge batteries and/or energize an electric motor / drive train). Since the FC voltage level normally does not directly fit the demands of the electric consumers one or more DC/DC converters resp. DC/AC converters are necessary. Furthermore, the PEMFC itself and the corresponding BoP components need a certain amount of energy to be operated. This also must be ensured by an appropriate power electronics converter.

I) Control units and safety instrumentation

A control system is needed to operate the fuel cell. Usually, however, there is also a higher-level control system for the vehicle, which can also take over safety tasks. This includes, for example, hydrogen detectors, pressure and temperature sensors, etc. In the event of potential danger, the PEMFC system can be brought into a safe state immediately. In addition, a data logger and an human-machine interface (HMI) as interface to the user can be optionally built in.

J) Power characteristics

A polarization curve (also called a U/I characteristic) is usually used as a measure of the performance of a fuel cell stack. This is valid for any kind of fuel cells not only PEMFCs. An exemplary course is given in the following .

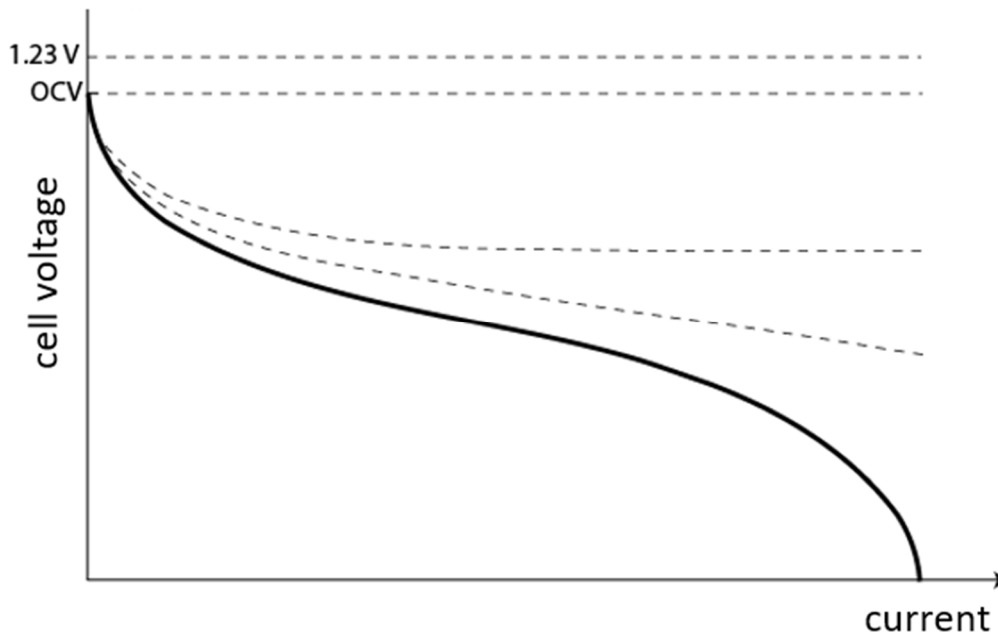


Figure 17. U/I characteristic or polarization curve of a fuel cell

When no current is drawn, the so-called open circuit voltage (OCV) is set. Due to various losses, this is significantly below the theoretic normal potential of the chemical reaction at about 1 volt. As soon as current is taken out of the system by an external consumer, the voltage drops along this curve.

3.3. Overview of the performances

As described previously, each technology possesses its own operating principle and efficiency. Therefore, Table 6 aims to summarize the main characteristics of the major types of FCs.

Table 6. Summary of the FCs' characteristics [23] [31] [32] [33] [34] [35]

FC Type	PEMFC	AFC	PAFC	SOFC	MCFC	DMFC
Operating temperature [°C]	50-100	90-100	150-200	600-1000	600-700	70-100
Efficiency [%]	40-50	50-55	40-50	50-60	50-60	30-40
Energy density [kWh/m ³]	112-770	-- ⁵	--	172-462	25-45	29.9-274
Power density [kW/m ³]	4-35	1	0.8-1.9	4.2-19	1.05-1.67	0.6
Lifespan [h]	>4000	~8000	-- ⁵	>10000	~7000-8000	>4500

PEMFC is the most commercialized technology due to its low operating temperature, short start time, and ease of use of its oxidant (i.e., atmospheric air) [36]. PEMFCs are already used in many systems, such as the first usable hydrogen-electric hybrid car in 2014 or more recently in the NEXP car from Hyundai, which reaches a range of 570km [37]. Hybrid configurations composed of Li-ion batteries and PEMFC are also under significant investigation with developments like the first hydrogen-powered train presented in 2016 by Alstom [38]. These systems are the current state of the art for FCs

⁵ Information was not found in literature.

and are expected to remain the main technology for the next 10 to 15 years. However, SOFCs are also gaining attraction thanks to their high efficiency and the possibility to use alternative fuels. They are already used in specific applications such as power backups for hospitals or data centers [39]. Finally, other types of fuel cells are used mainly for niche applications that require very particular operating conditions.

3.4. Fuel cell technology selection

Concerning the short-term FC technology, the GENESIS deliverable D1.1 identified that the minimum requirement to make fuel cells competitive in aviation is to reach specific powers at the system level above 2kW/kg [1]. Unfortunately, these systems are not expected to become commercially available earlier than 2035, as current state-of-the-art systems can only reach around 0.86 kW/kg [40]. Consequently, the FC technology is not ready yet and will not be incorporated for the short-term analysis. However, SOFCs and PEMFCs will be the technologies chosen to design the medium to long-term design as they show the highest energy and power densities. In addition, both technologies are receiving most of the scientific attention. Thanks to the significant funding allocated to research on FCs, major developments are expected to happen in the next 10 to 15 years to make FC systems viable for medium and long-term solutions.

3.5. Hydrogen storage

Hydrogen storage is a key technology for the advancement of hydrogen and fuel cell technologies in every application. Hydrogen has the highest energy per mass amongst standard fuels; however, its low-density results in a low energy per volume. Hydrogen has a density of 90g/m^3 , making it the lightest gas.

Table 7. Hydrogen properties [41]

Properties		Units
Formula	H ₂	-
Molar mass	2.016	g/mol
Density @ 20°C, 1atm	0.08342	kg/m ³
Boiling point 1atm	-252.8	°C
Density at boiling point	70.96	kg/m ³
Ignition limits in air	4 - 75	vol. %
Detonation limits in air	13 - 65	vol. %
Minimum ignition energy in air (MIE)	0.02	mJ
Heat of combustion	120	MJ/kg

The main goal of hydrogen storage development is to increase the density. To do so, three approaches are possible: increasing the pressure, reducing the temperature, or using a material with a high hydrogen content as a carrier.

The main available storage technologies are high-pressure tanks, cryogenic liquid tanks, and hydrides (see Table 8). The criteria by which the technologies are selected depend on the application.

Table 8. Hydrogen storage overview [42]

Storage technology	H ₂ state	Pressure	Temperature [°C]	H ₂ density [kg/m ³]	Gravimetric index [%]
High pressure tanks	Gaseous	200-700	25	15 - 40	< 7
Cryogenic tanks	Liquid	1-10	-253	70	6
Hydrides	Solid	1-10	25	100	~2

Cryogenic storage is influenced by ambient temperature, as the liquid hydrogen warms up, gaseous hydrogen is produced and needs to be used, reliquefied, or vented. Therefore, it is not used in applications where the tanks might stay unused or unattended for long periods.

Gaseous storage at ambient temperature reaches hydrogen density up to 40 g/L for pressures as high as 700 bar. The density is half as high as cryogenic with high pressure and results in much heavier tanks to ensure a high level of safety, but these tanks require no temperature regulation. It is used for long-time storage and applications where the environment and usage cycles are variable such as road mobility.

Solid storage is a material-based storage in which hydrogen is stored on the surface of solids by adsorption or inside of solids by absorption. Several technologies are researched, like carbon nanotubes or metal-organic frameworks (MOFs), but hydride storage is the most mature technology. Solid storage achieves high density but has a lower gravimetric index than the other solutions as the mass of the solids increases the mass of the storage system.

One indicator of the storage efficiency is the gravimetric index, %wt., i.e., the ratio of the mass of hydrogen stored over the mass of the storage system.

$$\%wt. = \frac{mass(H_2)}{mass(storage)} \cdot 100$$

3.5.1. Gaseous state storage

In order to achieve acceptable density, the gaseous hydrogen is typically stored in pressure vessels between 200 and 700 bar. At those pressures, the hydrogen density is still below 40g/L at ambient temperature, is still way lighter than the container designed to withhold the resulted stress.

The different structures of pressure vessels are classified into four types:

- Type I is an all-metal tank; it is the most commonly used for gas storage and the cheapest but heavy due to its materials and not suitable for storing very light gases such as hydrogen.
- Type II is a metal tank reinforced by continuous fiber composite in the hoop direction. This enables thinner and lighter tanks compared to type I tanks.
- Type III is a metal liner fully overwrapped with composite material. The metal liner is thin and constitutes the hydrogen-tight barrier.
- Type IV, similar to type III, with a polymer liner. The polymer liner makes it the lightest technology so far. It is the latest technology in terms of pressure vessels and the most commonly used for hydrogen storage due to its lightness.

The next step of pressure tank design would be a liner-less composite tank with a 10-20 % decrease on weight expected compared to type IV [43]. The main challenges are to guarantee a low permeation rate through the thermoset matrix of the composite and to wind the composite without the liner acting as a mandrel. The technology is not very mature yet but is under development in several companies.

To ensure safety and cycling resistance, the static burst pressure is designed to be much higher than the service pressure. The legislation imposes a burst pressure/service pressure ratio between 2.25 to 3 for ground applications. This ratio can be lowered to 1.5 on space application when the usage is more controlled and the cycling this reduced.

The composite shell is designed to withstand the mandatory burst pressure of the tank. It is usually formed by filament-winding of continuous fibers soaked in a polymeric matrix using the liner as a mandrel. Although the composite is shaped over the liner, they are not physically bonded, and gaps can form between the liner and the composite at low pressure.

The thickness of the composite used is directly linked to the service pressure, the diameter of the tank, the mechanical properties of the composite, and the legislation safety coefficient depending on end-use.

Three kinds of fibers are used for pressure vessels:

- Glass fibers are often used for intermediate pressures stationary application where cost is more important than weight, since its tensile strength is average, between 3300 and 5000 MPa.
- Aramid fibers are seldom used due to their medium resistance and price.
- Carbon fibers are pricier but have better mechanical properties, tensile strength is typically between 3500 and 7000 MPa. They are also very stiff with Young's modulus from 230 to 600 GPa [44].

The liner assures the gas tightness of the vessel. It is tightly assembled to the boss by a mechanical assembly or directly molded over it depending on the transformation process.

Hydrogen molecules, being very small, can permeate through many water-tight materials, especially polymers. In order to keep this effect to a minimum, the material has to be chosen accordingly; high-density polyethylene (HDPE) is the first choice for the liner material because of its good performance and light weight (0.96 kg/L), and polyamide PA6 is more and more commonly used due to its good gas barrier properties. Another advantage in polymer liners is that polymer contrary to metal is not subject to hydrogen embrittlement, which occurs when a susceptible material, generally a rigid metal, is attacked by hydrogen while under stress, resulting in the cracking of the material. Aluminium and especially steels are susceptible to hydrogen embrittlement depending on temperature [45].

The downsides to polymer liners are that they are more vulnerable to temperature and ageing. Polymer liners also have a low thermal conductivity. During quick-fueling of the tanks, the hydrogen warms up, and the heat produced is trapped into the tank. The tank temperature can rise to the liner maximum usage temperature and thus limit the fueling speed. Metal is a much better conductor, and thus, metal tanks can generally be fueled faster.

Bosses assure the interface of the tank with the system it is part of. The gas tightness is usually achieved with elastomer O-rings, and the accessory is connected via a thread. The bosses are the only metallic part of a type IV pressure tank, and specific attention must be given to hydrogen embrittlement. International standards as ISO11114-1 or ISO7866 compare the compatibility of materials with different gases and deem acceptable some types of steels, stainless steels, and aluminium alloys for pressure vessels.

Accessories, such as temperature sensors, thermally-activated pressure relief devices (TPRD), pressure relief valves, etc., can be added directly to the tank depending on its end use to assure safety.

Applications

Today, high-pressure vessels represent the most mature storage technology to store hydrogen. A type IV pressure vessel is considered the best solution because it offers good performance in terms of safety, flexibility, and weight. Recently developed 700 bar type IV vessels demonstrate promising results in high cycling resistance, burst pressure, hydrogen tightness, and gravimetric capacities, and thus are the primarily used technology for fuel cell electric vehicles (FCEV) and mobility.

It is also used for onboard light-duty vehicles, material-handling equipment, portable power applications, long-term stationary storage, buffer tanks for hydrogen production on dispensing stations, and hydrogen transportation.

However, the challenge for higher storage density remains. The energy density of hydrogen is three times higher than that of gasoline but with volumetric energy density, it is the opposite. 700 bar hydrogen has a density around 5 MJ/L, whereas gasoline has a density of 32 MJ/L [46], which is unfavorable for long-range aviation.

The TLAR for GENESIS announce an average amount of 150 kg of hydrogen for the medium term perspective depending on the mission strategy. With the current performance of gaseous storage, the necessary hydrogen tanks would weigh at least 2.15 tons and fill 3.7 m³ of space just for the compressed gas. The cylindrical shape of these tanks also generates lots of empty space that are difficult to make use of.

3.5.2. Liquid state storage

Storage of hydrogen in its liquid form requires cryogenic temperatures since the boiling point of hydrogen at 1 atm is -252.8°C [46]. In these conditions of temperature and pressure, liquid hydrogen has a density of 70.8 kg/m^3 . The cost attached to the liquefaction of hydrogen is significant energy- and equipment-wise.

The minimum liquefaction work required for hydrogen liquefaction depends on the initial and end state. Turning gaseous hydrogen at 1 atm 25°C to saturated liquid hydrogen at the same pressure requires a minimum work of 3.9 kWh/kg , about ten times that of liquid natural gas (LNG). The two main steps making 80% of the liquefaction work are:

- Cooling of gaseous hydrogen to saturated hydrogen at -253°C (20K).
- Condensing the saturated gas into saturated liquid

In reality, the total energy demand for liquefaction is $\sim 10\text{ kWh/kg}$ with current liquefaction technologies, which represents more than 30% of the hydrogen energy content [47].

Hydrogen has a low boiling point and low latent heat, so it evaporates easily with the heat transfer from outside the tank. The dense gaseous hydrogen increases in pressure, and since the tanks are not designed to bear pressure, the gaseous hydrogen has to be evacuated. This phenomenon is called “boil off” [48] and is characterized for a specific tank by the fluid evaporation rate or boil-off rate (%/d), i.e., the percentage of hydrogen lost per day under normal conditions.

To limit this phenomenon, insulation is the key element of such equipment. Standard insulation construction like polyurethane foam that is used for LNG is usually replaced with high-vacuum insulation ($<10^{-2}\text{ Pa}$) for small and medium tanks under 300 m^3 capacity and low-vacuum insulation ($<1\text{ Pa}$) for large tanks [49]. Since heat transfer depends on the exchange surface, large tanks with smaller surface-to-volume ratios have reduced boil-off rates around 0.1 %/d against $0.5\text{--}1\text{ %/d}$ for small and medium tanks [50].

Tanks are usually cylindrical; however, spherical tanks reduce the surface-to-volume ratio. Cryogenic temperature requires particular attention in the materials, at such temperatures, most materials transit from ductile to brittle behavior. Consequently, though polymers would be a good material choice considering their low thermal conductivity, their low-temperature embrittlement, i.e., lack of toughness, excludes most of them from cryogenic applications. Materials commonly used with liquid hydrogen service are austenitic stainless steels and aluminium alloys.

A way to reduce the boil-off losses and to further increase the hydrogen density is to store it at cryogenic temperatures and high pressure, also known as cryo-compressed storage.

The design is a hybrid between the compressed and liquid hydrogen, with the vessel designed to hold cryogenic fluid and withstand pressure around 300 bar. The density can reach $70\text{--}80\text{ g/L}$, which is the highest density for physical hydrogen storage. The low-temperature and high-pressure design allows the use of smaller cryogenic storage tanks in mobility applications even if extended idling periods are needed. Nevertheless, this technology is still not very mature and not used commercially [51].

Applications

Liquid hydrogen is the main technology in current infrastructures for storage and delivery. However, is not used in mobility with FCEV mainly because of the boil-off. Personal cars do not have a fixed schedule, and cars would rather rapidly lose its content by boil-off if left unused, which is not consumer-wise acceptable. It is also a significant safety hazard, although hydrogen is nontoxic and can be safely released in the atmosphere, it has a high diffusivity in the air and, in a closed space, can rapidly decrease the oxygen rate and cause suffocation. In addition, it is a highly flammable gas and has an explosivity range of $4\text{--}74\text{ %}$ [52] in the air and low ignition energy of only 0.02 mJ . Ignition

sources can be a hot spot, electricity and even static electricity. Thus, venting gaseous hydrogen from boil-off in a closed space is extremely dangerous and unsuited to the automobile industry [41].

If the venting of cold hydrogen is not problematic, and large quantities of hydrogen are required, liquid storage can be used, as it is the case in industry or hydrogen road and sea transportation. For aviation, boil-off would not be significant considering the high frequency of service of commercial aircraft, but the volumetric energy density of liquid hydrogen is a lot lower than that of kerosene [48].

To respond to the medium term TLAR of 150 kg of hydrogen, 2.1 m³ of liquid hydrogen are needed, which could be stored in a 2.5 tons tank on average. Since the flight missions are rather short and boil-off is low, the insulation could be lightened.

3.5.3. Solid storage - hydrides

Hydrogen does not have to be stored in its pure form. It is the smallest element and the 3rd most abundant on earth, widely available in common molecules, and many substances like water and most hydrocarbons have a higher hydrogen density than pure hydrogen (see Table 9). By finding appropriate carriers that can absorb high content of hydrogen, we can achieve high storage efficiency.

An optimal hydrogen-storage material needs to have the following properties: high hydrogen volumetric and gravimetric capacity, fitting conditions for absorption and desorption, reversibility.

Table 9. H₂ content in different liquids under STP [53]

Liquid	Formula	Volumetric H ₂ content [kg H ₂ /m ³]
Liquid hydrogen	H ₂	71
Water	H ₂ O	111
Methanol	CH ₃ OH	100
Heptane	C ₇ H ₁₆	113

Material-based storage is the subject of a lot of research and is progressing rapidly. Nevertheless, most of the solutions are still at research level or marginally used like metal organics frameworks (MOFs) or carbon nanotubes, and some are non-reversible like borohydrides. At the moment, metal and ionic hydrides are the most used industrially and commercially for hydrogen storage. Unfortunately, such materials are often heavy and result in poor gravimetric capacities or involve highly exo/endo-thermal reactions to absorb and release hydrogen (see Table 10).

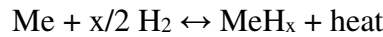
Table 10. Different technologies of material-based storage [42]

	Adsorbents	Complex hydrides	Single-phase hydrides	Borohydrides
Example material	Carbone nanotubes, MOFS	LaNi ₅ , FeTi, TiV, NaAlH ₄	MgH ₂	LiB ₄
H ₂ content wt. %	<8	1 to 5	7	18.5
Temperature of desorption	-200°C	-40 to + 150°C	300°C	>400°C

Hydride storage is the most commercially successful material-based storage type and thus, its behavior is better understood. Hydride storage stores hydrogen in an atomic form rather than in a molecular state like physical storage.

Single-phase light weight hydrides

Many metals and alloys react with hydrogen to form hydrides following this reaction:



Hydrides are formed through a solid/gas reaction between hydrogen and a metal, likely to form a reversible bond with hydrogen atoms. The absorption reaction is exothermic, and for hydrogen release/desorption, heat input is needed.

This amount of energy depends on the hydrides characterized by their dissociation pressure and temperature, conditions at which the hydride absorbs the most hydrogen.

Magnesium hydride (MgH_2) is one of the most researched lightweight hydrides. It is light, has a relatively high hydrogen content, and is very stable under normal conditions. The release temperature is around 300°C , which is relatively high for mobility but is adapted for some stationary applications.

The main shortcoming of MgH_2 for hydrogen storage is its slow kinetic reaction. Like for all hydrides, this parameter can be changed by interfering with process parameters, crystallography of the material, size of particles, and the use of additives or catalysts.

Complex hydrides

Most single-phased hydrides need to be brought up to high temperatures ($>300^\circ\text{C}$) to release hydrogen at 1 atm [54]. For example, zirconium hydride (ZrH_2) has a volumetric hydrogen density of 116 g/L, which is much higher than the volumetric hydrogen density of liquid hydrogen but has a release temperature above 700°C . The hydride form is highly stable at room temperature. Alternatively, nickel hydride (NiH) has a very low stability. Nickel cannot absorb large amounts of hydrogen at atmospheric pressure and only forms small quantities of hydride at high pressures. The intermetallic compound ZrNi reacts with hydrogen to form nickel zirconium hydride (ZrNiH_3), which releases hydrogen at 300°C at 1 atm., high enough that it is stable under normal conditions and low enough that it does not need a huge amount of energy to reconstitute hydrogen.

Similarly, lots of alloys can be designed to achieve different release conditions fitted to the application, by combining hydride forming elements and non-hydride forming elements (see Figure 18).

A: hydride forming element; **B**: non hydride forming element

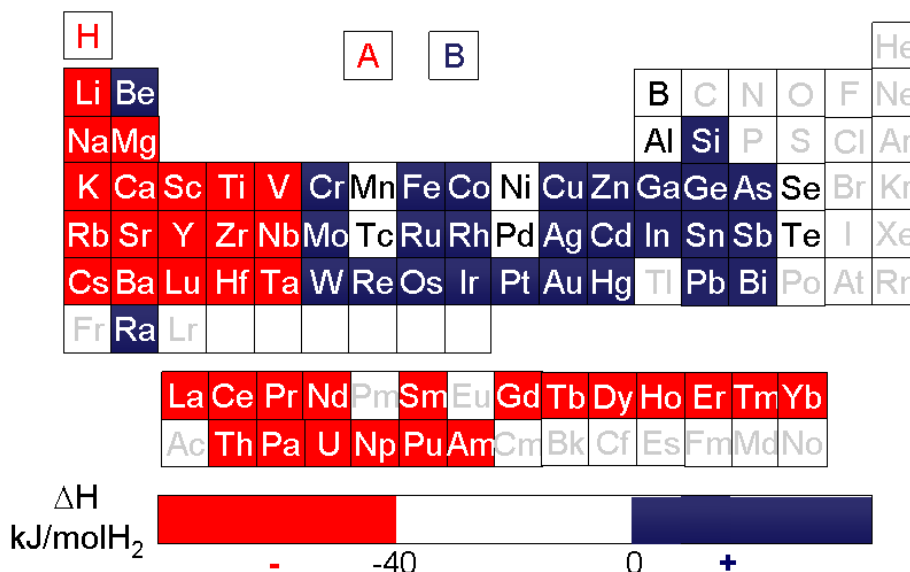


Figure 18. Hydride and non-hydride forming elements in the periodic system of elements [54]

Applications

Metal hydrides storage is a safe and compact alternative to physical hydrogen storage. System design has to select a hydride with suitable thermodynamic properties according to the application. The heat reaction and temperature of operation of the hydride should correspond to the waste heat and temperature of service of the connected device, typically the fuel cell or combustion system.

Although the hydrides themselves have theoretical high storage capacities, considering the temperature management and pressure bearing depending on the hydride thermodynamics, the overall hydrogen storage density is usually not above 1.8 wt % H₂. But research and innovation show several promising systems with high gravimetric storage in the range of 8-12 wt. % H₂.

With current mature technologies, a hydride tank corresponding to the medium term TLAR, would weigh more than 8 tons, which is not suitable for aviation. Still being the heaviest hydrogen storage technology, hydride storage is used for applications where the mass is not of concern, like stationary installation or when small amounts of hydrogen are needed, but special storage conditions (high pressure, cryogenic cold) cannot be achieved or maintained.

4. Turbine / ICE generator set analysis

4.1. Introduction

Several types of engines are used nowadays on civil and military aircraft to produce the necessary power and thrust. For a commuter or a small regional aircraft, turboprop engines are generally preferred over reciprocating engines or turbofans. This results from trade-off analyses including considerations on reliability, costs, ground performance, and fuel consumption. A turboprop engine comprises three main components: a gas turbine core (pretty similar to the one for a turbojet/turbofan engine), a gearbox, and a propeller. The gearbox helps to transfer the power from the core engine to the propeller, reducing the rotational speed. The gas turbine includes one or more compressors (axial or radial ones), a combustion chamber, and one or more turbines. There are several available options concerning the core engine configuration. These mainly differ in how the power is transferred to the gearbox and the propeller. In some designs, the turbine powering the gearbox is directly linked to one of the compressors. A different solution is to link the gearbox to a turbine that is not on the same shaft of any of the compressors extracting work from the gas, leading to what is usually called a free turbine turboprop engine. Just as the turbojet engine, the turboprop adopts a gas turbine core to generate power. What really separates one solution from the other is how this power is used. In turboprop engines, most of the available power is extracted by the turbine linked to the propeller, thus noticeably reducing the kinetic energy of the air expelled through the exhaust and the amount of jet thrust produced by the engine.

This chapter provides an overview of the approach adopted to model a gas turbine engine for the short-term scenario (2025-2035) in terms of performance (basically power-specific fuel consumption, SFC), emissions, weight, main dimensions, and costs. It is important to highlight that this approach is independent of the selected timeframe and can be easily adapted to different time horizons by simply modifying those assumptions that depend on technological factors or an envisaged entry into service (EIS).

The main objective was to build a rubber engine model that could be easily integrated into an aircraft design chain and used to perform trade factor analyses on fuel burn concerning engine dry mass, engine maximum diameter, and production cost, enabling aircraft designers to carry out single and multi-objective optimizations. By including specific aircraft requirements among the set of available input variables, such as the shaft power delivered (SPD), the power off-takes, and the overboard bleed, the engine model has been made sensitive to variations to the aircraft model, since they are reflected in the fuel consumption, the engine dry mass, and the main gas turbine dimensions. At the same time, this rubber engine model can provide valuable information to the engine manufacturer in terms of main gas turbine design parameters, such as the design burner exit temperature T_4 , the overall pressure ratio (OPR), and entry mass flow W_2 , since those have also been included in the sets of input/output variables.

The effect of advanced technologies has been included in the rubber engine model. The EIS has a direct impact on the performance of the main components of the engine (i.e., compressors, turbines, and burner). An additional technology factor has also been introduced in the model to account for less/more conservative designs. This factor impacts, again, on the performance of the compressors, on the materials for the turbines, on the cooling technology, on the pressure losses in the main ducts of the engine, and on the mechanical efficiencies. The value selected for this additional technology factor also directly impacts the final production cost of the engine. The dataset produced for the rubber engine model of the short-term scenario also includes variations to this input variable, allowing to perform for the same timeframe/scenario different analyses based on various assumptions on the technology level.

The impact of alternative fuels on the engine design has been included in the final rubber engine model. Biofuels in the form of synthetic paraffinic kerosene (SPK) have been modelled to consider their impact on fuel consumption and emissions. A basic strategy based on the fuel's lower heating value (LHV) of different blends of SPK with conventional jet fuel (namely Jet A-1) has been adopted, with calibration factors on emission indexes (EI) accounting for differences in terms of emissions concerning traditional kerosene.

Chapter 4.2 provides general information on the assumptions and methodology adopted to generate the final rubber engine model. Details have also been provided on the tools used to generate the reference dataset. Chapter 4.3 provides proof of validation of the selected methodology for a representative engine (i.e., the Pratt & Whitney PW127E engine model, equipped on the ATR 42 aircraft [55]), and also an overview of the results produced by the short-term engine model, accounting for the usage of different fuels and different design approaches (i.e., less/more conservative designs). Finally, Chapter 4.4 focuses on the approach and the tools used to generate a surrogate rubber engine in the hybrid-electric aircraft design work chain.

4.2. Methodology

Since the ATR 42 is the reference aircraft model selected for the performance comparisons concerning hybrid-electric aircraft platforms, its Pratt & Whitney PW127 engine has been selected as the reference engine model for the analyses. The PW127 is part of the PW100 family, a series of 1300 to 3700 kW turboprop engines manufactured by Pratt & Whitney Canada [56]. The first engine of the 127 series was certified in 1992, with the PW127E, the actual reference model used for validation and the analyses, certified in 1994. Except for the PW150 engine model, all the engines of this family feature a three-shaft configuration, with a low-pressure (LP) radial compressor, driven by a single-stage low-pressure turbine, supercharging a high-pressure (HP) radial compressor, driven by a single-stage high-pressure turbine. A third, two-stage, free turbine finally powers the propeller through a reduction gearbox. A scheme of this engine configuration is reported in Figure 19.

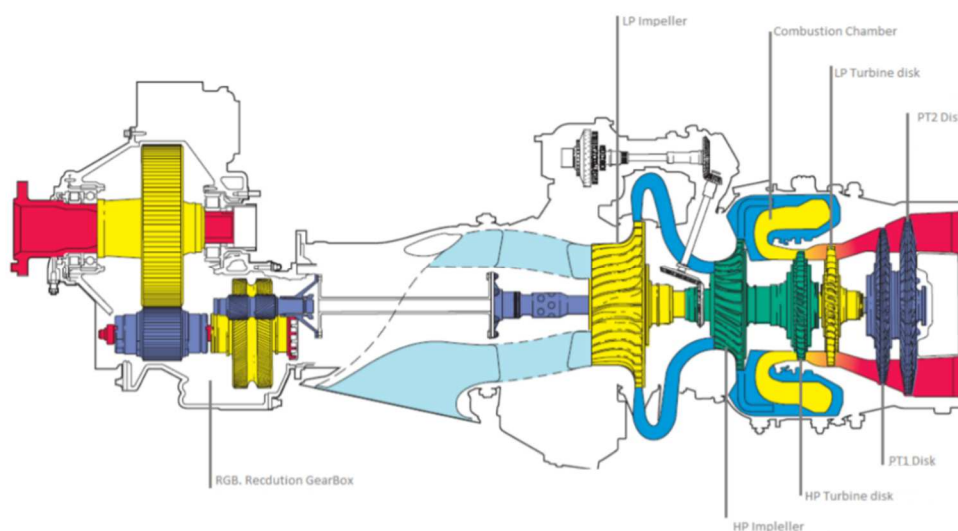


Figure 19. PW127 engine configuration [57]

The characteristics of the PW127E model are summarized in Table 11. Ratings are provided at sea-level (SL), with information on the temperatures provided in terms of variation with respect to the international standard atmosphere (ISA) model. Most of these values have been used to validate the rubber engine model, reported in Chapter 4.3.1.

Table 11. PW127E engine data

Description	Value	Source
Ratings		
Take-off, SL ISA +30	2160 SHP – 1611 kW	[58] [59] [60]
Take-off (one engine), SL ISA +30	2400 SHP – 1790 kW	[58] [59] [60]
Max continuous, SL ISA +30	2400 SHP – 1790 kW	[58] [59] [60]
Max climb, SL	2160 SHP – 1611 kW	[58] [59] [60]
Max cruise, SL ISA +10	2132 SHP – 1590 kW	[58] [59] [60]
Fuel consumption		
Max take-off, ISA SL	0.474 lb/(hp*h) – 0.288 kg/(kW*h)	[58]
Mass		
Dry mass	1060 lb – 481 kg	[58] [60]
Dimensions		
Length	81 in – 2.134 m	[58] [60]
Width	26 in – 0.660 m	[58] [60]
Height	33 in – 0.838 m	[58] [60]
Cycle values		
Entry mass flow rate	18.72 lb/s – 8.49 kg/s	[61]
Overall pressure ratio	14.7	[58]

The actual rubber engine model has been developed using GasTurb 11 [62], a gas turbine cycle program that simulates the most important gas turbine configurations used for propulsion or power generation. GasTurb allows performing gas turbine cycle simulations both for design and off-design conditions. For the off-design simulations, GasTurb requires compressors and turbines maps to simulate the performance of the engine adequately. The program also provides default maps, but they need to be appropriately scaled to produce reasonable results. The program can automatically perform this operation.

In order to produce a parametric model of a gas turbine engine, similar in terms of configuration to the PW127, a set of engine design laws and automatic update strategies have been implemented in the GasTurb design calculation mode, starting from the GasTurb template model for a three-spool turboprop engine. For each generic template model, GasTurb provides a set of default values, which need to be appropriately adjusted for the model to reflect the actual characteristic of the engine at the design point. These input quantities include:

- Burner exit temperature;
- Overall pressure ratio;
- Entry mass flow rate;
- Polytropic efficiencies of the compressors and turbines;
- Pressure ratios of the low and high-pressure impellers;
- Relative amount of cooling air for the nozzle guide vane and rotor blades of the high-pressure turbine;
- Pressure losses for the inter-compressor and inter-turbine ducts;
- Burner efficiency and pressure loss;
- Inlet duct pressure loss and nozzle pressure ratio.

Since the first three quantities in the above list have been selected, along with technological factors, as the main input variables for the GasTurb parametric model, strategies needed to be picked and implemented to update the remaining input variables automatically. GasTurb supports the implementation of these strategies through the definition of additional input variables, the possibility

to define custom composed values, and by enabling the setting of specific iterations, aiming the matching between model input variables and calculated composed values.

The following sub-chapters provide more information on the assumptions performed for each of the input variables listed above. It is important to highlight that take-off (T/O) has been assumed as the design point condition, for which flight conditions have been summarized in Table 12. The selected flight Mach number corresponds to the ATR 42 take-off speed indicated in [59], while the same flat rating (ISA +30) of the PW127E engine model was supposed for all the designed engines.

It is also important to remark that the parametric model that has been implemented in GasTurb is valid for a three-spool turboprop engine configuration similar to the one of the reference engine model: centrifugal compressors on separate shafts, single-stage high-pressure and low-pressure turbines, and a two-stage free turbine. In addition, only the high-pressure turbine has been supposed to be cooled, so no relative cooling air for the low-pressure turbine is ever provided. Unfeasible engine designs generated from having assumed a fixed engine configuration are typically discarded, either because they are not competitive (e.g., too high specific fuel consumption) or because they do not observe mechanical limitations listed in Chapter 4.2.8.

Table 12. Set of conditions for the design point

	Rating	Altitude	Mach number	ISA
Design point condition	Max. take-off	0 m	0.17	+30

4.2.1. Pressure ratios

Since the engine OPR has been set as one of the main input parameters of the rubber engine model in GasTurb (through the definition of a dedicated custom input parameter), the pressure ratios of the LP and HP impellers needed to be consequently set. Suggestions on a plausible pressure split between the two impellers have been taken from [63], in which statistical data are provided for the pressure ratio, mean stage loading, inducer and exducer diameter, and rotational speed of single and double stage radial compressors. Due to the lack of additional and more refined statistical data, variations of this pressure split for the engine OPR have not been assumed, but it has been deemed constant in the GasTurb rubber engine model. Moreover, this pressure split has allowed to match the target rotational speeds of the LP and HP spools to validate the GasTurb model for PW127E real engine data.

4.2.2. Polytropic efficiencies and basic flow path modelling

Two distinct approaches have been adopted to calculate polytropic efficiencies of the radial compressors and axial turbines of the engine.

For the centrifugal compressors, an approach based on the set of formulas and assumptions suggested in [64] has been implemented. Polytropic efficiency values have been assumed starting from the chart of [64], hereby reported in Figure 20a. Where, the polytropic efficiency of the radial compressor is a function of the technology level and the non-dimensional specific speed (NS), defined as:

$$NS = N * VW^{0.5} / \Delta T_{ideal}^{0.75},$$

where N is the rotational speed, VW is the volumetric inlet flow, and ΔT is temperature rise. For a fixed technology level (f_{tech}), the polytropic efficiency is at its peak for a specific value of the specific speed, as can be seen from the chart in Figure 20a. This value is assumed by the rubber engine model as the polytropic efficiency of the radial compressor, once corrected for the EIS, according to the data provided in [63], and hereby reported in Figure 20b. For this correction, the suggested tendency line for two-stage radial compressors has been considered.

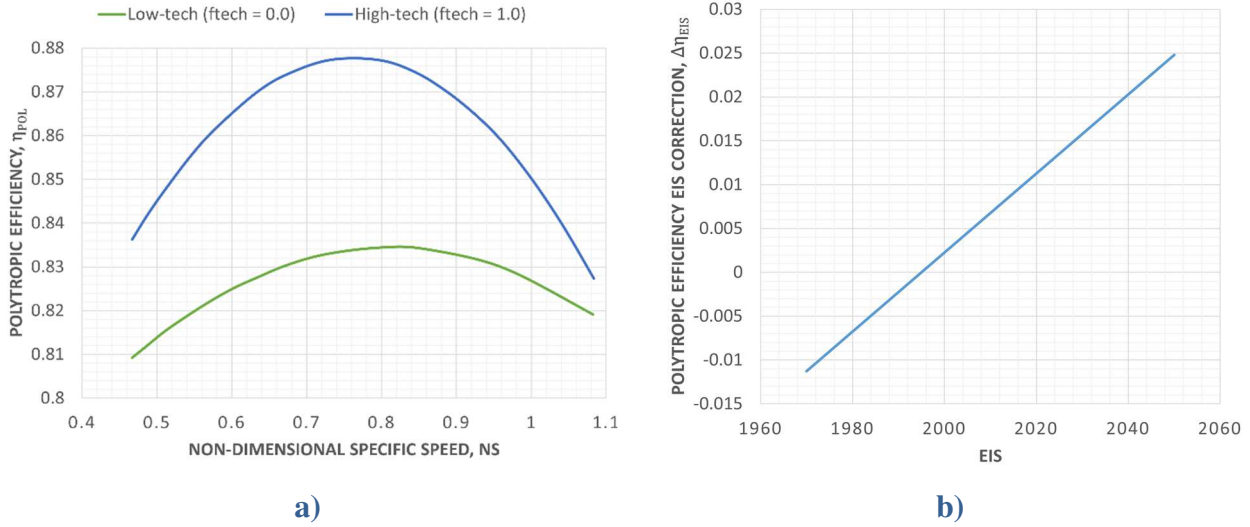


Figure 20. Radial compressor polytropic efficiency versus nondimensional specific speed and technology level according to [64] (left), and EIS correction according to [63] (right)

Starting from the values for the pressure ratios, the nondimensional specific speed, and the polytropic efficiencies, rotational speeds and exit speeds can be consequently calculated by inverting the formula for the specific speed and the formula for the pressure ratio of the impeller (P_3/P_2), also provided in [64]:

$$P_3/P_2 = (1 + (\eta_2 F_{P\ input} F_{slip} U_{ex}^2) / (c_p T_2))^{\gamma / (\gamma - 1)},$$

where η_2 is the isentropic efficiency, $F_{P\ input}$ is the power input factor (typically between 1.02 and 1.05), F_{slip} is the slip factor (typically between 0.9 and 0.935), U_{ex} is the exducer tip speed, T_2 is the total temperature at the inlet section, c_p is the specific heat capacity of the gas at constant pressure, and γ is the heat capacity ratio. At this point, the exducer diameter of the compressor can be easily estimated, having both the rotational speed and the exducer tip speed. This diameter is quite important, especially for the LP radial compressor, because for particularly high values of the OPR, it may drive the general dimensions of the gas turbine, and consequently, those of the nacelle. For the axial turbines, the approach suggested in [63] has been adopted. The polytropic efficiency of a generic axial turbine is a function of different contributions, which can be listed as follows:

$$\begin{aligned} \text{for the HP turbine, } \eta_{pol} &= \eta_{pol}^{***} + \Delta\eta_{EIS} + \Delta\eta_{RNI} + \Delta\eta_{size} + \Delta\eta_{cool}, \\ \text{for the LP and power turbine, } \eta_{pol} &= \eta_{pol}^{***} + \Delta\eta_{EIS} + \Delta\eta_{RNI} + \Delta\eta_{size}, \end{aligned}$$

where

- η_{pol}^{***} is the normalized polytropic efficiency, which is reported in [63] as a function of the mean stage loading $\bar{\Psi}$:

$$\bar{\Psi} = 2\Delta H / (n_{stg} \bar{U}^2),$$

where ΔH is the specific work of the component, n_{stg} is the number of stages, and \bar{U} is the circumferential speed at the mean diameter of the component;

- $\Delta\eta_{EIS}$ is the EIS correction, which is also provided in [63] through several charts;
- $\Delta\eta_{RNI}$ is the Reynolds correction, provided by [63] through a formula;
- $\Delta\eta_{size}$ is the size correction, also provided by [63] in terms of a simple formula;
- $\Delta\eta_{cool}$ is the correction for cooling air, which is applied only to the HP turbine (since it is the only assumed cooled turbine). Its calculation relies on the related chart obtained from statistical data and provided in [63].

The calculation of normalized polytropic efficiencies has been implemented in the GasTurb rubber engine model using lookup tables by digitalizing charts provided in [63]. These digitalized charts are also reported in Figure 21, for the HP turbine, and in Figure 22, for the LP and free turbines. It is worth noticing that [63] does not provide for these two quantities a single trendline, but a supposed range of variation since these charts have been derived from collections of data for several gas turbine engines. It is also reasonable to suppose that higher values may be linked to less conservative design choices and higher technology levels, independently of the supposed EIS. For this reason, the previously mentioned technology factor, f_{tech} , has been introduced into this model, allowing to select, for a given mean stage loading, the corresponding normalized polytropic efficiency. This factor is the same acting on the polytropic efficiency of the chart of Figure 20a. Polytropic efficiency EIS corrections have also been implemented in the GasTurb rubber engine model in the form of lookup tables by digitalizing related charts provided in [63]. The digitalized curves are reported in Figure 23 for the HP turbine and Figure 24 for the LP and free turbines. Finally, the same approach has been applied for the cooling air correction for the polytropic efficiency of the HP turbine. The digitalized chart providing the related lookup table to be implemented is reported in Figure 25. The relative cooling air is the total amount – nozzle guide vanes (NGV) plus rotor blades – of cooling air provided to the HP turbine, divided by the total amount of cooling air passing through the HP impeller. This amount depends on the burner exit temperature, the supposed cooling technology, and the materials adopted for the components of the HP turbine. Chapter 4.2.3 provides more information on how this quantity is calculated.

In order to have an estimation of the mean stage loading for each turbine, which is necessary for the calculation of normalized polytropic efficiencies, basic modelling of the flow path is required. For this purpose, the steps and calculations reported in Figure 26 have been adopted and implemented in the GasTurb rubber engine model. Assumptions have been performed for the hub-to-tip ratios and the Mach numbers at the entry and exit of each turbine. For the first one, values have been set starting from a cutaway of the PW127 engine model (such as the one reported in Figure 19). For the second one, reasonable assumptions have been performed starting from indications provided in [64].

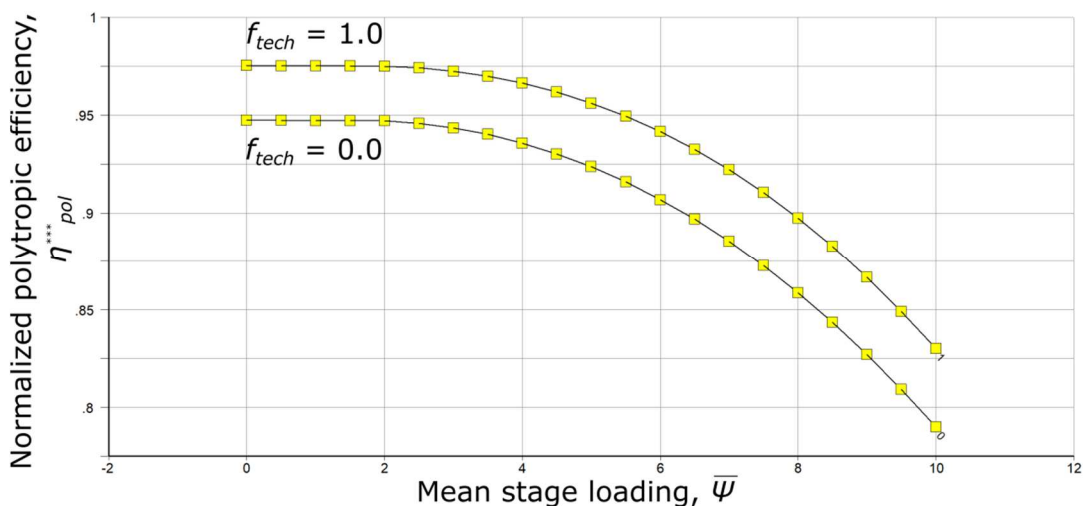


Figure 21. HP turbine normalized polytropic efficiency versus mean stage loading and technology level, derived from [63]

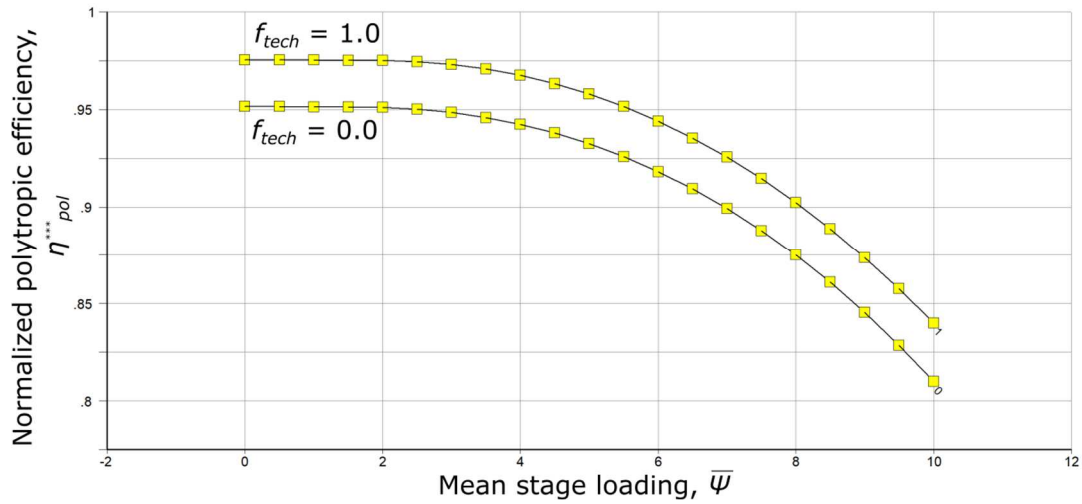


Figure 22. LP and power turbine normalized polytropic efficiency versus mean stage loading and technology level, derived from [63]

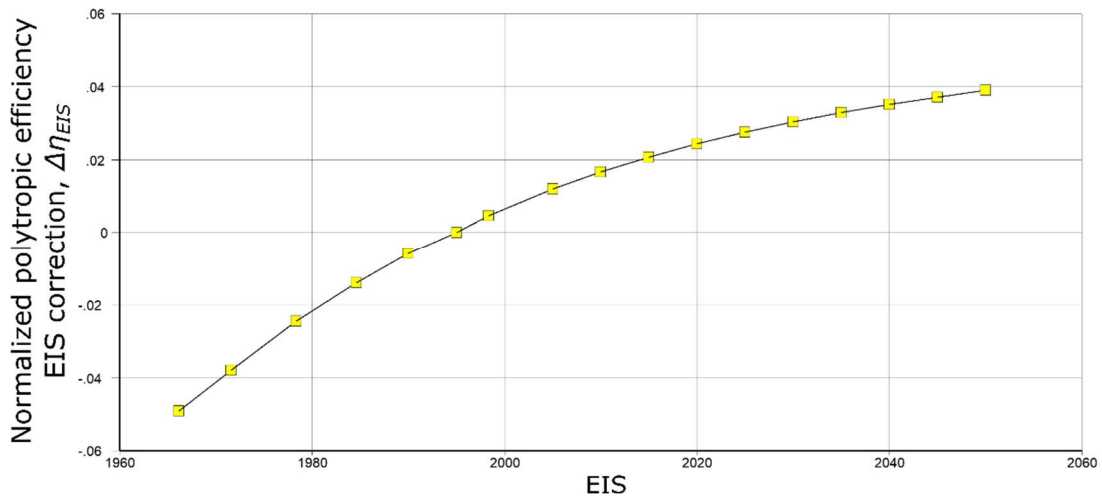


Figure 23. HP turbine EIS correction for polytropic efficiency, derived from [63]

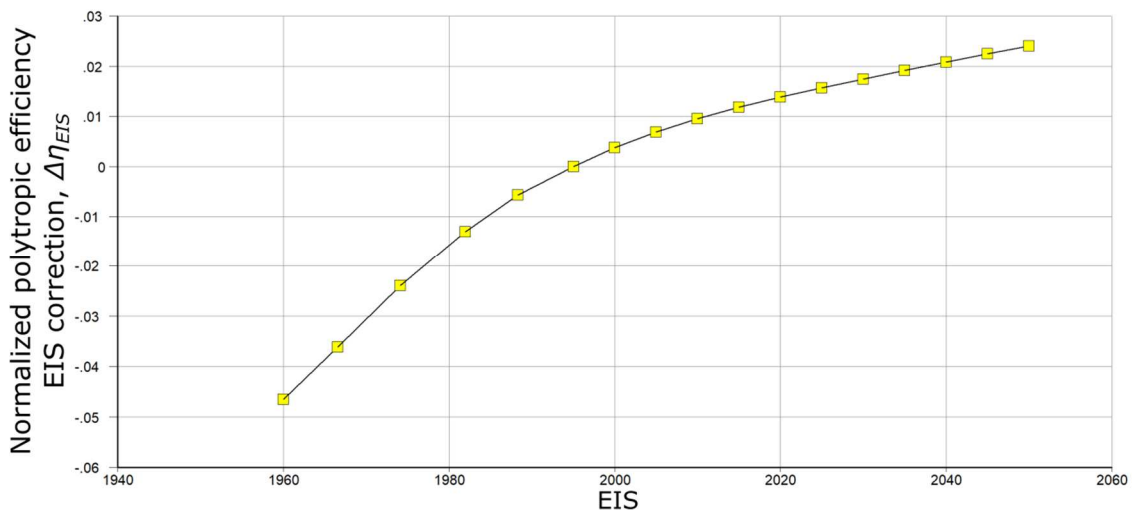


Figure 24. LP and free turbine EIS correction for polytropic efficiency, derived from [63]

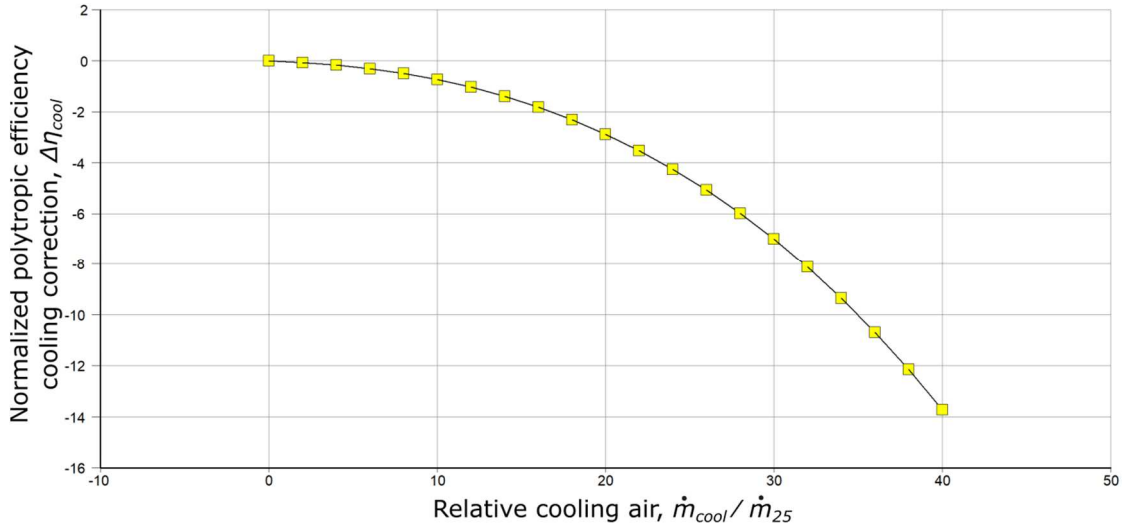


Figure 25. HP turbine relative cooling air correction, as derived from [63]

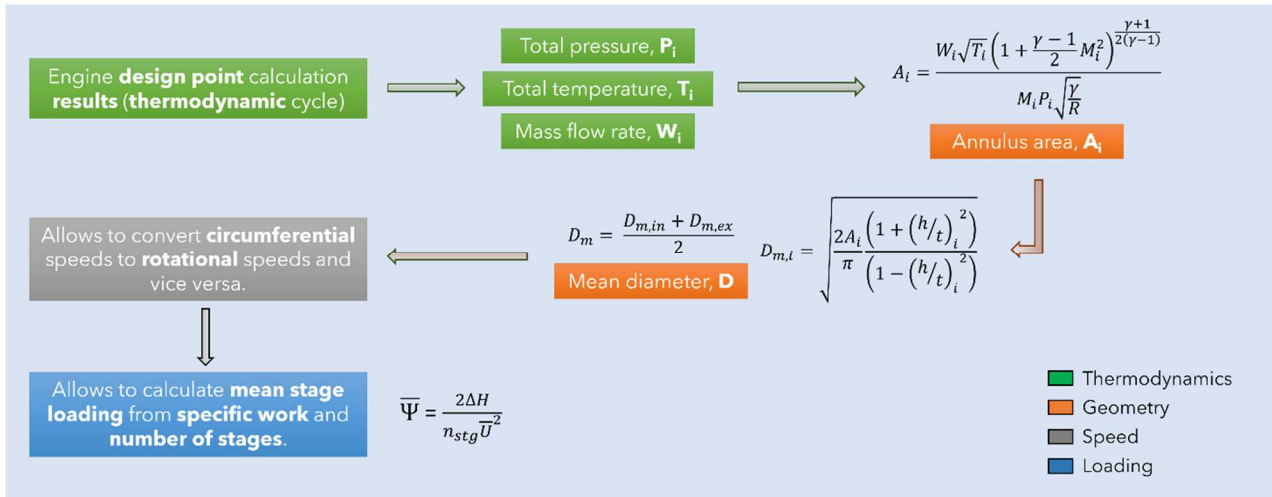


Figure 26. Series of steps for the modelling of the flow path following the combustion chamber

4.2.3. Cooling air requirement

The amount of required cooling air should always be estimated for the most demanding condition in terms of engine temperatures, which is usually take-off. Since the selected design point matches this condition, the amount of cooling air required by the engine can be directly estimated at the design point, avoiding any iteration involving off-design simulations.

For the determination of the relative cooling air mass flow required by each grid of a cooled turbine, the strategy presented in [65] has been implemented. This methodology is essentially based on the cooling effectiveness (η_{cool}) definition for heat exchangers:

$$\eta_{cool} = (T_{HG} - T_M) / (T_{HG} - T_{CA}),$$

where:

- T_{HG} is the hot gas temperature (i.e., the temperature of the air-fuel mixture at the entry of the turbine grid), appropriately incremented to include additional effects, as described in [65];
- T_M is the allowable bulk metal temperature, and depends upon the year of material technology, on the desired life and duty cycle;
- T_{CA} is the cooling air temperature, which reflects the stage of the compressor from which the bleed flow is extracted.

[65] suggests a formula for estimating the allowable bulk metal temperature, both for the stator and for the rotor blades, depending upon the selected EIS. However, it has been assessed that the application of this formula would have led to too many optimistic values, especially for future engine applications. For this reason, a new trendline has been adopted, starting from suggestions provided by [66] and [67]. Allowable maximum temperature values have been collected for several materials and have been linked to the technology factor, as reported in Table 13. This table also provides information on the assumptions performed for the maximum allowable temperature for cooled turbine stages. This information has also been gathered from [66] and [67] and will be used to limit the available design workspace, as highlighted in Chapter 4.2.8. For the calculation of the actual allowable material temperature, a desired 20,000 hours life for the turbine airfoils has been accounted, thus reducing T_M of 30 K, according to the formula suggested by [65].

Table 13. Maximum limiting temperature assumptions for the calculation of the required amount of cooling air (assumed from [66] and [67])

	Maximum T_M	Maximum T (cooled)	Technology factor
Inconel 713C	1200 K	1450 K	0.0
Inconel 792	1250 K	1550 K	0.2
PWA 1480	1300 K	1750 K	0.4
PWA 1492	1350 K	1950 K	0.6
CMC	1400 K	2050 K	0.8
CMC (adv. thermal coating)	1450 K	2100 K	1.0

By using the above definition for cooling effectiveness, the required cooling air mass flow relative to HP compressor entry mass flow for a specific turbine grid (i.e., stator or rotor blades) can be derived from the following correlation, still provided by [65]:

$$\dot{m}_{cool}/\dot{m}_{25} = c_{cool}(\eta_{cool}/(1 - \eta_{cool}))^{1.25},$$

where c_{cool} is the cooling factor, which mostly depends on the cooling configuration and its related technology level. [65] provides typical values for this factor, used to determine a trendline concerning the technology coefficient. Values used as the main reference for the definition of this trendline are reported in Table 14. As with the maximum allowable turbine material temperature, this trendline has been included in the set of formulas for the GasTurb rubber engine model. It is worth mentioning that, as suggested in [65], the cooling factor has also been calibrated to take into account additional effects, which tend to lower the effectiveness of the cooling system, such as end wall effect, leakage, and cooling of shrouds and disks.

Table 14. Cooling factor reference values (according to [65]) adopted to define a technological trend inside the GasTurb rubber engine model

Cooling technology	Cooling factor	Technology factor
Advanced convection (100% tr. edge ejection)	1.4	0.0
Film with convection (75% tr. edge ejection)	1.3	0.17
Film with convection (50% tr. edge ejection)	1.2	0.33
Film with convection (25% tr. edge ejection)	1.1	0.5
Full cover film	1.0	0.66
Transpiration with convection	0.9	0.83
Transpiration	0.8	1.0

4.2.4. Miscellaneous input variables

In order to complete the definition of the rubber engine model, several other input variables had to be set and eventually linked to other input parameters.

Pressure losses for compressor and turbine inter-ducts have been assumed starting from [64] and have been linked to the input factor accounting for the level of technology. [64] provides typical ranges of variation for these losses. A linear trend for the input technology factor has been supposed between the lower and upper bound suggested by [64].

The same approach has also been adopted to define the mechanical efficiencies of the HP, LP, and free turbine spools, for the burner pressure losses (with reference boundaries taken from [63]) and for the turbine exit duct pressure losses. Boundary values are reported in Table 15, along with the reference from literature from which they have been taken.

Table 15. Lower and upper boundaries adopted for the modelling of pressure losses and spool mechanical efficiencies

	Lower bound	Upper bound	Reference
Compressor duct pressure loss	0.98	0.99	[64]
Turbine duct pressure loss	0.975	0.995	[64]
Turbine exit duct pressure loss	0.985	0.995	[64]
Burner pressure loss	0.945	0.97	[63]
Spool mechanical efficiency	0.99	0.999	[64]

For the burner efficiency, a lookup table has been elaborated and implemented in the GasTurb rubber engine model by mainly using suggestions from [68] and by extrapolating for future tendencies, assuming a flat behavior. A graphical representation of this lookup table is reported in Figure 27, while the related dataset is reported in Table 16.

Table 16. Lookup table for the burner efficiency

EIS	Burner efficiency	Reference
1955	0.88	[68]
1975	0.94	[68]
1995	0.99	[68]
2015	0.995	[68]
2035	0.996	extrapolated
2055	0.997	extrapolated

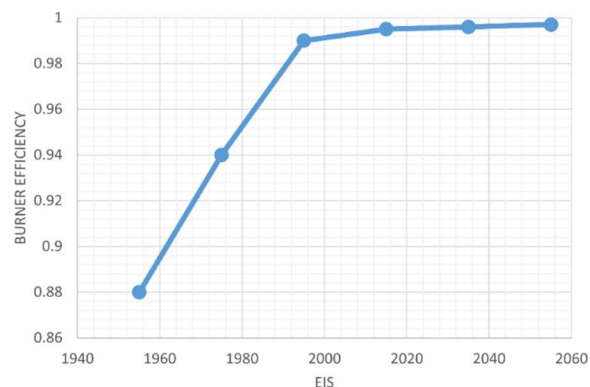


Figure 27. Burner efficiency versus EIS, mainly according to [68]

For the intake and nozzle pressure ratios, constant values (i.e., independent of the selected technology level) have been assumed, reflecting the design point condition. The nozzle pressure ratio has also been fixed by matching the required amount of equivalent shaft power (i.e., the sum of the shaft power and the power derived from the jet thrust) for the reference engine.

4.2.5. Dry mass calculation

There are plenty of semiempirical methods in the literature to estimate the dry engine mass of a turboprop engine. Most of these methods are based on single-input equations, depending on the shaft power of the engine. [69] and [70] provide valid examples of this type of regression law.

In the present context, to link the engine dry mass to one of the driving design parameters of the engine and to highlight the effect of different design choices on the dry mass for a pre-selected target shaft power, the entry mass flow has been adopted as the input for a new semiempirical formulation. For this purpose, engines have been selected from an available online database [71], trying to discard from the set derated variants of the same engine. The list of engines used to generate the regression model is reported in Table 17, while Figure 28 provides a visual representation of this model, along with its regression equation.

Table 17. Dataset used for the generation of the regression model for the engine dry mass

Manufacturer	Model	Year	T/O mass flow rate [kg/s]	Weight [kg]
Pratt & Whitney	PW120	1979	6.7	417
Pratt & Whitney	PW127	1990	8.49	481
Pratt & Whitney	PW150	1995	14.44	690
Walter Aircraft Engines	M602B	1986	7.33	490
Klimov	TV7-117S	1993	7.95	530
Rolls-Royce	AE-2100J	1990	16.33	702
Europrop	TP400-D6	2005	26.3	1938
GE BGA Turboprops	H85	2009	3.8	180
Allison Engine Company	C20R	1960	1.73	78
Allison Engine Company	C40B	1960	2.77	127
Garrett AiResearch	TPE331-10U	1960	3.49	175

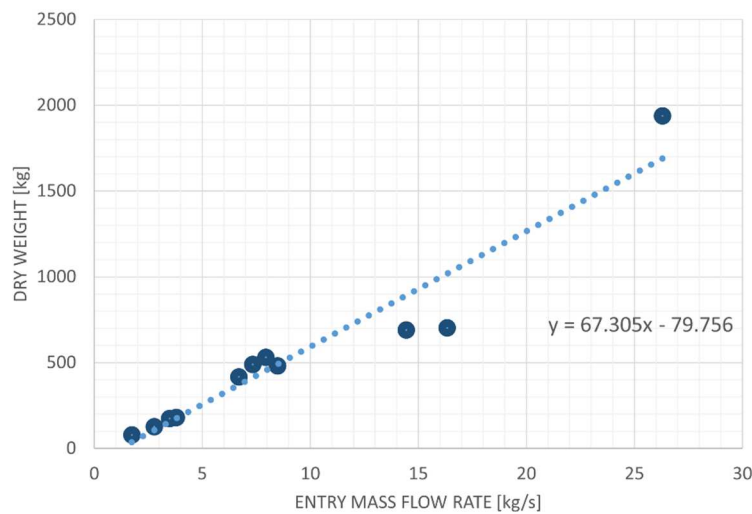


Figure 28. Engine dry mass linear regression law with respect to entry mass flow rate

4.2.6. Main dimensions estimation

Unlike the dry engine mass, there are not so many semiempirical methods available from literature allowing to perform a first-order estimation of the main dimensions of the engine.

To estimate the overall length of the engine, an approach similar to the one of Chapter 4.2.5 has been adopted. The overall length has been linked to the shaft power of the engine through a linear, single-input regression law, which is shown in Figure 29. The dataset of [71] has been used for its generation, still discarding derated engine models from the original dataset.

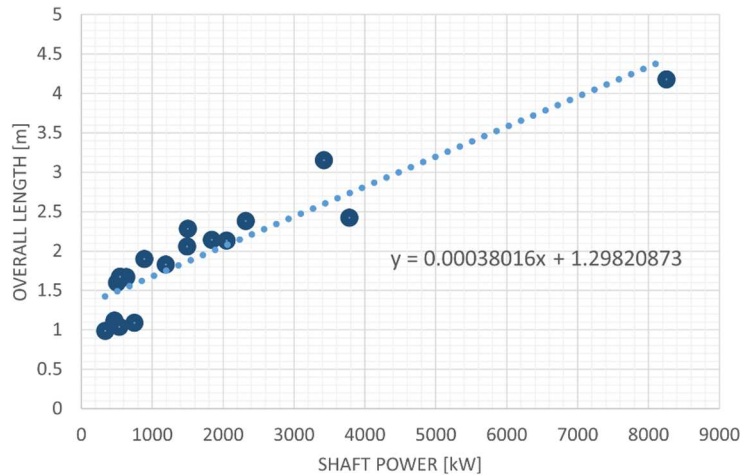


Figure 29. Engine overall length linear regression with respect to shaft power

In order to assess the maximum width and height of the gas turbine, an “almost” component-based (rather than simply semiempirical) approach has been adopted. What typically drives the size of a gas turbine for a turboprop configuration such as the reference one is the outer diameter of the exducer of the LP impeller and the tip diameter of the last stage of the free turbine. These two quantities are estimated by the rubber engine model implemented in GasTurb since basic modelling of the gas path is performed to assess mean stage loadings and polytropic efficiencies of the turbines group. By setting constant multipliers for these diameters, based on ratios estimated for the reference engine, it is possible to link the overall dimensions of the engine to its actual design point thermodynamic cycle. These ratios are reported in Table 18. In the present modelling, the width of the engine would be driven by the bigger of the two previously cited diameters. In contrast, the diameter of the LP impeller would always drive the height of the engine, at least for the selected configuration.

Table 18. Ratios for engine dimensions with respect to LP impeller and power turbine last stage diameters

	Ratio	Turbomachinery diameters
Maximum width	1.5	Max. between LP impeller and free turbine
Maximum height	2.0	LP impeller

4.2.7. Costs estimation

As with the overall dimensions of the engine, there is a lack of first-order, semiempirical methods to estimate the costs and the development time of a gas turbine engine. [72] provides several basic single and multi-input formulas to estimate development costs, development time, and production costs for turbofan military engines. These cost-estimating relationships were developed through a series of least-square regressions, based on turbofan cost data available as of publication time in 2002. Although these formulas were developed from historical data for engines application different from the ones here examined, these are still useful in the early conceptual design stages of an engine to perform valuable trade-off studies. Formulas for the production costs have been calibrated to match

price data for the reference engine, as explained in Chapter 4.3, by the introduction of a dedicated calibration factor, f_{cost} . In addition, to include the effect of different assumptions on the technology level in the cost estimation, the input technology factor has been linked to the cost calibration factor as follows:

$$f_{cost} = 0.775f_{tech} + 0.225.$$

Finally, it is important to mention that the costs calculated with these formulas are expressed in 2001 \$millions and that they need to be adequately converted by using calculated or predicted (depending on the supposed EIS for the designed engine) inflation rates.

For the estimation of development costs, [72] suggests the use of the following formula for a new centerline development engine:

$$C_{dev} = e^{-24.429+4.027\ln(T_{41}-460)},$$

where T_{41} is the turbine rotor inlet temperature (expressed in Rankine degrees).

For the production costs, [72] suggests two different formulas: one for the first production engine, one for the production of engine number 375. These are as follows:

$$C_{prod}^1 = e^{-10.40-8.550 \ln(slope)+1.162 \ln(T_{41}-460)+0.261\ln(W)},$$

$$C_{prod}^{375} = e^{-10.40+1.162 \ln(T_{41}-460)+0.262\ln(W)},$$

where *slope* is the cost improvement and can be assumed equal to 0.9 for new engines, and W is the dry mass of the engine in pounds.

[72] also provides a semiempirical formula for the estimation of the development time, expressed in months:

$$T_{dev} = e^{-0.243+0.425new+1.151\ln(OPR)},$$

in which *new* should be assumed equal to 1 for new engines, and *OPR* is the design overall pressure ratio of the engine.

4.2.8. Engine limitations

Mechanical and thermal limitations can be assumed to restrict the design space only to those combinations of input parameters that lead to feasible engine configurations.

[63] and [64] provide useful information on the maximum circumferential speed that compressor and turbine blades can be sustained. These indications are summarized in Table 19. Another important mechanical limitation is represented by AN^2 , which is the product of the annulus area of a turbine stage and the square of the turbine rotational speed. For the last stage of the power turbine, its value should be kept below certain limits, as also reported in Table 17, to avoid too high disc stress.

Table 19. Set of mechanical limitations assumed for the analyses

	Upper limit	Reference
Radial compressor exducer tip speed	625 m/s (Ti alloy blades)	[64]
HP turbine average circumferential speed	550 m/s	[63]
LP turbine average circumferential speed	470 m/s	[63]
Power turbine average circumferential speed	400 m/s	[63]
AN^2	$50 \cdot 10^6 \text{ m}^2 \text{ rpm}^2$	[64]

Concerning temperature limitations, these have already been collected in Chapter 4.2.3. Improvements in the maximum allowable temperature mainly derive from adopting more advanced materials, better cooling technology, and improved thermal coatings. These limitations apply to the HP turbine rotor inlet temperature (T_{41}), to the LP turbine inlet temperature (T_{43}) and are recapped in Table 20, along with related assumptions on the technology level.

Table 20. Set of temperature limitations assumed for the analyses

Technology level	Maximum T_{41}	Maximum T_{43}
0.0	1450 K	1200 K
0.2	1550 K	1250 K
0.4	1750 K	1300 K
0.6	1950 K	1350 K
0.8	2050 K	1400 K
1.0	2100 K	1450 K

The last set of limitations has been derived from [64] and comprises typical limitations for radial compressors. These are collected in Table 21.

Table 21. Radial compressor limitations, taken from [64]

	Limit
Pressure ratio	< 10.0
Exducer tip diameter	< 0.8 m
Entry mass flow rate	< 10 kg/s

4.2.9. Emissions

Emissions cannot be directly estimated in GasTurb. The only information provided is the NO_x severity index, which should be multiplied by a coefficient depending on the burner technology, as suggested in [73], to obtain the related EI. For an old technology burner, a coefficient value of 32 is suggested, while for modern combustion chambers, this value can be lowered to 23.

There are several semiempirical methodologies available in the literature for estimating aircraft engine emissions. Most of these are particularly suited for turbofan engines. [74] provides a simple methodology for fast and reasonable predictions of pollutant species emissions for turboprop airplanes. This methodology is based on emissions data collected in the ICAO databank [75], which have been conveniently adapted, through several correlations, to fit the emissions for a turboprop engine.

In order to enable the use of this simplified model, the only information required from the engine model is the fuel flow and the design OPR. This methodology allows the estimation of the EI for the following pollutant species:

- NO_x (nitrogen oxides),
- CO (carbon monoxide),
- HC (hydrocarbons).

It is reasonable to assume that the EI values produced by this model can be believed to be reliable as long as the adopted fuel is conventional jet fuel (i.e., Jet A-1).

Regarding the EI for CO_2 , H_2O , and SO_2 , constant values suggested in [76] and here reported in Table 22 can be reasonably adopted, with the same assumption on the fuel reported above.

Table 22. EI for CO_2 , H_2O , and SO_2 , according to [76]

	EI (grams of pollutant divided by kilograms of fuel burn)
CO_2	3149.0
H_2O	1230.0
SO_2	0.84

4.2.10. Alternative fuels

GasTurb 11 allows choosing between different fuels for the cycle simulations. Conventional jet fuel for civil aircraft applications, Jet A-1, named *Generic Fuel* in GasTurb 11, has been selected as the standard kerosene fuel for the analyses and the GasTurb rubber engine model. GasTurb provides for this fuel a LHV equal to 43.124 MJ/kg at ISA SL static temperature [73]. This value has been adjusted in the present context to consider information provided in [77] on the average LHV for Jet A-1 fuel, which should be about 43.26 MJ/kg. In order to consider the effects related to the use of alternative fuels on the engine thermodynamic cycle, a simplified approach similar to the one presented in [78] has been selected. Different blends of biofuels have been considered by varying the GasTurb input defining LHV. The LHV for these blends have been estimated starting from pure kerosene and pure biofuel LHV values, interpolating linearly for different blends depending on the percent by mass of the mixture. This is a simplified approach since the fuel properties file used by GasTurb for the analysis has not been updated accordingly with the different assumptions on the fuel. A more accurate approach would have required the generation of fuel performance data by using an additional tool, as explained in [77], possibly in the same format required by GasTurb 11 for the input file for fuel properties.

However, cycle simulations, including the effect on the LHV, should still account for the effects of biofuel blends on the thermodynamic cycle of the engine and the fuel consumption, as exemplified in [78].

Hydro-processed esters and fatty acids synthetic paraffinic kerosene (HEFA-SPK) and synthetic paraffinic kerosene derived from the Fischer-Tropsch process (FT-SPK) have been chosen among the set of biofuels certified for civil aviation use. For both these biofuels, blending ratios up to 50% with conventional jet fuel have been already approved, with this value being destined to grow in the coming years since several tests on military aircraft engines are already underway [79]. Moreover, among all the available biofuels, the two typologies selected here have the highest technology readiness level (TRL) for commercialization, according to [80].

Within this context, three fuels have been examined and included in the rubber engine model:

- Conventional kerosene (Jet A-1),
- Conventional kerosene 50 % blend with SPK,
- 100 % SPK biofuel.

Distinctions between the two typologies of biofuel identified above have not been performed in the context of the impact these fuels have on the thermodynamic cycle of the engine. Information on the LHV for these fuels have been collected from [77] and are presented in Table 23. The same reference also provides indications of CO₂ EI (gram of pollutant per kilogram of fuel), which have been conveniently adapted and are collected in Table 23. No additional reliable information has been retrieved from the literature on the impact that biofuel blends may have on the remaining EI.

Table 23. Input values for the LHV and CO₂ EI of the fuels examined for GENESIS, mainly derived from indications included in [77]

Fuel	LHV [MJ/kg]	CO ₂ EI [g/kg]
Jet A-1	43.26	3149.0
SPK 50%	43.65	3124.5
SPK 100%	44.04	3100.0

4.3. Validation and testing for the short-term scenario

The following chapters provide proof of validation of the engine model implemented in GasTurb 11 and an analysis of the short-term scenario results, involving different suppositions for the fuel and the technology level (less/more conservative design).

4.3.1. Validation

In order to validate the rubber engine model implemented in GasTurb, this has been tested using input for the reference engine: the PW127E engine variant. Data for this engine has been mainly collected from [61], [58], [81], [60], and [56], or reasonable assumptions have been performed in case direct information was not available. The design has been carried out under the same conditions listed in Table 12. Table 24 summarizes the selected input variables to the model, while Table 25 lists information on the cycle output and the set of derived output variables.

Assumptions on the power off-takes and the overboard bleed have been performed starting from semi-empirical formulas provided in [82] and in [64], respectively. Information on the aircraft application, such as the number of passengers on board (flight crew included) and the maximum take-off weight, are required to use these formulas. These basic figures have been taken from [59]. The technology factor has been selected based on information from [61] and [81] regarding the turbine materials (Mar M-200 for the HP turbine blades, Inconel 792/100 for the remaining parts, all with a maximum allowable metal temperature around 1250 K, according to [67]) and the cooling air technology (film with convection and trailing edge ejection).

Table 24. Set of input data to the rubber engine model for the PW127E engine

Input variable	Value	Reference	Notes
Shaft power delivered	1790 kW	[58] [60] [56]	Max. T/O power
Inlet mass flow	8.49 kg/s	[61]	-
Burner exit temperature	-	-	Iterated to match target shaft power
Overall pressure ratio	14.7:1	[58]	-
Technology factor	0.2	-	Set to match available information
EIS	1990	[61]	PW127 program start
Power off-takes	14 kW	-	Estimated starting from [74]
Overboard bleed	0.25 kg/s	-	Estimated starting from [64]
FHV	43.26 MJ/kg	-	Conventional kerosene (Jet A-1)

Table 25 gives evidence of the good match between the output from the rubber engine model and the values expected for the reference engine. The differences in terms of performance are quite negligible, especially for the fuel consumption, with a difference at ISA SL static T/O condition lower than 1 %. For the remaining variables, dry mass and overall dimensions, the differences are larger but below 10 %. Moreover, the model also tested well concerning expected boundaries, with the cycle output being compliant with thermal and mechanical limitations.

Table 25. Output cycle and derived variable results for the reference engine

Output variable	Value	Expected value	Reference	Diff.
Equivalent shaft power	1877 kW	1876 kW	[58]	+0.05%
Burner exit temp.	1442 K	1420 – 1530 K	[81]	-
LP turbine inlet temp.	1219 K	below 1220 K	-	-
LP impeller exit velocity	564 m/s	below 625 m/s	-	-
HP turbine mean velocity	469 m/s	below 550 m/s	-	-
LP turbine mean velocity	438 m/s	below 470 m/s	-	-
Free turbine mean vel.	372 m/s	below 400 m/s	-	-
Free turbine AN ²	39*10 ⁶ m ² rpm ²	below 50*10 ⁶ m ² rpm ²	-	-

Cooling relative air	5%	-	-	-
Engine dry mass	492 kg	481 kg	[58] [60]	+2.29%
Engine width	652 mm	660 mm	[58]	-1.21%
Engine height	770 mm	838 mm	[58]	-8.11%
Engine overall length	1979 mm	2134 mm	[58]	-7.26%
SFC @ design point	0.3080 kg/(kW*h) 0.5063 lb/(hp*h)	-	-	
Equivalent SFC @ design point	0.2937 kg/(ekW*h) 0.4828 lb/(ehp*h)	-	-	
Equivalent SFC @ SLS ISA T/O	0.2900 kg/(ekW*h) 0.4768 lb/(ehp*h)	0.4740 lb/(ehp*h)	[58]	+0.59%

Regarding the costs, the formula for estimating the production cost for the 375th engine reported in Chapter 4.2.7 has been used to test the result against price data for 2010 reported in [81]. This formula, with input from the engine design cycle output, provides a \$1,376,200 production cost for 2001, which, once converted to 2010 US dollars by using a 23.2% cumulative rate of inflation, gave a production cost for 2010 equal to \$1,695,500, quite distant from the \$920,000 price tag suggested by [81]. Supposing a 30% profit margin per engine sold, a corrective calibration factor equal to 0.38 was assumed for the costs formulas.

4.3.1. Short-term scenario analysis

For the short-term scenario, technology level factors equal to 0.4 and 0.6 have been considered (for the assumptions on the related technologies, see Chapter 4.2). For the calculation of the EIS correction for the polytropic efficiencies, a value equal to 2030 has been selected, since it has been indicated as the representative year for the short-term scenario. Concerning the fuel, blending ratio up to 50 % with HEFA- and FT-SPK biofuels have been reasonably considered due to their high TRL and the fact that they have already been approved. Since tests are already ongoing for higher blending ratios and certification could be expected in the coming years, blending ratios up to 100 % have been included in this preliminary analysis.

Results have been reported in terms of engine SFC, dry mass, maximum diameter, and production cost. Limitations (most of which have been already reported in Chapter 4.2.8) have been included in the selection to restrict the available design space and allow selecting a reasonable design point. An upper limit has been introduced on the NO_x severity index to have EI NO_x values at a design point lower than 20 g/kg. It is important to remark that NO_x severity index values for these analyses have been directly obtained from the rubber engine model implemented in GasTurb and not from using the semiempirical methodology suggested by [74] and described in Chapter 4.2.9.

Moreover, an upper bound for the cooling air relative flow equal to 5 % has been added to the set of limitations. Such a limitation could be introduced to restrain the complexity of the cooling air system. For the estimation of the production cost, the scaling procedure for turboprop engines, technology level, and US dollar inflation rate described in Chapter 4.2.7 have been adopted. For the 2021-2030 time span, a cumulative inflation rate equal to the one for the 2011-2020 decade has been assumed.

For all the analyses reported in this chapter, the required shaft power at the design point has been kept constant and equal to 1790 kW, the same value of the reference engine. The same applies to the power off-takes and the overboard bleed, which have been kept equal to 14 kW and 0.25 kg/s, respectively. Figure 30 to Figure 33 provide results for 0.4 technology level assumption and 0 % biofuel blending ratio for the main output variables. As can be deduced from these contour plots, the temperature at the inlet of the LP turbine, together with NO_x emissions and cooling air system complexity, restrict the design space to the polygon in the lower-left corner. By choosing as the design point, for example, the point at the intersection between the NO_x and the cooling air limit lines (i.e., the purple and the cyan dashed lines), the results reported in Table 26 are obtained. For the same technology level,

contour plots have also been produced assuming different values for the fuel blending ratio. Figure 34 and Figure 35 provide SFC contours for 50 % and 100 % blending ratios, respectively. Contours for the remaining output variables have not been included since only small variations to the 0 % blending ratio have been observed. Table 27 provides information on the impact of alternative fuels on the SFC for the same advanced engine using standard kerosene and concerning the reference engine model, still using conventional jet fuel.

Table 26. Obtained values for the main output variables for a gas turbine engine designed for the short-term scenario, assuming a value for the technology factor equal to 0.4 and a 0 % blending ratio for the adopted fuel

Variable	Value	Reference engine	Difference
SFC [kg/(kW*h)]	0.2455	0.3080	-20.3 %
Dry mass [kg]	351	481	-28.5 %
Max. diameter [mm]	647	770	-15.9 %
Production cost [M\$]	1.37	-	-

Table 27. Effect of alternative fuels on the fuel consumption for the short-term scenario, for a technology factor equal to 0.4

SFC [kg/(kW*h)]	Value	Difference with respect to 0% fuel blend	Difference with respect to reference engine
Conventional kerosene (0% blending)	0.2455	-	-20.3 %
SPK 50% (HEFA-SPK / FT-SPK)	0.2433	-0.89 %	-21.0 %
SPK 100% (HEFA-SPK / FT-SPK)	0.2412	-1.75 %	-21.7 %

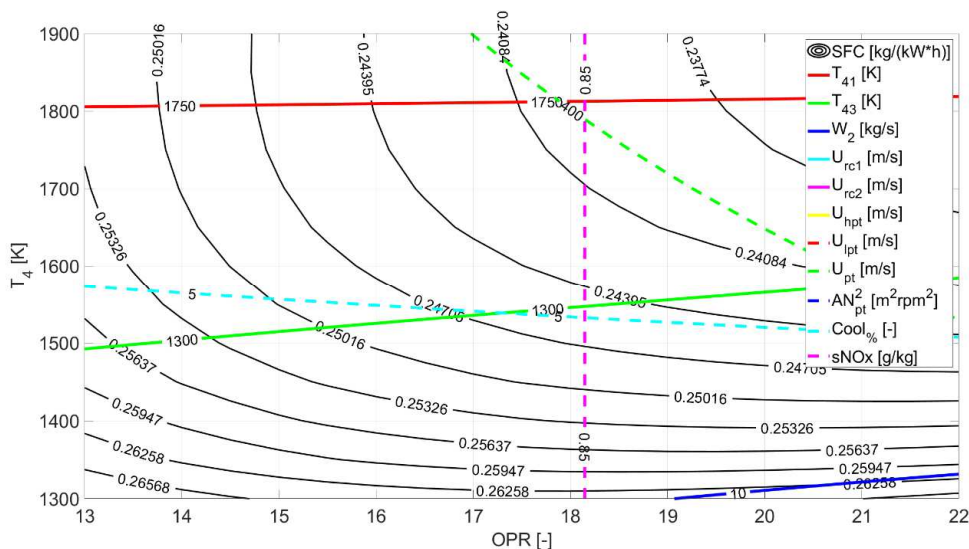


Figure 30. SFC contour plot for technology level 0.4 and 0 % biofuel blending ratio

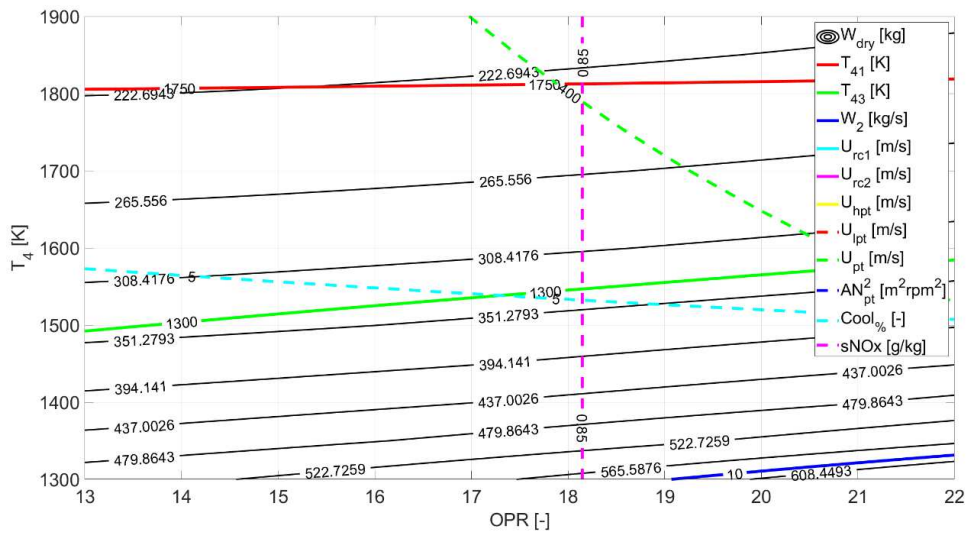


Figure 31. Dry mass contour plot for technology level 0.4 and 0 % biofuel blending ratio

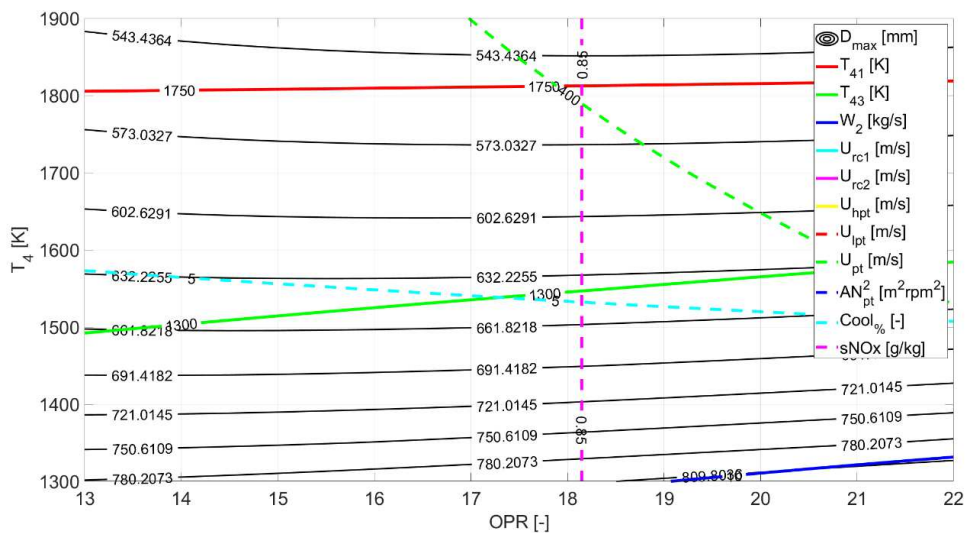


Figure 32. Maximum diameter contour plot for technology level 0.4 and 0 % biofuel blending ratio

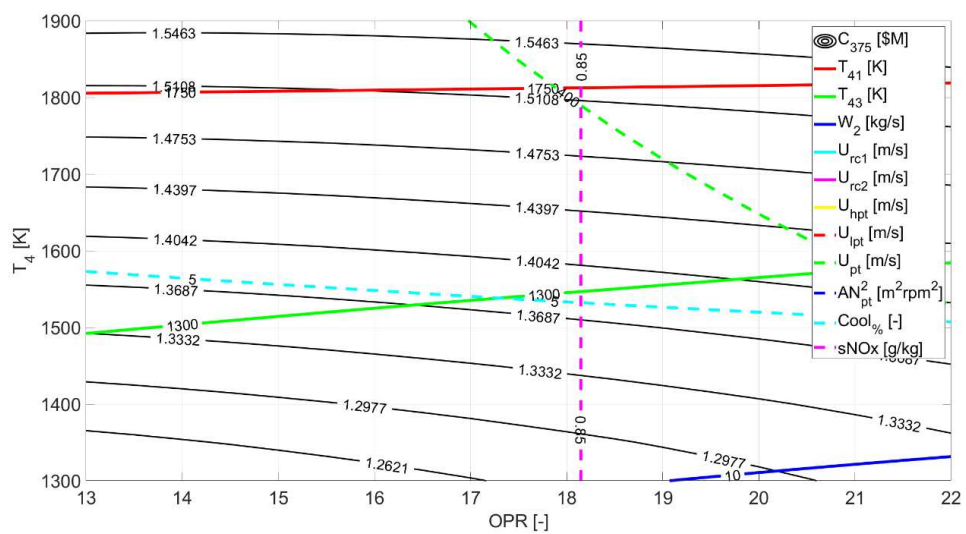


Figure 33. Production cost (375th engine) contour plot for technology level 0.4 and 0 % biofuel blending ratio

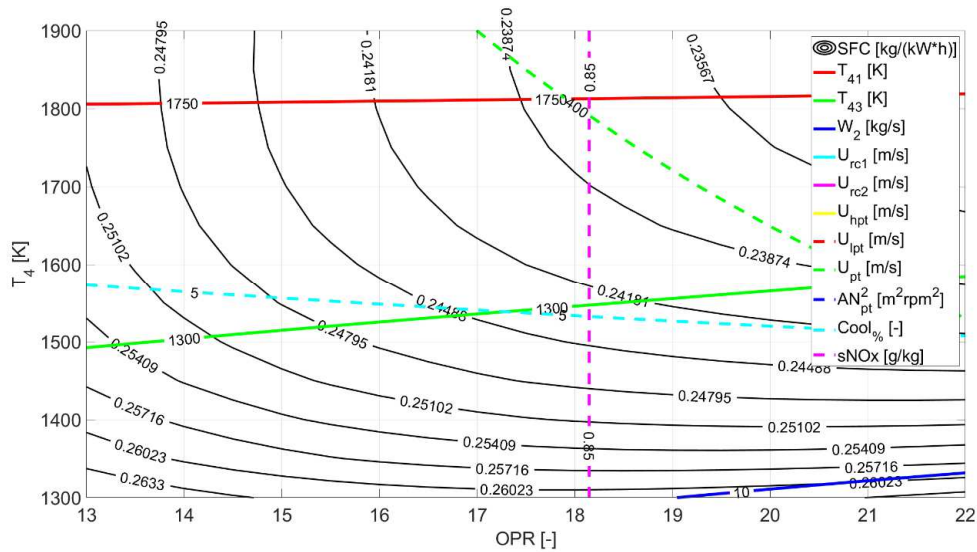


Figure 34. SFC contour plot for technology level 0.4 and 50 % biofuel blending ratio

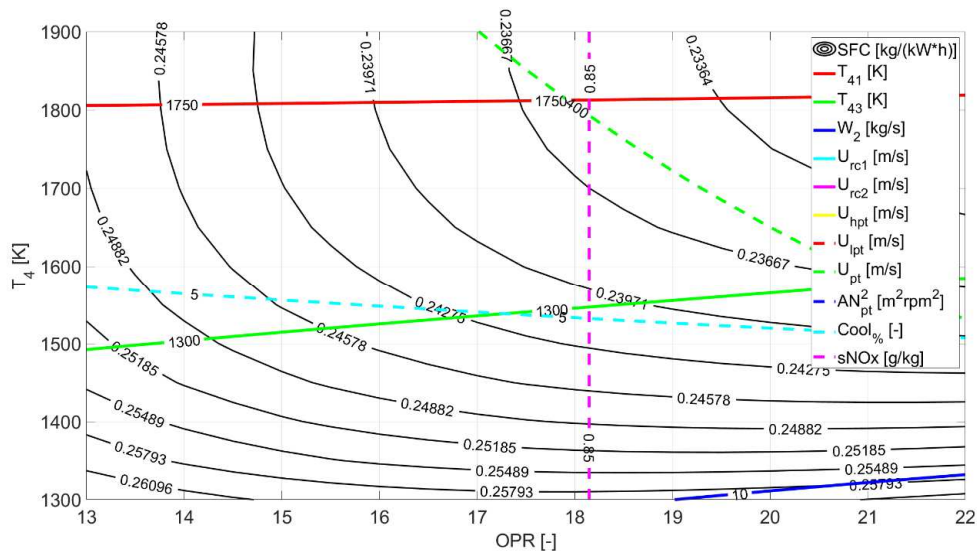


Figure 35. SFC contour plot for technology level 0.4 and 100 % biofuel

The same analyses have been performed assuming a higher technology level, equal to 0.6, for the short-term scenario. Figure 36 to Figure 39 provide contour plots for the fuel consumption, the dry mass, the engine size, and the production cost. As can be seen from these plots, the higher technology level moves upward the limitations provided by the LP turbine entry temperature and the relative airflow for cooling. Moreover, the amount of cooling air required by the HP turbine is no more a limitation to the available design space in this case. What remains the same is the limitation provided by NO_x emissions, which restricts the maximum achievable OPR to a value a little higher than 18:1. As done before, an example design point was chosen, this time at the intersection between the purple dashed line for the NO_x emissions and the light green line for the LP inlet temperature. Results for this design point, assuming conventional kerosene as jet fuel, are recapped in Table 28. Here, they have also been compared to the results previously obtained for the lower technology factor assumption. Finally, Table 29 provides information on the effect of alternative fuels on the SFC for the technology factor 0.6 scenario. The impact is the same as before, with an approximate 1 % decrease in fuel consumption for the 50 % blend and almost 2 % for pure SPK jet fuel.

Table 28. Obtained values for the main output variables for a gas turbine engine designed for the short-term scenario, assuming a value for the technology factor equal to 0.6 and a 0 % blending ratio for the adopted fuel, with a comparative with respect to technology level 0.4 and the reference engine

Variable	Tech. level 0.6	Tech. level 0.4	Reference engine	Tech. 0.6 difference with respect to tech. 0.4	Tech 0.6 difference with respect to ref. engine
SFC [kg/(kW*h)]	0.2296	0.2455	0.3080	-6.5 %	-25.4 %
Dry mass [kg]	285	351	481	-18.8 %	-40.7 %
Max. diameter [mm]	608	647	770	-6.0 %	-21.0 %
Production cost [M\$]	1.79	1.37	-	+30.6 %	-

Table 29. Effect of alternative fuels on the fuel consumption for the short-term scenario, for a technology factor equal to 0.6

SFC [kg/(kW*h)]	Value	Difference with respect to 0 % fuel blend	Difference with respect to reference engine
Conventional kerosene (0% blending)	0.2296	-	-25.4 %
SPK 50% (HEFA-SPK / FT-SPK)	0.2277	-0.83 %	-26.1 %
SPK 100% (HEFA-SPK / FT-SPK)	0.2257	-1.70 %	-26.7 %

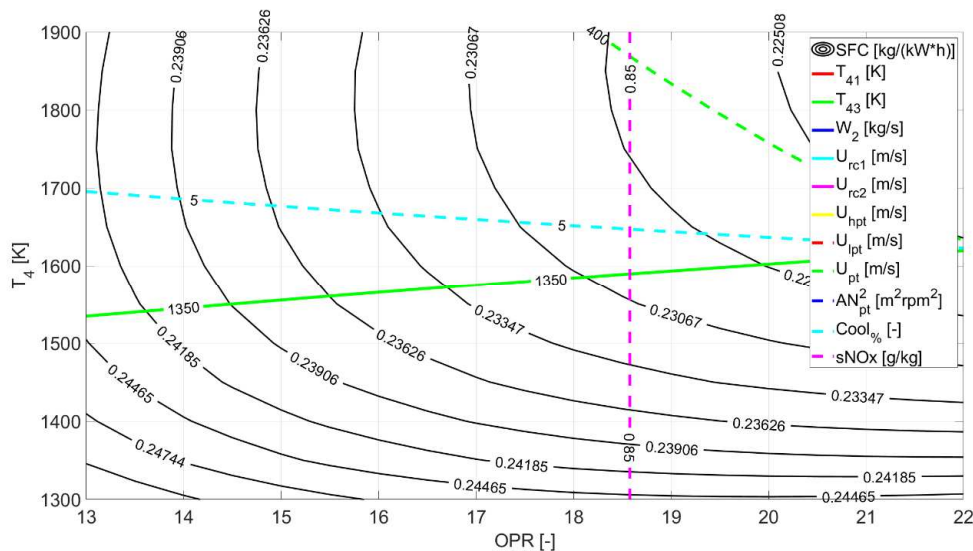


Figure 36. SFC contour plot for technology level 0.6 and 0 % biofuel blending ratio

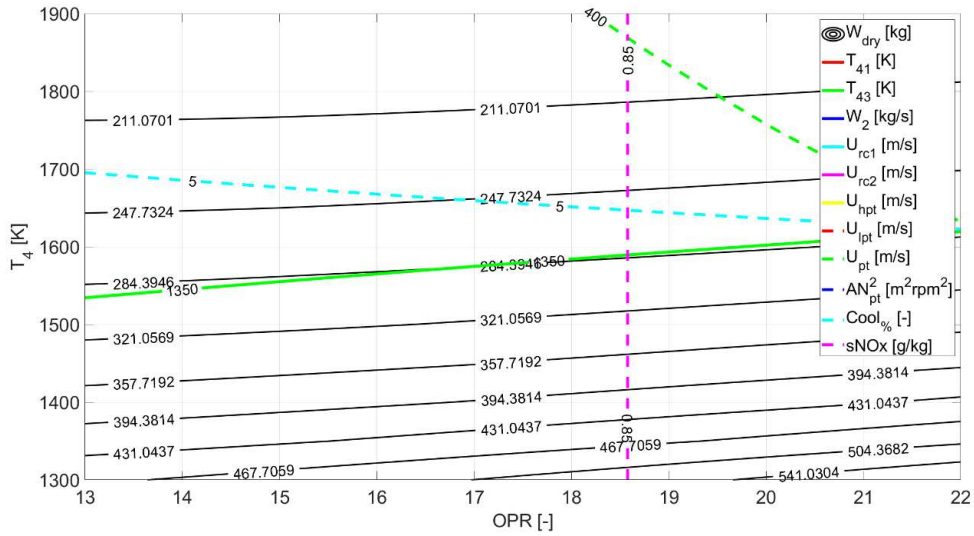


Figure 37. Dry mass contour plot for technology level 0.6 and 0 % biofuel blending ratio

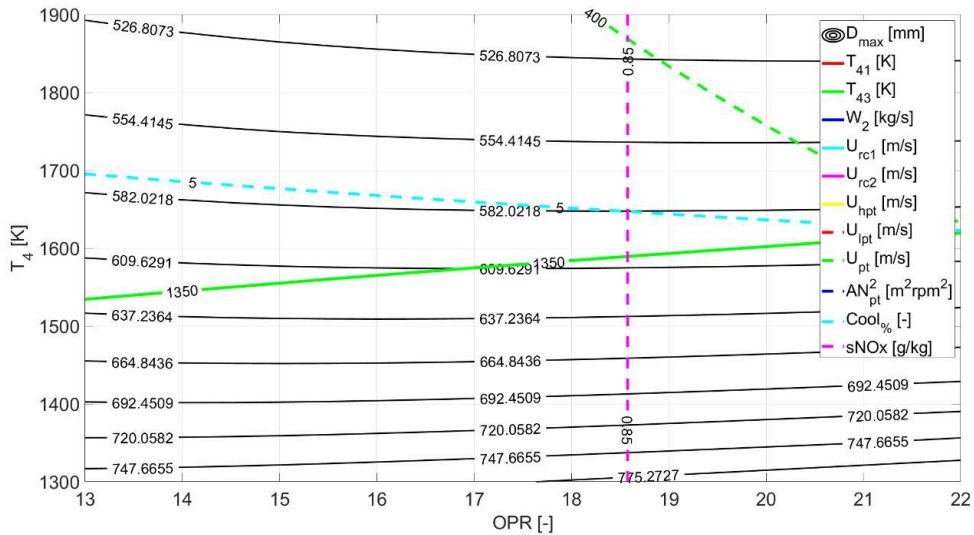


Figure 38. Maximum diameter contour plot for technology level 0.6 and 0 % biofuel blending ratio

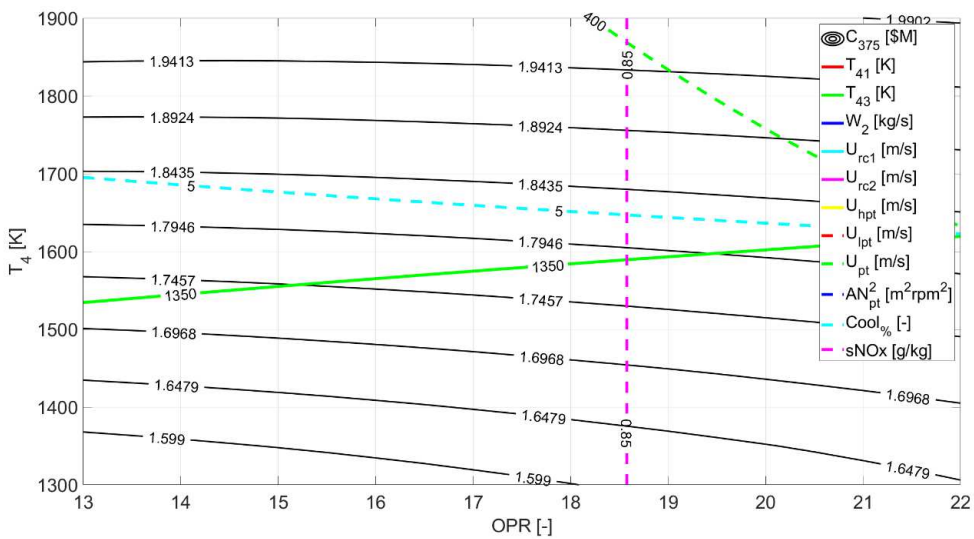


Figure 39. Production cost (375th engine) contour plot for tech level 0.6 and 0 % biofuel blending ratio

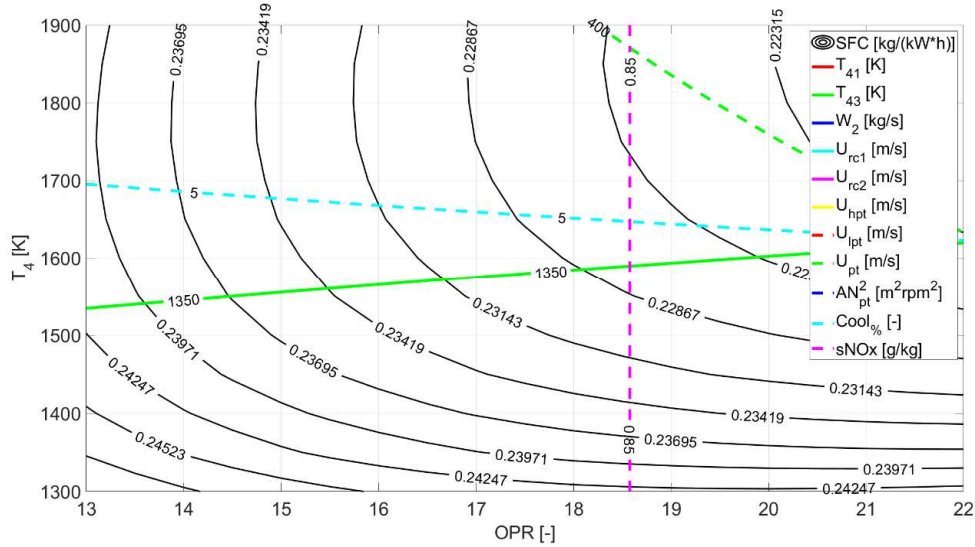


Figure 40. SFC contour plot for technology level 0.6 and 50 % biofuel blending ratio

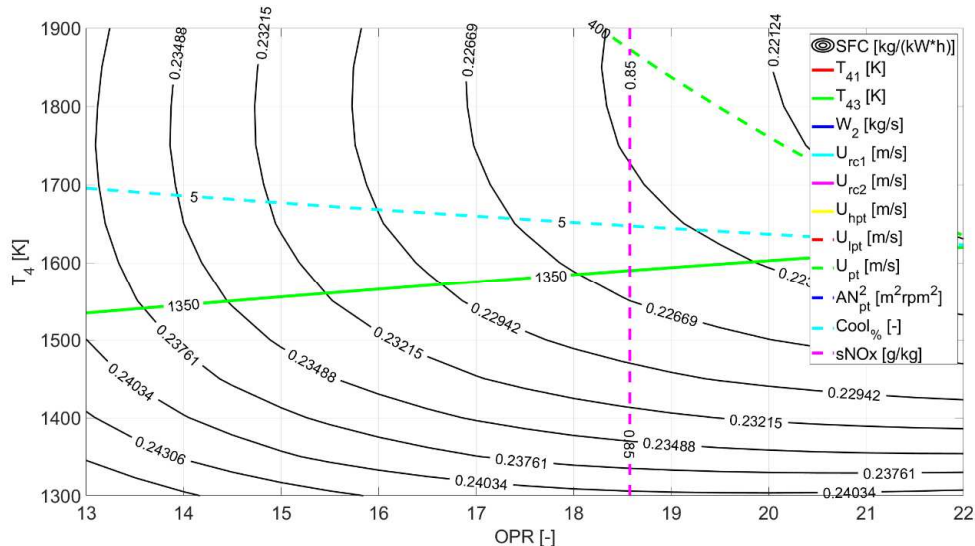


Figure 41. SFC contour plot for technology level 0.6 and 100 % biofuel blending ratio

4.4. Generation of a surrogate engine model

The GasTurb rubber engine model, once implemented with the set of design laws and update rules of Chapter 4.2, has been used to perform several parametric studies, involving the following variables at the design point:

- Shaft power delivered,
- Burner exit temperature,
- Overall pressure ratio,
- Power off-takes,
- Overboard bleed,
- Biofuel blending ratio,
- Entry into service, and
- Technology level factor.

The entry mass flow has been automatically iterated to match the indicated amount of shaft power for a certain combination of input parameters. Table 30 provides an overview of the parametric study performed explicitly for the short-term scenario analysis. Information has been provided here regarding lower and upper boundaries adopted for the parametric analysis, together with step size, for each input variable examined and allowed by the implemented GasTurb rubber engine model.

Table 30. Input for the parametric study for the short-term scenario of GENESIS

Input variable	Lower boundary	Upper boundary	Step
Shaft power delivered	1000 kW	2400 kW	100 kW
Burner exit temperature	1300 K	1700 K	50 K
Overall pressure ratio	13:1	22:1	1
Power off-takes	0.0 kW	50 kW	50 kW
Overboard bleed	0.0 kg/s	0.50 kg/s	0.25 kg/s
Biofuel blending ratio	0.0%	100%	50%
Entry into service	2030	2030	-
Technology level factor	0.4	0.6	0.2

The dataset produced with these parametric studies has been used to train a separate linear regression model for each of the cycle output variables of interest to generate a surrogate model of the engine that could be easily exported and implemented in an external tool to perform trade-off analyses and optimizations at aircraft level. The MATLAB® Regression Learner App [83] has been used for this purpose. This app provides several training models that are even more complicated than the linear one and more flexible to the provided dataset. The main advantages of linear models within this context are their easy interpretability (i.e., simple linear formulas used to perform data regression) and the possibility to easily export the trained model to applications outside the MATLAB® environment.

For the linear model, there are several options provided by the application, especially concerning the terms of the linear model. The application allows to choose between four types of terms:

- Linear (constant term and linear terms);
- Interactions (constant term, linear terms, and interaction terms);
- Pure Quadratic (constant term, linear terms, and purely quadratic terms);
- Quadratic (constant term, linear terms, interaction terms, and purely quadratic terms).

It was tested for each cycle output that the linear model option to fit the dataset best was the quadratic term, providing for each output variable reasonable results in terms of root mean squared errors. The training results are collected in Table 29, along with information on the terms of the model and the residual error.

Table 31. Training results for the surrogate engine model of the short-term scenario

Output variable	Regression model	Terms	R ²
SFC [kg/(kW*h)]	Linear	Quadratic	0.0017
sNO _x [g/kg]	Linear	Quadratic	0.0014
W ₂ [kg/s]	Linear	Quadratic	0.1562
LP exducer Diameter [m]	Linear	Quadratic	0.0024
PT exit Diameter [m]	Linear	Quadratic	0.0024
T ₄₁ [K]	Linear	Quadratic	1.0753
T ₄₃ [K]	Linear	Quadratic	1.7495
LP exducer tip U [m/s]	Linear	Quadratic	0.3739

HP exducer tip U [m/s]	Linear	Quadratic	0.6861
HP turbine average U [m/s]	Linear	Quadratic	1.0946
LP turbine average U [m/s]	Linear	Quadratic	0.9385
PT average U [m/s]	Linear	Quadratic	0.7281
PT AN ² [m ² rpm ² /10 ⁶]	Linear	Quadratic	0.1682
NGV relative cooling [-]	Linear	Quadratic	3.8668*10 ⁻⁴
Rotor relative cooling [-]	Linear	Quadratic	2.3492*10 ⁻⁴

This surrogate model is ready to be included, as it is, in an aircraft design chain, providing information on variations of engine fuel consumption, dry mass, dimensions, emissions, and costs, depending on the chosen set of input variables. Information on the fuel consumption, in particular, can be used to scale an existing deck for SFC. For a simplified approach, the same scaling should be applied to all the engine ratings.

4.5. Conclusions

The approach adopted for modeling a gas turbine engine for the short-term scenario has been presented. Since this approach includes considerations on the technology level and the EIS, it can be easily adapted to the remaining scenarios within the context of GENESIS.

A rubber engine model has been first implemented in GasTurb, by assuming the PW127 engine configuration as the main reference. This model includes considerations on the polytropic efficiencies of the compressors and turbines, the pressure ratios of the radial compressors, the pressure losses along the main ducts, and the cooling air requirements. The setting and the update of these quantities have been automated and linked to the values of several major input variables at the design point, such as the required shaft power, the OPR, and the burner exit temperature, along as well with the values of EIS and technology factor. This enables to keep the design of the gas turbines for future scenarios consistent.

This rubber engine has been tested and calibrated against real-world data of the reference engine and has also been used to carry out representative analyses for the short-term scenario, assuming values for the aircraft requirements in terms of thrust, power off-takes, and overboard bleed. These analyses have helped to provide a glimpse of the expected benefit in terms of fuel burn reduction coming from the gas turbine, in addition to the impact on weight, main dimensions, and costs.

In order to allow trade-off analyses at aircraft level, including effects on the engine, a surrogate model has been developed starting from the rubber engine model implemented in GasTurb. This surrogate model can be easily included in the aircraft design chain. The actual engine model for the short-term scenario will only be defined once that parametric analyses and trade-off studies have been carried out for the hybrid-electric aircraft. Values for engine SFC, dry mass, main dimensions, costs, and EI used throughout the aircraft analysis process will be an output of this surrogate engine model, which already includes assumptions for the short-term scenario regarding efficiencies, cooling air technology, and materials, that have been listed in Chapter 4.2.

5. Power electronics technology analysis

5.1. Introduction

This chapter deals with the short-term (2025-2035) technology analysis for all power electronics converters in the GENESIS project. Figure 42 shows the basic electric architecture of the regional aircraft and all possible existing power electronics converters.

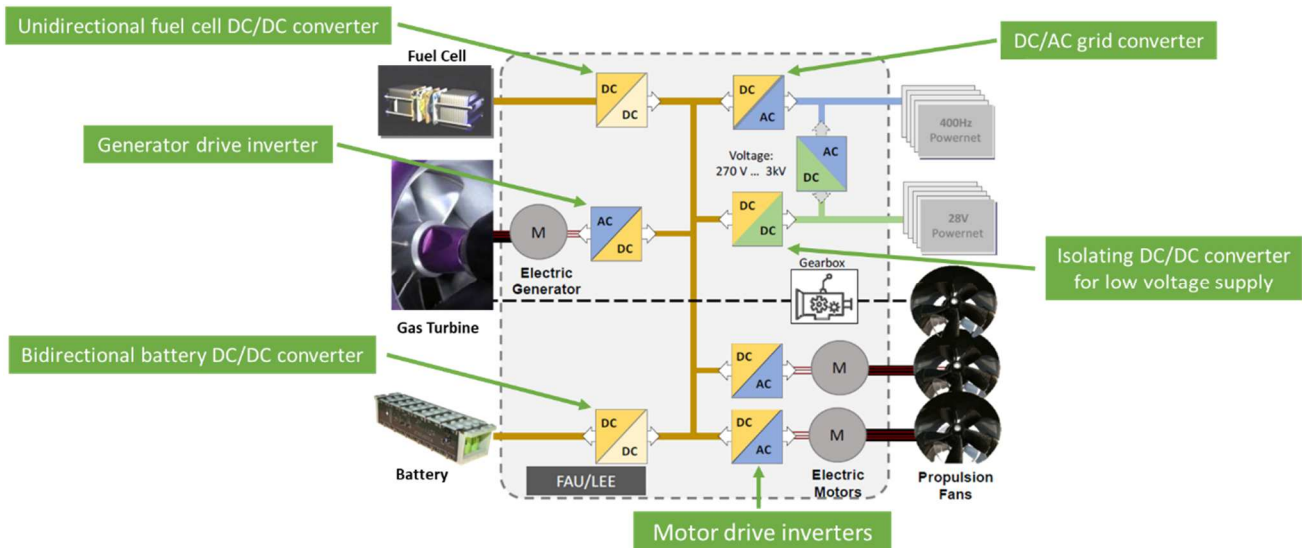


Figure 42. Overview of possible power electronics converters for all time frames

The electric generator (primary electric machine) is driven by the gas turbine and converts mechanical power into electrical power. The output voltage of the electric generator is actively rectified by the generator drive inverter, which will supply the internal (high voltage) HV DC bus. For the HV DC bus, a voltage between 270 V and 3 kV is conceivable. This topic is analyzed in depth in Chapter 5.2 and in the end, a voltage of 800 V was chosen for the short-term time frame. The generator and motor inverters drive the primary and electric motors by generating sinusoidal currents. The electric motors convert electrical into mechanical power and drive the propulsion fans to generate thrust. The bidirectional battery DC/DC converter transfers power between the battery pack with a maximum voltage of 1170 V and the internal 800 V DC bus. Depending on the power flow direction, the bidirectional battery DC/DC converter charges or discharges the battery pack. The DC/AC grid converter transfers power from the internal 800V DC bus to the 400 Hz powernet, which is used to power different aircraft electric consumers like heaters and hydraulic pumps. The isolating DC/DC converter for low voltage supply transfers power from the internal 800V DC bus to the 28 V powernet. Depending on the redundancy concept of the aircraft, there could also be an AC/DC grid to low voltage (LV) converter. It can transfer power directly between the 400 Hz and 28 V powernet if there is an outage of the DC/AC grid converter or the isolating DC/DC converter for low voltage supply. For this report, the AC/DC grid to LV converter is neglected because, at the moment, there is planned to have two DC/AC grid converters and two isolating DC/DC converters for low voltage supply. So, a single outage of a converter can already be compensated. Table 32 shows the considered power electronics components for the short-term period. It is assumed that all converters are liquid-cooled to increase the power density. Air-cooled converters need big heatsinks, and therefore they are bigger and heavier.

Table 32. Power electronics components for the short-term period

Power electronics component	Number of units	Reference power in kW
Generator drive inverter	2	1200
Motor drive inverter	8	600
Bidirectional battery DC/DC converter	2	1200
DC/AC grid converter	2	30
Isolating DC/DC converter for low voltage supply	5	11.2

5.2. Choice of HV DC bus voltage

The internal HV DC bus voltage is a very important parameter for all power electronics converters. It influences many different topics, which are briefly discussed below. Four different voltage levels (800 V, 1500 V, 2000 V, 3000 V) have been chosen for the analysis. A HV DC bus voltage of 800 V is a popular choice for the newest battery electric vehicle (BEV) generation. Many experience and field data are already available for this voltage class. Higher voltage levels above 1 kV are discussed by many aircraft manufacturers, but there are safety concerns and empirical values are missing.

5.2.1. Creepage and clearance distances

The higher the HV DC bus voltage, the higher the creepage and clearance distances have to be. Consequently, the physical size of the power electronics converters can be negatively affected if the creepage and clearances distances become too high. A first rough assessment has been carried out according to the standard IEC EN60664-1 to give insight into the dependency from different HV DC bus voltages levels. The pollution degree 2 (normally only non-conductive pollution occurs, temporary conductivity caused by condensation is expected) has been used for the analysis. The dielectric strength of air decreases with the air pressure and therefore with the installation altitude. This is known as Paschen's law. For installation altitudes above 2000 m above sea level, the clearance distances have to be increased by an altitude correction factor [84]. The altitude correction factor according to the standard EN60664-1 is given in Table 33.

For a typical flight altitude of 25000 feet (= 7600 meters), a correction factor of 2.13 has to be applied. The clearance distances depend on the impulse withstand voltages, which have been derived from the maximum breakdown voltages of the power semiconductors and the HV DC bus voltage. Table 34 shows the result of the insulation coordination analysis for the creepage and clearance distances.

Table 33. Altitude correction factor according to IEC EN60664

Altitude in m	Barometric pressure in hPa	Multiplication factor for clearance
2000	800	1.00
3000	700	1.14
4000	620	1.29
5000	540	1.48
6000	470	1.70
7000	410	1.95
8000	355	2.25

Table 34. Creepage and clearance distances for different HV DC bus voltages

V_{DC}	Creepage distance	Impulse withstand voltage	Clearance distance for < 2000 m altitude	Clearance distance for 7600 m altitude
800 V	4.0 mm	1200 V	0.2 mm	0.43 mm
1500 V	7.5 mm	2300 V	0.5 mm	1.07 mm
2000 V	10.0 mm	3080 V	1.0 mm	2.13 mm
3000 V	15.0 mm	4600 V	2.0 mm	4.26 mm

5.2.2. Influence on power distribution cables

It is evident that with higher DC bus voltages, the current levels will decrease. Therefore, the cable cross-section of the power distribution cables and the cable weight can be reduced. DC transmission cables are built with a circular conductor material composed of copper or aluminium. The circular conductor is surrounded by a concentric layer of insulation material. The thickness and kind of the insulation material depends on the voltage level and has to be sized by an insulation coordination. Often, a cable shield is also used to reduce electromagnetic interference (EMI). The DC transmission cables have to be sized by an electrical and thermal analysis. The electric analysis provides the values for the cable resistance and the ohmic losses in the cable. The losses have to be dissipated by natural heat convection and heat radiation. The thermal analysis dictates the cable cross-section in such a way that the conductor temperature stays below the maximum admissible conductor temperature (e.g. 180°C). The sizing parameters are fixed by the application and use cases, so that only the conductor material, i.e., copper or aluminium, can be freely chosen [85].

The conductivity of aluminium is 39 percent lower than the conductivity of copper. However, as the density for aluminium is distinctly lower, aluminium has only 30 percent of the weight of copper. For the same electrical resistance a bare wire of aluminium weighs half as much as a bare wire of copper. Therefore, a mass advantage can be recognized in the case of aluminum cables, and they are recommended for usage in the GENESIS project.

5.2.3. Derating due to cosmic radiation

It should be noted that power semiconductors at high altitudes are prone to cosmic radiation-induced failures because of the increased particle flux. High-energy particles can generate “single event burnout” failures. Measurements show that the applied DC link voltage should be limited to 50 percent of the devices breakdown voltage for silicon devices (IGBTs = insulated-gate bipolar transistors) and to 65 percent of the devices breakdown voltage for silicon carbide devices (SiC-MOSFETs = silicon carbide metal oxide semiconductor field-effect transistors) to preserve low failure rates [86].

5.2.4. Derating due to switch-off overvoltage

One important goal in power electronics application is to minimize the stray inductance in the power switching loop. A high parasitic inductance will lead to high over-voltage spikes during the switching events, requiring a higher breakdown voltage rating of the power semiconductors. The DC bus voltage has normally to be limited between 60 and 70 percent of the breakdown voltage. For example, for an 800 V DC bus, 1200 V rated power semiconductors and for a 400 V DC bus, 650 V rated power semiconductors are recommended.

5.2.5. Breakdown voltage ratings of power semiconductors

The breakdown voltage of power semiconductors is the largest reverse voltage that can be safely applied without destroying the part, e.g., due to avalanche breakdown. The breakdown voltage of the power semiconductors cannot be chosen arbitrarily. There are some distinct voltage levels, which can be chosen from, e.g., 650 V, 750 V, 900 V, 1200 V, 1700 V, 3300 V, and 6500 V.

5.2.6. Power electronics topology (multilevel converters vs. two-level converters)

To tackle the problem of high breakdown voltages, multi-level converters can be used, which reduce the voltage stress of individual power semiconductors. The underlying basic idea is to connect two or more power semiconductors in series. In a three-level converter, the necessary breakdown voltage is reduced by 50 percent. Three examples of three-level converter legs are shown in Figure 43. In a five-level converter, the necessary breakdown voltage is reduced to 25 percent compared to a standard two-level converter. Table 35 shows the minimum necessary breakdown voltages and Table 36 shows suitable power semiconductor classes for different DC link voltages and converter topologies, whereas the voltage derating regarding cosmic radiation is also considered.

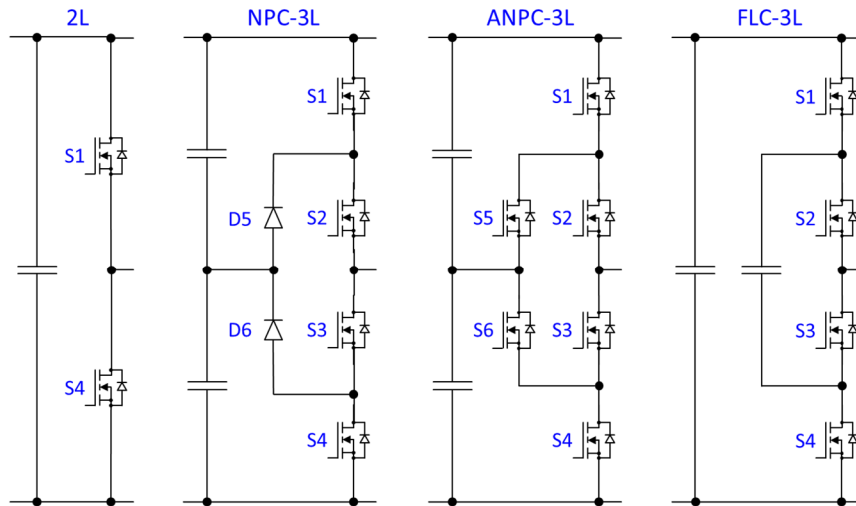


Figure 43. Inverter legs of different inverter topologies: 2L, NPC-3L, ANPC-3L, and FLC-3L

Table 35. Minimum breakdown voltage ratings for different DC link voltages

V_{DC}	Minimum breakdown voltage ratings for 2-level converter		Minimum breakdown voltage ratings for 3-level converter		Minimum breakdown voltage ratings for 5-level converter	
	$V_{DC} / 50\%$	$V_{DC} / 65\%$	$0.5 \cdot V_{DC} / 50\%$	$0.5 \cdot V_{DC} / 65\%$	$0.25 \cdot V_{DC} / 50\%$	$0.25 \cdot V_{DC} / 65\%$
800 V	1600 V	1230 V	800 V	615 V	400 V	308 V
1500 V	3000 V	2308 V	1500 V	1154 V	750 V	577 V
2000 V	4000 V	3077 V	2000 V	1538 V	1000 V	769 V
3000 V	6000 V	4615 V	3000 V	2308 V	1500 V	1154 V

Table 36. Suitable devices for different DC link voltages and converter topologies

V_{DC}	Suitable devices for 2-level converter		Suitable devices for 3-level converter		Suitable devices for 5-level converter	
	$V_{DC} / 65\%$	$V_{DC} / 65\%$	$0.5 \cdot V_{DC} / 50\%$	$0.5 \cdot V_{DC} / 65\%$	$0.25 \cdot V_{DC} / 50\%$	$0.25 \cdot V_{DC} / 65\%$
800 V	1.7 kV IGBT	1.2 kV SiC MOSFET	900V IGBT	650 V SiC MOSFET	650 V IGBT	650V SiC MOSFET
1500 V	3.3 kV IGBT	3.3 kV SiC MOSFET	1.7 kV IGBT	1.2 kV SiC MOSFET	750V IGBT	650V SiC MOSFET
2000 V	4.5 kV IGBT	3.3 kV SiC MOSFET	3.3 kV IGBT	1.7 kV SiC MOSFET	1.2 kV IGBT	900V SiC MOSFET
3000 V	6.5 kV IGBT	6.5 kV SiC MOSFET	3.3 kV IGBT	3.3 kV SiC MOSFET	1.7 kV IGBT	1.2 kV SiC MOSFET

The choice of power semiconductors and the converter topology are the major issues for the losses of the power electronics system. As shown in Chapter 5.3, only SiC MOSFETs are regarded for the short-term time frame of the GENESIS project. For a two-level converter and a DC voltage of 800 V, the usage of mature 1.2 kV SiC MOSFETs is possible. This is favorable because there are a large number of such devices from different manufacturers available today. The number and maturity of available 1.7 kV and 3.3 kV SiC MOSFET is still very limited. For a three-level or five-level converter, the needed amounts of power semiconductors and gate drivers increase dramatically. However, devices with lower blocking voltages, and therefore lower conduction and switching losses

can be used. Another disadvantage is that the reliability will decrease for multi-level inverters as the number of devices and failure cases are increased.

5.2.7. Conclusion

As shown above, the HV DC bus voltage level influences many different topics. The main reason for higher DC bus voltages would be the possibility to reduce the weight of power distribution cables. All other factors favor lower DC bus voltages. Therefore, a HV DC bus voltage of 800 V is recommended for the short-term time frame (2025-2035) of the GENESIS project.

5.3. Choice of power semiconductors

The main components for all power electronic converters are the power semiconductors. They have a big influence on the system design and the system properties. For many years, silicon-based power semiconductors were used in all power electronics applications. For low voltage applications, silicon (Si) MOSFETs and for high voltage applications, silicon IGBTs were used. Roughly ten years ago, the first wide bandgap (WBG) power semiconductors based on silicon carbide (SiC) and gallium nitride (GaN) came on to the market [87] [88]. WBG devices are a disruptive technology that is beginning to get market traction as it displaces silicon-based technologies in various key power electronics markets. The SiC power device revenue is expected to rise from \$592M in 2020 to \$2562M in 2025 with a compound annual growth rate of about 30% [89] with battery electric vehicles (BEV) as the main driver. The GaN power device revenue is expected to rise from \$47M in 2020 to \$1107M in 2025 with a compound annual growth rate of about 70% with the consumer market as the main driver [90].

Silicon carbide and gallium nitride are wide bandgap materials with a comparably large bandgap than other semiconductor materials. This enables the realization of transistors with high blocking voltages and low on-resistance simultaneously, especially compared to silicon-based semiconductors. Table 37 compares the properties of the semiconductor materials Si, SiC, and GaN (see also Figure 44). The higher critical field of SiC and GaN underlines their usability at high voltages, the higher thermal conductivity of SiC facilitates the thermal management. SiC and GaN power semiconductors enable the realization of power electronic systems with the highest power densities, efficiencies, and switching frequencies. This is due to the significantly reduced switching and conduction losses of these wide bandgap semiconductors compared to state-of-the-art silicon-based IGBTs and MOSFETs.

Table 37. Comparison of material properties

Materials property	Si	SiC-4H	GaN
Band gap (eV)	1.1	3.2	3.4
Critical field (10^6 V/cm)	0.3	3.0	3.5
Electron mobility ($\text{cm}^2/(\text{Vs})$)	1450	900	2000
Electron saturation velocity (10^6 cm/s)	10	22	25
Thermal conductivity (W/(cmK))	1.5	3.7	1.3

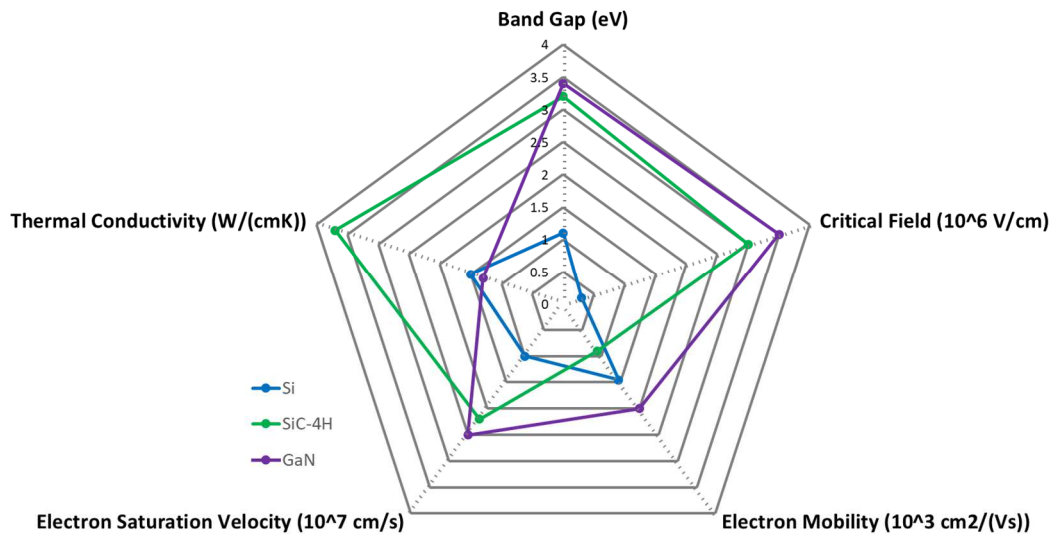


Figure 44. Comparison of material properties

For silicon-based semiconductors, an important choice is whether to use MOSFETs or IGBTs. IGBTs have a different internal build-up than MOSFETs. IGBTs have an additional PN junction that blocks reverse current flow, meaning that IGBTs cannot conduct current in reverse direction like MOSFETs. For an inverter application, an additional diode antiparallel to the IGBT is needed. Si MOSFETs, SiC MOSFETs, and GaN MOSFETs offer, in contrast to IGBTs, the possibility to conduct current in both directions with a so-called “body diode”. This characteristic is used to carry the freewheeling current in inverter applications without additional external diodes. After the commutation process of the current is finalized, the transistors are turned-on again and their internal channel is used as freewheeling-path (synchronous rectification). Another drawback of IGBTs is that they are bipolar devices and large presence of minority carriers leads to long-tail currents during turn-off events and, therefore, to high turn-off losses. Additionally, the on-state forward voltage drop in IGBTs behaves very differently from power MOSFETs. The MOSFET voltage drop can be modelled as a resistance, with the voltage drop proportional to the current. By contrast, the IGBT has a diode-like voltage drop increasing only with the log of the current (see also Figure 45).

For the chosen 800 V DC bus voltage of the aircraft, it should be noted that only silicon IGBT can (normally) be considered for this voltage class. Silicon MOSFETs are only used for lower DC bus voltages. However, for wide bandgap materials, the situation is different. For these materials, power semiconductors are only used in a MOSFET structure nowadays. As of today, there is no GaN IGBT available, and there is some research work regarding SiC IGBTs ongoing. Still, there is no commercial product available due to the intrinsic defects and immature fabrication process [91].

GaN is the newest class of market-available semiconductors with ongoing R&D work and technical improvement. All currently available GaN-transistors are lateral semiconductors as vertical GaN-technology is still in a research state with unknown readiness for market. The technology leap to vertical GaN would offer huge benefits like significantly reduced specific on-resistance, higher current densities, and more even heat distribution. Overall, the competitiveness of GaN will strongly depend on its technological advancement within the next years. Today, only a few GaN devices are available with blocking voltages of 900 V and 1200 V. They cannot compete with silicon and silicon carbide devices regarding the specific on-resistance. Therefore, it was decided that for the short-term (2025-2035) technology analysis, GaN devices are not considered. For the other time frames, they will be an interesting alternative to silicon carbide devices. Comparing gallium nitride and silicon carbide devices, it can be said that in the near future GaN devices will be mostly used for lower voltage, lower power, and higher frequency (>100 kHz) applications (e.g., portable chargers for

mobile phones, notebooks, etc.) [89]. SiC devices will be used for higher voltage, higher power, and medium frequency (<100 kHz) applications [90].

Overall, it can be concluded that silicon carbide devices have many advantages regarding electrical properties compared to silicon devices (see Table 38). The only real drawback of SiC devices is that nowadays, they are a lot more expensive. With growing demand, production ramp-up, and bigger wafer sizes, the price is expected to drop. Even if there will be no price equality at device level, silicon carbide can bring advantages at system level. For example, the battery size can be reduced if power converters using silicon carbide power semiconductors have higher efficiency. SiC devices also allow the usage of higher switching frequencies that reduce the size and weight of passive components (capacitors, inductors, transformers) and hence the size and weight of the power converters. This is very advantageous for aircraft applications. Altogether, it can be concluded that for the short-term analysis (2025-2035) in the GENESIS project, silicon carbide power semiconductors (SiC MOSFETs) are the best option for all power converters. Some examples of commercially available SiC MOSFETs, considered for the power electronics converters, are shown in Table 39.

Table 38. Comparison of Si MOSFETs, Si IGBTs, and SiC MOSFETs properties [89]

Parameter	Si MOSFET	Si IGBT	SiC MOSFET
Device type	unipolar	bipolar	unipolar
Breakdown voltage	12 V to 650 V	400 V to about 12 kV	600 V to several kV
Current density	medium	high	very high
On-resistance $R_{DS(on)}$	medium	medium	low
Conduction losses	medium	medium	low
Switching speed	high	low	very high
Switching losses	medium	high	low
Cost	low	medium	high
Thermal conductivity	low	low	high

Table 39. Some examples for market available SiC MOSFETs with low on-resistance values

SiC MOSFET	Package	V_{DS} in V	$R_{DS(on),25^{\circ}C}$ in $m\Omega$	$R_{DS(on),125^{\circ}C}$ in $m\Omega$	E_{on} in mJ	E_{off} in mJ	E_{ges} in mJ	I_{ref} in A	U_{ref} in V
SiC MOSFET A	Bare-Die	1200	9	13.3	3.50	0.70	4.20	100	800
SiC MOSFET B	Bare-Die	1200	16	24.8	2.82	0.15	2.97	80	800
SiC MOSFET C	Bare-Die	1200	16	21.6	2.12	0.62	2.74	75	800
SiC MOSFET D	Bare-Die	1200	16	22.4	6.25	1.10	7.35	100	800
SiC MOSFET E	Bare-Die	1700	20	34.0	0.77	0.23	1.00	75	1200

5.4. Motor and generator traction drive inverters

5.4.1. Introduction

This chapter deals with the technology analysis for the motor and generator traction drive inverters. As described in Chapter 6.2 for the primary machines (generators), two secondary machines (motors) are stacked together and connected with a common rotor shaft. Accordingly, two motor drive inverters will be used as generator drive inverters. The secondary machine will be a six-phase machine, which will be driven by a six-phase motor drive inverter. The primary machine will be a two-times stacked six-phase machine, which will be driven by two six-phase motor inverters.

5.4.2. Calculation of power losses

One approach to determine the inverter efficiency is to calculate the losses for different operating points with analytic formulas as given in [92]. The losses in the DC link capacitor and the losses in the bus bars are neglected. The driving losses and the blocking losses are negligible for the given application. Dead time losses are also neglected here. Therefore, the total power losses of a transistor P_{tot} are the sum of the switching losses P_{sw} and conduction losses P_{cond} :

$$P_{tot} = P_{sw} + P_{cond}$$

If a linear dependence of the switching energies from the voltage and current levels is assumed, then the total switching losses for a two-level inverter are given by [92]:

$$P_{sw} = 6 \cdot f_{sw} \cdot (E_{on} + E_{off} + E_{rr}) \cdot \frac{1}{\pi} \cdot \frac{\hat{i}}{I_{ref}} \cdot \frac{V_{DC}}{V_{ref}}$$

Where f_{sw} is the switching frequency, E_{on} is the turn-on switching energy, E_{off} is the turn-off switching energy, E_{rr} is the reverse-recovery energy, V_{DC} is the DC link voltage, V_{ref} is the reference voltage, and I_{ref} is the reference current.

The linear dependence of the switching energies from the current and voltage levels is an approximation. The temperature dependence is here also neglected for the numeric calculations, which is more important for IGBTs. The temperature dependence of the switching losses is small for SiC-MOSFETs and can be neglected for a first rough analytic design of the system. As stated in Chapter 5.3, the voltage drop across the transistors during the on-state differs for bipolar (IGBTs) and unipolar (MOSFETs) transistors. The voltage drop can be approximated according to Figure 45.

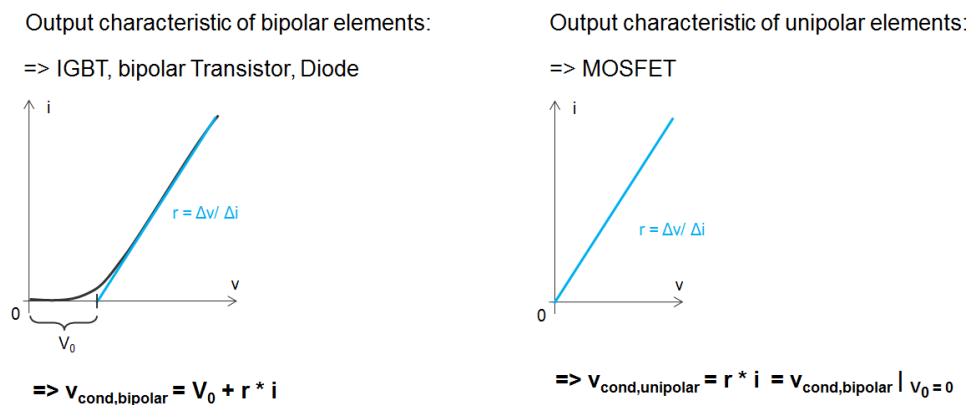


Figure 45. Calculation of voltage drop for bipolar and unipolar semiconductors

For an unipolar transistor (MOSFET) with synchronous rectification, the conduction losses for the transistor $P_{cond,T,unipolar}$ and the internal body diode $P_{cond,D,unipolar}$ are:

$$P_{cond,T,unipolar} = r_{DS(on)} \cdot \hat{i}^2 \cdot \left(\frac{1}{8} + \frac{m \cdot \cos(\varphi)}{3\pi} \right)$$

$$P_{cond,D,unipolar} = r_F \cdot \hat{i}^2 \cdot \left(\frac{1}{8} - \frac{m \cdot \cos(\varphi)}{3\pi} \right) = r_{DS(on)} \cdot \hat{i}^2 \cdot \left(\frac{1}{8} - \frac{m \cdot \cos(\varphi)}{3\pi} \right)$$

Where $r_{DS(on)}$ is the on-resistance of the MOSFET, \hat{i} is the peak output current, m is the modulation index, $\cos(\varphi)$ is the power factor, and r_F is the linearized on-resistance of the diode. Here, it is assumed that the on-state resistance for the MOSFETs is approximately the same for the first and third quadrant for the same gate-source voltage. The total conduction losses $P_{cond,unipolar}$ for a two-level inverter with unipolar transistors (MOSFETs) and synchronous rectification are:

$$P_{cond,unipolar} = 6 \cdot (P_{cond,T,unipolar} + P_{cond,D,unipolar}) = \frac{3}{2} \cdot r_{DS(on)} \cdot \hat{i}^2$$

For high output currents, a parallel connection of two or more power devices is necessary. The total switching losses $P_{sw,T(n)}$ for a parallel connection of n transistors can be calculated as:

$$P_{sw,T(n)} = P_{sw,T} = f_{sw} \cdot (E_{on} + E_{off}) \cdot \frac{1}{\pi} \cdot \frac{\hat{i}}{I_{ref}} \cdot \frac{V_{DC}}{V_{ref}}$$

This means the total switching losses are independent of a parallel connection of several transistors. It is assumed that the current is equally shared between the devices, so each transistor generates $1/n$ switching losses. The same applies to the switching losses of the diodes $P_{sw,D(n)}$:

$$P_{sw,D(n)} = P_{sw,D} = f_{sw} \cdot E_{rr} \cdot \frac{1}{\pi} \cdot \frac{\hat{i}}{I_{ref}} \cdot \frac{V_{DC}}{V_{ref}}$$

The total switching losses $P_{sw}(n)$ for the two-level inverter with a parallel connection of n devices are:

$$P_{sw}(n) = P_{sw} = 6 \cdot (P_{sw,T} + P_{sw,D}) = 6 \cdot f_{sw} \cdot (E_{on} + E_{off} + E_{rr}) \cdot \frac{1}{\pi} \cdot \frac{\hat{i}}{I_{ref}} \cdot \frac{V_{DC}}{V_{ref}}$$

The transistor conduction losses $P_{cond,T,unipolar}(n)$ and diode conduction losses $P_{cond,D,unipolar}(n)$ for a parallel connection of n unipolar transistors with synchronous rectification can be calculated as:

$$P_{cond,T,unipolar}(n) = \frac{r_{DS(on)}}{n} \cdot \hat{i}^2 \cdot \left(\frac{1}{8} + \frac{m \cdot \cos(\varphi)}{3\pi} \right)$$

$$P_{cond,D,unipolar}(n) = \frac{r_F}{n} \cdot \hat{i}^2 \cdot \left(\frac{1}{8} - \frac{m \cdot \cos(\varphi)}{3\pi} \right) = \frac{r_{DS(on)}}{n} \cdot \hat{i}^2 \cdot \left(\frac{1}{8} - \frac{m \cdot \cos(\varphi)}{3\pi} \right)$$

The total conduction losses $P_{cond,unipolar}(n)$ for a parallel connection of n unipolar transistors with synchronous rectification for a two-level inverter are:

$$P_{cond,unipolar}(n) = 6 \cdot (P_{cond,T,unipolar}(n) + P_{cond,D,unipolar}(n)) = \frac{3}{2} \cdot \frac{r_{DS(on)}}{n} \cdot \hat{i}^2$$

An iterative calculation would be necessary for a more accurate estimation of the power losses for each operating point. The on-resistance and the switching energies of power semiconductors are temperature-dependent, and so are the conduction and switching losses. The junction temperature will rise until a temperature balance is reached between the generated losses and the cooling. Another possibility for estimating the inverter power losses is to use a simulation model, and the software tool PLECS[®] (= piecewise linear electrical circuit simulation) developed by Plexim can be used for such a task. Wolfspeed, the market leader in SiC production, has an online tool called “SpeedFit Design Simulator”, which uses the software tool PLECS to estimate the losses of an inverter system based on input parameters such as operating point, switching frequency, and cooling conditions. The datasheet parameters of different SiC MOSFETs and power modules are already included in the given simulation model. The results for the power losses of the motor and generator traction drive inverters obtained by the “SpeedFit Design Simulator” are shown in Chapter 5.4.5.

5.4.3. Six-phase vs. three-phase motor and inverter configuration

First, the losses have been calculated and simulated for a three-phase inverter used in a classic three-phase motor system belonging to the secondary electric machines. The primary electric machines are supplied by two identical inverters, also used for the secondary electric machines. The analysis showed that, for this system configuration, two power modules per phase would have to be connected in parallel to reduce the losses and not to exceed the current capability of the power modules. To avoid the parallel connection of two power modules, it is also possible to use a six-phase motor system with two separated star points (see Figure 46).

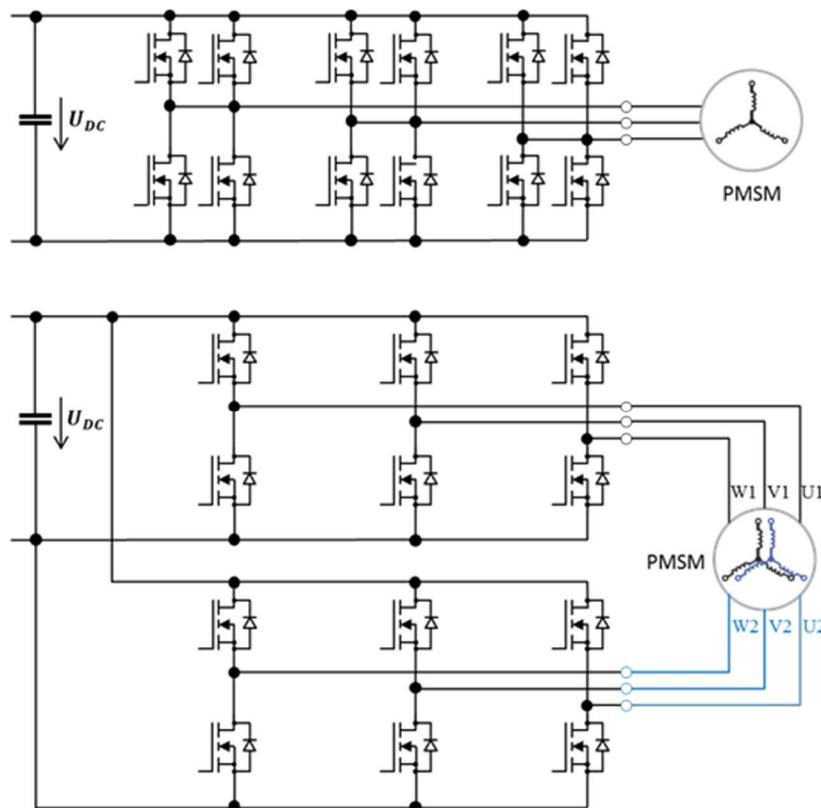


Figure 46. Three-phase topology with paralleled devices (top) and six-phase topology (bottom)

For the three-phase solution, there would be one gate driver for two switches in two locally separated modules (see Figure 47, left). The gate driver is placed in the middle of both switches as it cannot be

simultaneously placed very close to both switches. This results in a high parasitic inductance in the gate driver loop, which creates an oscillating circuit and leads to high ringing and voltage overshoots at the gate of the MOSFETs. Large gate resistors ($R_{g,on} / R_{g,off}$) are needed to damp the oscillating circuit and prevent the destruction of the MOSFETs. Adversely, large gate resistors reduce the switching speed and lead to higher switching losses and lower efficiency.

For the six-phase solution, there would be one gate driver for one switch in one power module (see Figure 47, right), allowing the gate driver to be placed very close to the corresponding switch. This results in a small parasitic inductance in the gate driver loop and an oscillating circuit, but with much smaller ringing and voltage overshoots at the gate of the MOSFETs. To damp the oscillating circuit, only small gate resistors ($R_{g,on} / R_{g,off}$) are needed. These enable higher switching speeds and lead to lower switching losses and higher efficiency, contrary to large gate resistors.

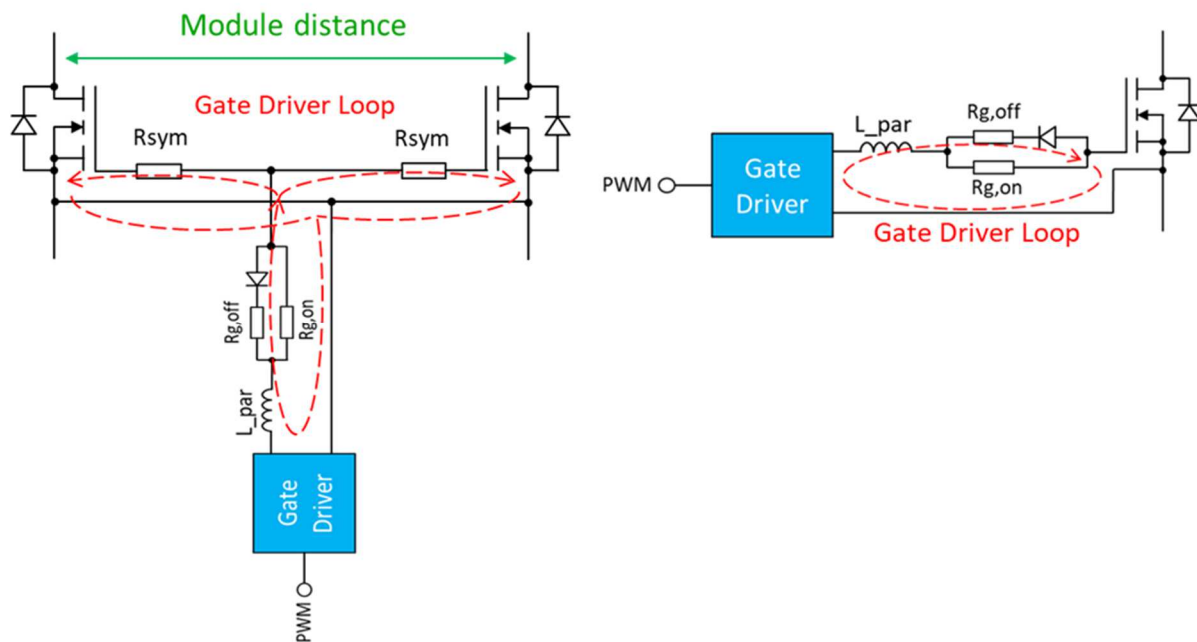


Figure 47. Gate driver loop for three-phase configuration (left) and six-phase configuration (right)

To avoid the parallel connection of two power modules and enable higher efficiency, it was decided to use a six-phase configuration for the motor traction inverters for the secondary machines. This results in a six-phase inverter system with one common DC link capacitor. For the six-phase system, the current and voltage ripple of the DC link and, therefore, the DC link capacitor can be reduced by using multiphase interleaved pulse-width modulated (PWM) techniques with phase displacement as stated in [93] (see also next Chapter 5.4.4). The total number of power semiconductors for the six-phase system remains the same as for the three-phase system. The total inverter losses of both systems are also approximately the same. Another advantage of the six-phase system is that this configuration enables fail-operational capabilities if incorporated in the control algorithm. If one of the two three-phase subsystems of the six-phase motor or the six-phase inverter fails, the other subsystem can still generate at least about half of the maximum output power and thrust for the aircraft. The disadvantage of the six-phase configuration is that the double amount of current sensors and gate driver circuits are needed. However, it also cuts the power requirements for each single gate driver output by half.

5.4.4. DC link capacitor

The DC link capacitor is the second most important part of the inverter system. For the dimensioning of the DC-link capacitor, a capacitor voltage ripple of less than 16 V is normally used. The needed capacitance depends mainly on the maximum allowed voltage ripple, the switching frequency, and the operating point (voltage level, modulation index, phase angle) of the inverter system. For a six-phase system, the current and voltage ripple of the DC link and, therefore, the DC link capacitor can be drastically reduced [93]. The first method is to use multiphase interleaved PWM techniques and shift the carrier signals for the PWM for the second three-phase system by a certain angle. The optimum angle value for the phase shift is 90 degree [93]. The second method is a motor phase displacement for the second three-phase system. The optimum angle value for the phase displacement is 60 degree [93]. However, the difference between a phase displacement of 60 degree compared to a value of 30 degree is small, and for the current motor design, no phase displacement is planned. Nevertheless, it is an optimization parameter that could be utilized in the future.

The required minimum DC link capacitance of a three-phase traction inverter can be estimated as [94]:

$$C_{DC-link,min} \geq \frac{n \cdot I_{out}}{f_{sw}} \cdot \frac{1}{\Delta v_{pp}} \cdot r_{max}(\varphi) \quad (5-17)$$

With n the number of motor phases, I_{out} the output current amplitude, f_{sw} the switching frequency, Δv_{pp} the maximum allowed voltage ripple, and a scaling factor r_{max} , which depends on the output phase angle φ . The relevant values for the scaling factor r_{max} are shown in Table 40.

Table 40. Values for the scaling factor r_{max}

Angle	Value for 3-phase system	Value for 6-phase system
$\varphi = 20^\circ$	$r_{max} = 0.061$	$r_{max} = 0.034$
$\varphi = 45^\circ$	$r_{max} = 0.066$	$r_{max} = 0.025$
$\varphi = 70^\circ$	$r_{max} = 0.071$	$r_{max} = 0.014$

The output phase angle φ lies, depending on the operation point of the motor, somewhat between 25° and 40° . For the dimensioning of the DC link capacitor, a factor of 0.034 for the six-phase system was used. The final calculated DC link capacitance for all operating points is shown in Chapter 5.4.5 and it was calculated with the following equation:

$$C_{DC-link,min} \geq \frac{6 \cdot I_{out,6-phase}}{20 \text{ kHz}} \cdot \frac{1}{16 \text{ V}} \cdot 0.034 \quad (5-18)$$

The maximum ripple current is the second most important parameter for sizing of the DC link capacitor. The ripple current generates losses inside the capacitors, which have to be limited to not exceed the maximum allowed capacitor temperature. The ripple current depends on the output current I_{out} and the operating point of the motor (modulation index). For a 3-phase system, the maximum ripple current can be roughly estimated to be 60 % of the maximum output current I_0 [95]. For a 6-phase system, the maximum ripple current is further reduced by a factor of 0.55 using interleaved PWM techniques [95]. Therefore, the maximum ripple current was calculated to:

$$I_{DC-link,max} = 0.6 \cdot 0.55 \cdot I_{out,6-phase} \quad (5-19)$$

For the DC link capacitor of high-performance traction inverters, mainly foil or ceramic capacitors are used. Electrolyte capacitors are too bulky to fit in the inverter design space and have a too low current ripple rating. Ceramic capacitors have the highest capacitance volume density but are rather expensive. Another drawback is that the capacitances of (most) common ceramic capacitors are dependent on the applied voltage and temperature. Apart from that, they have very low ESL (equivalent series inductance) and ESR (equivalent series resistance) values and a high ripple current capability, making them an ideal choice for DC link applications. The manufacturer TDK designed a special series of ceramic capacitors, called CeraLink™, that are particularly suited for DC link applications. These capacitors are designed to have their maximum capacitance at a voltage bias of 800 V and room temperature.

Foil capacitors have a rather low capacitance volume density but are relatively cheap in comparison to ceramic capacitors. The biggest advantage is that the capacitance of foil capacitors is neither voltage nor temperature-dependent. However, the maximum applied voltage is limited by the capacitor temperature. For example, for a temperature of 105°C, a derating of 70 % for the maximum allowed voltage is necessary. High temperatures also reduce the lifetime of foil capacitors dramatically. Due to higher ESR values, the ripple current capability is a lot smaller than for ceramic capacitors. The ESL values are rather high because most foil capacitors are radial leaded devices.

In the end, it was decided to use a custom-designed foil capacitor for the motor and generator drive inverters because the foil capacitor is more lightweight than a solution with ceramic capacitors. The capacitor solution would be smaller in volume, but the weight advantage should be favoured for an aircraft application. Additionally, the usage of a custom foil capacitor makes it easier to use laminated busbars to connect the DC link capacitor with the power modules.

5.4.5. Design analysis results for the motor and generator inverter systems

The following Table 42 and Table 43 show the results for the simulated power losses with the “SpeedFit Design Simulator” and the calculated DC link parameters for the motor inverters for the secondary electric machines and the generator inverters for the primary electric machines. As explained at the beginning of Chapter 5.4.1, the generator inverter with a nominal power of 1200 kW consists of two motor drive inverters, each having a nominal power of 600 kW. Different SiC power modules were investigated, and the low-inductance half-bridge power module, CAB760M12HM3 from Wolfspeed (see Table 41), was chosen as the best option. The 6-phase motor inverter will consist of six half-bridge power modules, and the two-times 6-phase generator inverters will consist of twelve half-bridge power modules. For both inverter systems, efficiencies greater than 99 percent can be achieved.

Table 41. Characteristics of half-bridge power module CAB760M12HM3 from Wolfspeed

Parameter	Value
Blocking voltage	1200 V
Current rating	765 A
On-resistance $R_{DS(on),25^{\circ}C}$	1.33 mΩ
Turn-on switching energy $E_{on,25^{\circ}C}$	20.3 mJ
Turn-off switching energy $E_{off,25^{\circ}C}$	17.9 mJ
Reference voltage U_{ref} for switching energies	600 V
Reference current I_{ref} for switching energies	760 A

Table 42. Results of technology analysis for secondary electric machine and inverter with 600 kW nominal power for short-term time frame (2025-2035)

		Take off	Climb	Cruise	Data Origin
Secondary propeller	Mission time in min	0.34 / 0.37	21 / 24	12 / 97	from TLAR
	$P_{\text{Propeller}}$ in kW	407	--	--	from TLAR
	$T_{\text{Propeller}}$ in Nm	6900	--	--	from TLAR
	$n_{\text{Propeller}}$ in rpm	563	--	--	calculated
	$\eta_{\text{Propeller}}$ in %	75	--	--	from TLAR
Secondary electric motor	η_{Gearbox} in %	98	--	--	from TLAR
	Gearbox ratio	1:10	--	--	determined
	$P_{\text{Motor,mech}}$ in kW	554	--	--	calculated
	T_{Motor} in Nm	939	--	--	calculated
	n_{Motor} in rpm	5633	--	--	calculated
	η_{Motor} in %	96	--	--	from TLAR
	Motor configuration	6-phase	--	--	determined
Inverter for secondary electric motor	Inverter configuration	6-phase	--	--	determined
	$P_{\text{Inverter,total}}$ in kW	577	--	--	calculated
	$P_{\text{Inverter,3-phase}}$ in kW	288	--	--	calculated
	$I_{\text{LL,eff}} = I_{\text{str,eff}}$ in A_{RMS}	385	--	--	calculated
	V_{DC} in V	800	--	--	determined
	I_{DC} in A_{RMS}	727	--	--	calculated
	f_{PWM} in kHz	20	--	--	determined
	$P_{\text{cond,total}}$ in W	2064	--	--	simulated
	$P_{\text{sw,total}}$ in W	2978	--	--	simulated
	$P_{\text{losses,total}}$ in W	5042	--	--	simulated
	$\eta_{\text{Inverter,total}}$ in %	99.13	--	--	simulated
	T_{j} in °C	135.3	--	--	simulated
	$C_{\text{DC-link,min}}$ in μF	347	--	--	calculated
	$I_{\text{DC-link}}$ in A_{RMS}	127	--	--	calculated

Table 43. Results of technology analysis for primary electric machine and inverter with 1200 kW nominal power for short-term time frame (2025-2035)

		Take off	Climb	Cruise	Data Origin
Primary propeller	Mission time in min	0.34 / 0.37	21 / 24	12 / 97	from TLAR
	$P_{\text{Propeller}}$ in kW	340	1266	1136	from TLAR
	$T_{\text{Propeller}}$ in Nm	5760	12173	7780	from TLAR
	$n_{\text{Propeller}}$ in rpm	564	993	1394	calculated
	$\eta_{\text{Propeller}}$ in %	63	84	85	from TLAR
Primary electric motor	η_{Gearbox} in %	98	98	98	from TLAR
	Gearbox ratio	1:10	1:10	1:10	determined
	$P_{\text{Motor,mech}}$ in kW	1224	233	209	calculated
	T_{Motor} in Nm	2074	224	143	calculated
	n_{Motor} in rpm	5637	9931	13943	calculated
	η_{Motor} in %	96	96	96	from TLAR
	Motor configuration	2x 6-phase	2x 6-phase	2x 6-phase	determined
Inverter for primary electric motor	Inverter configuration	2x 6-phase	2x 6-phase	2x 6-phase	determined
	$P_{\text{Inverter,total}}$ in kW	1175	224	201	calculated
	$P_{\text{Inverter,3-phase}}$ in kW	294	56	50	calculated
	$I_{\text{LL,eff}} = I_{\text{str,eff}}$ in A_{RMS}	392	75	67	calculated
	V_{DC} in V	800	800	800	determined
	I_{DC} in A_{RMS}	1482	281	252	calculated
	f_{PWM} in kHz	20	20	20	determined
	$P_{\text{cond,total}}$ in W	6076	497	437	simulated
	$P_{\text{sw,total}}$ in W	4332	87	74	simulated
	$P_{\text{losses,total}}$ in W	10408	584	511	simulated
	$\eta_{\text{Inverter,total}}$ in %	99.12	99.48	99.49	simulated
	T_{j} in °C	137.7	73.2	72.1	simulated
	$C_{\text{DC-link,min}}$ in μF	644	123	110	calculated
	$I_{\text{DC-link}}$ in A_{RMS}	259	49	44	calculated

To give some idea how a possible 600 kW motor traction inverter for the short-term horizon (2025-2035) could look like, the inverter reference design CRD600DA12E-XM3 from the manufacturer Wolfspeed with SiC power modules and a custom foil capacitor should be mentioned [96]. The key parameters of this inverter system are listed in Table 44. The reference design can meet the requirements for the proposed GENESIS motor traction drive inverter. Two of these inverter systems can be used to drive the generator (primary electric machine).

Table 44. Key parameters of the 6-phase 600 kW inverter from Wolfspeed [96]

Parameter	Value
SiC power modules	6x CAB450M12XM3
DC link capacitance in μF	600
Nominal output power in kW	600
Nominal output current in A_{RMS}	360
External length in mm	267
External width in mm	204
External thickness in mm	157
Total weight in kg	9.7
Volume in liter	8.6
Volumetric power density in kW/liter	70.0
Gravimetric power density in kW/kg	62.9

5.5. Bidirectional battery DC/DC converter

There are several suitable topologies for the bidirectional battery DC/DC converters. The main challenge is to choose the optimal solution for every individual application. The main requirements for the battery DC/DC converter are:

- The maximum output power is 1070 kW
- The battery voltage range is between 950 V and 1170 V
- The HV DC bus voltage is assumed to be constant 800 V
- There is no galvanic isolation needed

The battery voltage is always higher than the HV DC bus voltage. From the battery to the HV DC bus, the converter will work as a buck-converter and from the HV DC bus to the battery as a boost-converter. Due to this limitation, a simple half-bridge converter is the optimal topology. Figure 48 shows the proposed topology. It provides a simple, low-cost and highly efficient solution due to the low number of semiconductors and passive components.

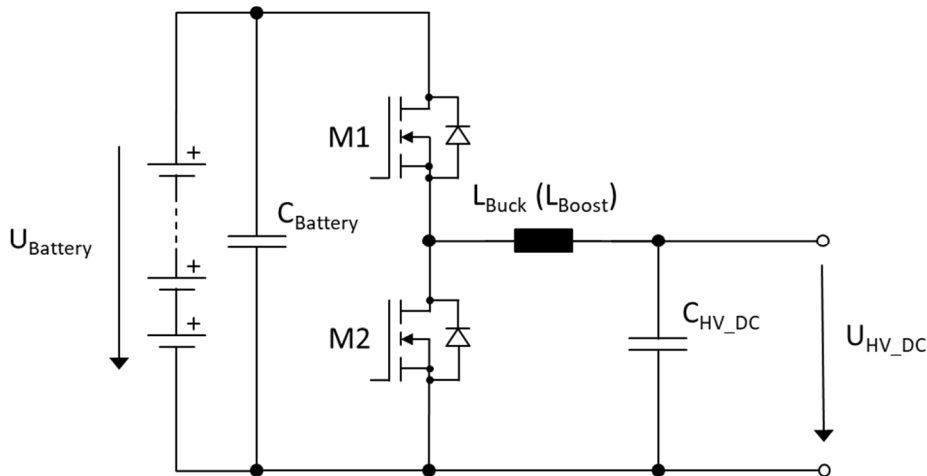


Figure 48. Half-bridge DC/DC converter

Furthermore, it is proposed to use three DC/DC converters in an interleaved configuration (see Figure 49) to decrease the ripple current and, therefore, the losses in the inductors and capacitors. The size of the capacitors can also be reduced by using interleaved technology. Moreover, the number of parallel MOSFETs for a single converter without interleaving would be too high to construct a MOSFET module.

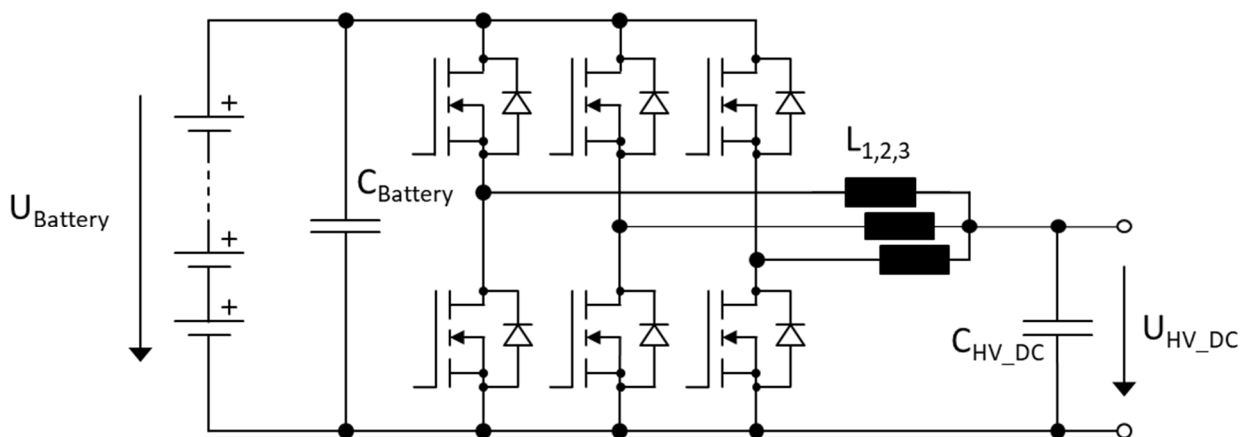


Figure 49. Three times interleaved halfbridge DC/DC converter

The converter will be operated in continuous conduction mode (CCM) for better efficiency. The value of the inductor in a half-bridge converter depends on both possible directions of energy flow. It is necessary to calculate the minimum inductor value for buck (L_{Buck}) and boost operation (L_{Boost}). The minimum value is determined according to the equations below:

$$L_{Buck} > \frac{V_{out} \cdot (V_{in_max} - V_{out})}{K \cdot f \cdot V_{in_max} \cdot I_{out}}$$

$$L_{Boost} > \frac{V_{in_min}^2 \cdot (V_{out} - V_{in_min})}{K \cdot f \cdot I_{out} \cdot V_{out}^2}$$

Where f is the PWM switching frequency, K is the estimated inductor ripple, V_{out} is the output voltage, I_{out} is the output current, V_{in_max} is the maximum input voltage. With an estimated 20 % inductor current ripple per converter, the inductance must be at least 28.37 μ H. The voltage ripple ΔV_{max} is assumed to be less than 1 %. The capacitance and the ESR (equivalent series resistance) of the capacitor determine the voltage ripple. With the duty cycle D , the ESR-ripple for the buck-operation ($\Delta V_{out_ESR_Boost}$) and boost-operation ($\Delta V_{out_ESR_Buck}$) are given by:

$$\Delta V_{out_ESR_Boost} = ESR \cdot \left(\frac{I_{out}}{1-D} + \frac{\frac{K}{3} \cdot I_{out} \cdot V_{out}}{2 \cdot V_{in}} \right)$$

$$\Delta V_{out_ESR_Buck} = ESR \cdot \frac{K}{3} \cdot I_{out}$$

The minimum capacitance for the for the buck-operation (C_{out_Boost}) and boost-operation (C_{out_Buck}) is calculated to:

$$C_{Battery} = C_{out_Boost} = \frac{I_{out} \cdot D}{f \cdot (\Delta V_{max} - \Delta V_{out_ESR_Boost})}$$

$$C_{HV_DC} = C_{out_Buck} = \frac{\frac{K}{3} \cdot I_{out}}{8 \cdot f \cdot (\Delta V_{max} - \Delta V_{out_ESR_Buck})}$$

For an assumed ESR of 1 m Ω , the capacitances are calculated to $C_{out_Boost} = 280.2 \mu$ F and $C_{out_Buck} = 14.09 \mu$ F. A maximum temperature increase of $\Delta T = 60$ K was assumed to calculate the necessary amount of parallel MOSFETs. The losses consist mainly of conduction losses and switching losses. The conduction losses P_{con} per MOSFET can be calculated with the following two equations:

$$P_{con} = R_{DS(on)} \cdot \left(\frac{I_{out}}{n} \right)^2 \cdot D$$

$$P_{con} = R_{DS(on)} \cdot \left(\frac{I_{out}}{n} \right)^2 \cdot (1 - D)$$

Where n is the number of parallel MOSFETs, $R_{DS(on)}$ is the on-resistance of the MOSFETs, and D the worst-case duty cycle of the buck or boost converter. Which one applies depends on the energy flow direction. The switching losses P_{sw} per MOSFET are estimated to:

$$P_{sw} = f \cdot (E_{on} + E_{off}) \cdot \frac{I_{out} \cdot V_{DC}}{I_{ref} \cdot n \cdot V_{ref}}$$

Where f is the PWM switching frequency, E_{on} is the turn-on energy, E_{off} is the turn-off energy, I_{out} is the output current, V_{DC} is the DC link voltage, I_{ref} is the reference current value, n is the number

of parallel MOSFETs, and V_{ref} is the reference voltage value. The equation is simplified. In reality, there is no exact linear correlation between switching energies and current and voltage levels.

One of the main factors that determine the switching losses is the switching frequency. There is a tradeoff between the size of passive components and switching losses. With a high switching frequency, the size of the capacitors and inductors can be reduced, but the switching losses will increase. Due to the early stage of the project, there are no size constraints for the inductor, and therefore, it was necessary to assume a realistic frequency. A switching frequency of 100 kHz offers a reasonable tradeoff between size and losses. To estimate the resulting temperature rise, the losses are multiplied by the thermal resistance. Assuming a small thermal resistance between MOSFET and heat sink, the minimum number of parallel MOSFETs is seven for M1 and six for M2 (see Figure 48). The following Table 45 gives a summary of the MOSFET losses and the resulting temperature increases. Power semiconductors with a minimum breakdown voltage of 1700 V have to be used due to the given maximum battery voltage of 1170 V. Different options were considered and, in the end, the 20 mΩ 1700 V SiC MOSFETs G3R20MT17-CAL from GeneSiC were chosen for the battery DC/DC converter.

Table 45: Summary of MOSFET losses

Operation mode	Switch	P_{sw}	P_{con}	ΔT
Buck-Mode	M1	150.31 W	116.14 W	55.95°C
	M2	175.36 W	59.37 W	49.29°C
Boost-Mode	M1	150.31 W	82.36 W	48.86°C
	M2	175.36 W	42.10 W	45.67°C

The theoretical calculated efficiency of the DC/DC converter is 99.69 % for buck operation and 99.72 % for boost operation. For the calculation, neither the inductor nor the capacitor losses were included. The actual reachable efficiency, in a realistic application, should be about 98 % to 99 %. Using zero voltage switching to decrease switching losses might result in higher efficiency. This would require further investigation. Depending of the size of the inductors and capacitors, high sophisticated designs of the battery DC/DC converter should be enable to reach a power density of about 40 to 60 kW/kg.

5.6. Unidirectional fuel cell DC/DC converter

There is no fuel cell system planned as an energy source for the short-term time frame (2025-2035). Therefore, there is also no unidirectional fuel cell DC/DC converter required. However, the basic topology for such a converter would be a multiple times interleaved boost-converter. Therefore, the same topology and design rules from Chapter 5.5 can be used.

5.7. DC/AC grid converter

The DC/AC grid converter has the basic topology of a two-level inverter, as described in Chapter 5.4 (see Figure 50). Therefore, the same design rules from Chapter 5.4 apply to calculate the inverter losses and to size the DC link capacitor. The only difference is that filter inductors have to be connected between the DC/AC grid converter and the 400 Hz 115 V power net to reduce the output current ripple. Depending on the requirements of the 400 Hz power net (harmonics current limits), it could also be necessary to increase the filter effort and to install a three-phase LC-filter or LCL-filter instead of only three inductors. The topic of electromagnetic compatibility (EMC) and net filters is rather complex and needs extensive analysis and is not part of this report. However, a rough estimation of the filter inductance value is given here. The inductance value L_{filter} can be approximated to [97]:

$$L_{filter} \cong \frac{V_{DC} \cdot m}{2 \cdot \sqrt{3} \cdot f_{PWM} \cdot \Delta i_{max}} = \frac{800 V \cdot 0.144}{2 \cdot \sqrt{3} \cdot 16 kHz \cdot 5 A} = 416 \mu H$$

With V_{DC} the DC bus voltage, m the modulation index, f_{PWM} the PWM switching frequency and Δi_{max} the maximum allowed current ripple value. If required, a LCL-filter can, for example, be sized according to [98]. Table 46 shows the analysis results for the DC/AC grid inverter. The power semiconductor losses have been simulated with the “SpeedFit Design Simulator” from Wolfspeed. For the power semiconductors, the Wolfspeed power module CAB425M12XM3 was chosen. Sophisticated designs of DC/AC grid converters can reach a power density of at least 30 kW/kg.

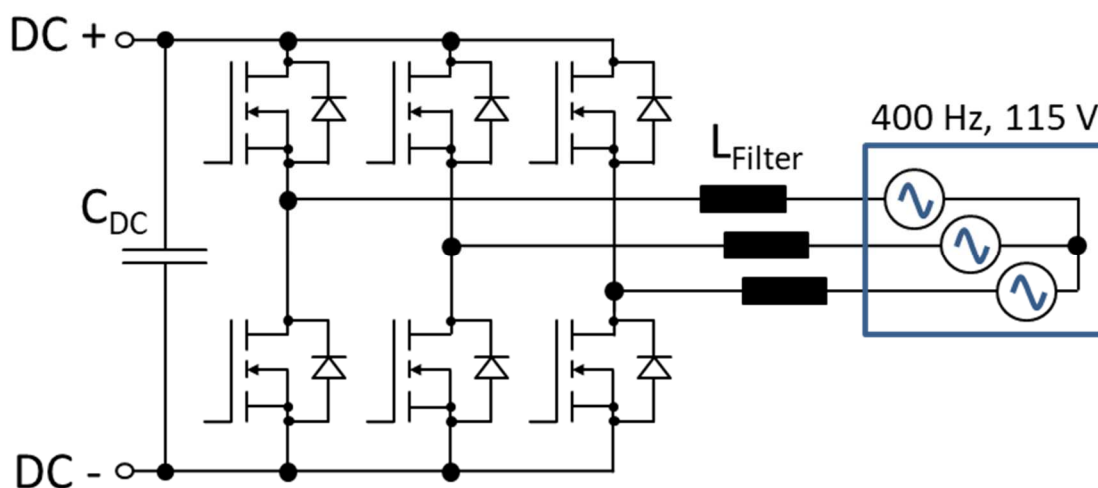


Figure 50. DC/AC grid converter

Table 46. Results of technology analysis for the DC/AC grid inverter

Parameter	Value	Data Origin
Inverter configuration	3-phase	determined
$P_{\text{Inverter,total}}$ in kW	30	from TLAR
I_{DC} in A_{RMS}	37.5	calculated
V_{DC} in V	800	determined
$V_{\text{out,LL}}$ in V_{RMS}	115	from TLAR
f_{out} in Hz	400	from TLAR
f_{PWM} in kHz	16	determined
$I_{\text{LL,eff}} = I_{\text{str,eff}}$ in A_{RMS}	150.6	calculated
$P_{\text{cond,total}}$ in W	244.5	simulated
$P_{\text{sw,total}}$ in W	240.5	simulated
$P_{\text{losses,total}}$ in W	485.0	simulated
$\eta_{\text{Inverter,total}}$ in %	98.40	simulated
T_j in °C	84.2	simulated
$C_{\text{DC-link,min}}$ in μF	60.0	calculated
$I_{\text{DC-link}}$ in A_{RMS}	90.4	calculated

5.8. Isolating DC/DC converter for low voltage supply

The isolating DC/DC converter for low voltage supply transfers power from the 800 V DC bus to the 28 V consumers of the aircraft. The total 28 V power demand or power demand per converter can differ for various regional aircraft. Table 47 shows two examples. The difference can be explained by the electric consumers inside the aircraft. The Bombardier CRJ100 has many more electric consumers, which run on the 400 Hz power net, than the Embraer ERJ145. Therefore, the Bombardier CRJ100 has a higher power demand regarding the 400 Hz power net. The Embraer ERJ145, by contrast, has a higher power demand regarding the 28 V power net. For this case study, a maximum output current of 400 A and a maximum output power of 11.2 kW for the isolating DC/DC converters were assumed.

Table 47. Examples for 28V power demand for two regional aircraft

Regional aircraft	Number of units	Rated Voltage	Maximum Current	Maximum Power
Embraer ERJ145	5	28 V	400 A	11.2 kW
Bombardier CRJ100	5	28 V	100 A	2.8 kW

For the isolation between the high voltage and low voltage sides, a transformer is necessary. The transformer adds a significant amount of weight, decreases the system efficiency, and increases the system complexity. The isolating DC/DC converter for low voltage supply is the most challenging converter to design compared to the other presented power electronics converters. There are non-resonant, partial-resonant and resonant topologies. Fifteen different implementation possibilities of isolating DC/DC converters are described in [99].

For the given application, a LLC resonant converter or a phase-shifted full bridge (PSFB) converter are the two most promising candidates. The two topologies are shown in Figure 51 and Figure 52. They have the same number of power semiconductors, and both can use the same output stage (e.g., full bridge rectifier) on the low-voltage side. For higher efficiency, the diodes in the output stage are replaced by low-voltage silicon MOSFETs or, for very high switching frequencies, by low-voltage GaN-MOSFETs. The main difference between the two topologies is the control strategy. The output voltage of the LLC converter is controlled by changing the switching frequency, while the one of the PSFB converter is controlled by a phase shift of the PWM signals for the second half-bridge. Both topologies have distinct advantages and disadvantages. A short comparison of the properties is presented in Table 48 and more details can be found in [99] or [100].

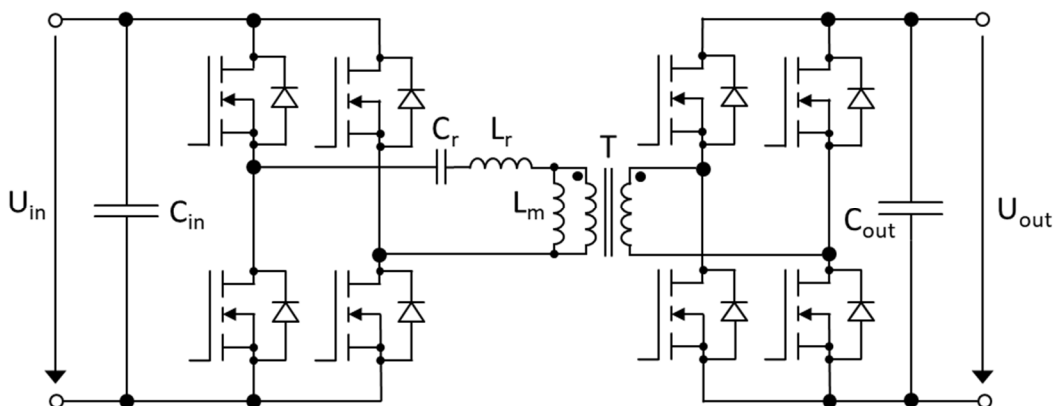


Figure 51. LLC resonant converter

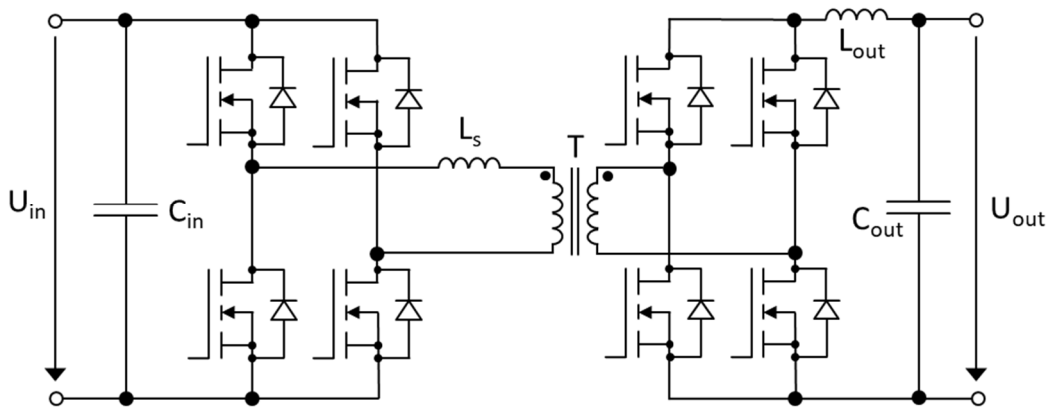


Figure 52. Phase-shifted full-bridge (PSFB) converter

Table 48. Comparison between LLC and PSFB converter [100]

Parameter	LLC converter	PSFB converter
Switching frequency	variable	fixed
Synchronization, current share	poor	good
Output voltage range	medium	wide
EMI	low level of noise generation	medium level of noise generation
Efficiency	good, best at resonance	good, minimizes body diode conduction
Transformer	operates over a wider frequency range	fixed frequency range

An isolated 10 kW HV/LV DC/DC converter is presented, which serves as a reference design for this converter class for the short-term period (2025-2035). Fraunhofer IISB developed the converter for the LuFo V-3 project “GETpower 2”, which is (partially) funded by the German federal ministry BMWi. The main parameters of the converter are listed in Table 49. Regarding the power density, the developed reference design has a 2.5-times higher gravimetric power density than comparable state-of-the-art converters and a 2.3-timer higher volumetric power density. The basic structure of the converter is shown in Figure 53. The converter is split into two identical building blocks. The HV input stage is connected in series to consider the breakdown voltage derating, which must be applied due to cosmic radiation and high altitudes. For the high voltage input stage, 1000V SiC MOSFETs are used. The LV output stage is connected in parallel to increase the output current rating. The topology of the converter is a LLC resonant converter with a full-bridge rectifier output stage. In the output stage, silicon 100 V MOSFETs are used instead of diodes to increase efficiency. The mechanical design is shown in Figure 54.

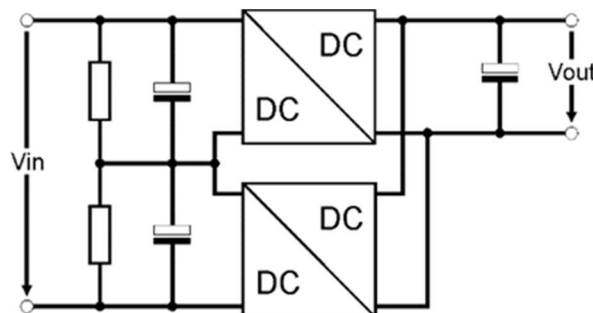


Figure 53. Basis structure of the 10 kW isolating DC/DC converter for low voltage supply

Table 49. Key parameters of the 10 kW isolating DC/DC converter for low voltage supply

Parameter	Value	Unit
Input voltage range	540...840	V
Output voltage range	24...28	V
Maximum output current	400	A
Nominal output current	360	A
Maximum output power	11.2	kW
Nominal output power	10.0	kW
Volume	4	dm ³
Weight	5	kg
Volumetric power density	2.5	kW/dm ³
Gravimetric power density	2	kW/kg
Switching frequency	120...240	kHz
Efficiency	94...97	%

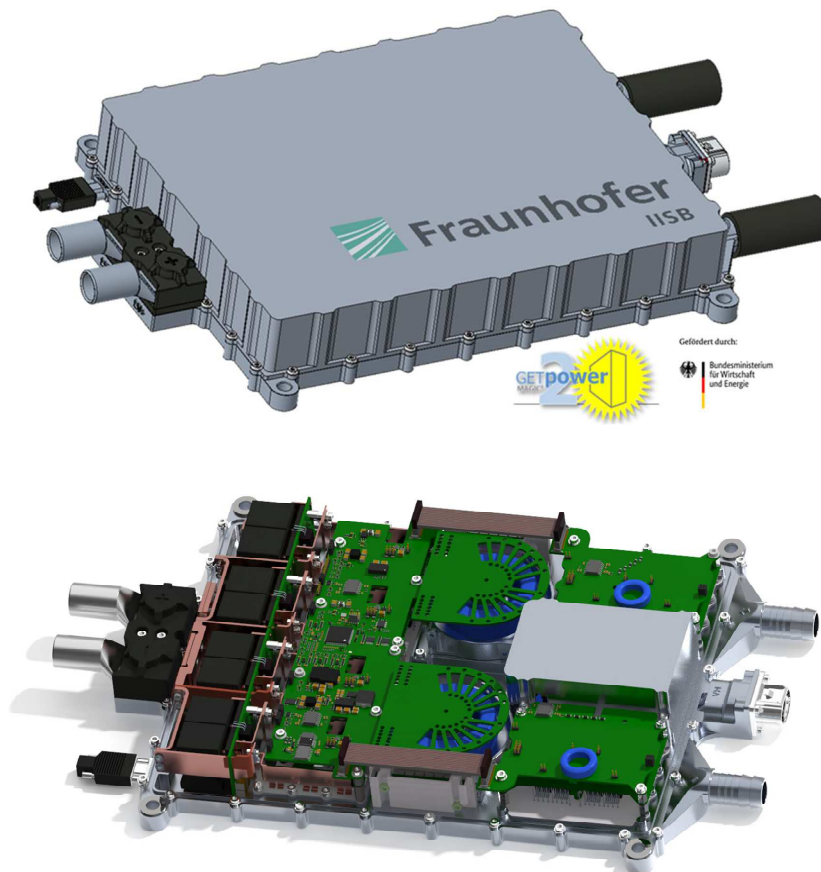


Figure 54. Mechanical design of the 10 kW isolating DC/DC converter for low voltage supply with housing (top) and without housing (bottom)

5.9. Conclusions

The technology analysis for all power electronics converters in the GENESIS project for the short-term horizon (2025-2035) has been presented. The influence of the HV DC bus voltage was investigated. It was concluded that the bus voltage should be set to 800 V for the short-term perspective. Power semiconductors have the biggest influence on the design of power electronics systems. The properties of silicon, silicon carbide, and gallium nitride power semiconductors have been compared. The analysis showed that for the short-term analysis, silicon carbide power semiconductors (SiC MOSFETs) are the best option for all power electronics converters. All different power electronics converters, i.e, motor traction drive inverter, generator traction drive inverter, bidirectional battery DC/DC converter, unidirectional fuel cell DC/DC converter, DC/AC grid converter, and isolating DC/DC converter for low voltage supply, have been investigated in detail. The converters were sized for the application and efficiency and power density values have been provided. The results of the investigation are summarized in Table 50.

Table 50. Results of the technology analysis for all power electronics converters for the short-term horizon (2025-2035)

Converter	Topology	Rated power	Efficiency	Power density
Motor drive inverter	6-phase two-level inverter	600 kW	99 %	63 kW/kg
Generator drive inverter	2x 6-phase two-level inverter	1200 kW	99 %	63 kW/kg
Battery DC/DC converter	3-times interleaved half-bridge converter	1070 kW	98 - 99 %	40 - 60 kW/kg
Fuel cell DC/DC converter	--	--	--	--
DC/AC grid inverter	3-phase two-level inverter	30 kW	98.4 %	30 - 40 kW/kg
Isolating DC/DC converter	2x LLC converter	11.2 kW	94 - 97 %	2 kW/kg

6. Electric drive technology analysis

6.1. Introduction

This chapter deals with the short-term (2025-2035) technology analysis for the electric drives in the GENESIS project. For the propulsion of electric vehicles, electrical AC machines are used. There are six different kinds of radial AC machines (see Figure 55), which all have different kinds of characteristics, advantages, and disadvantages. The main difference between the six AC machines is the configuration of the rotor. With the exception of the switched reluctance motor, they all have a distributed stator winding system. With distributed windings, higher harmonics are reduced or eliminated and the induced back electromotive force (BEMF) voltage becomes (more) sinusoidal. AC motors can be divided into synchronous motors and induction motors.

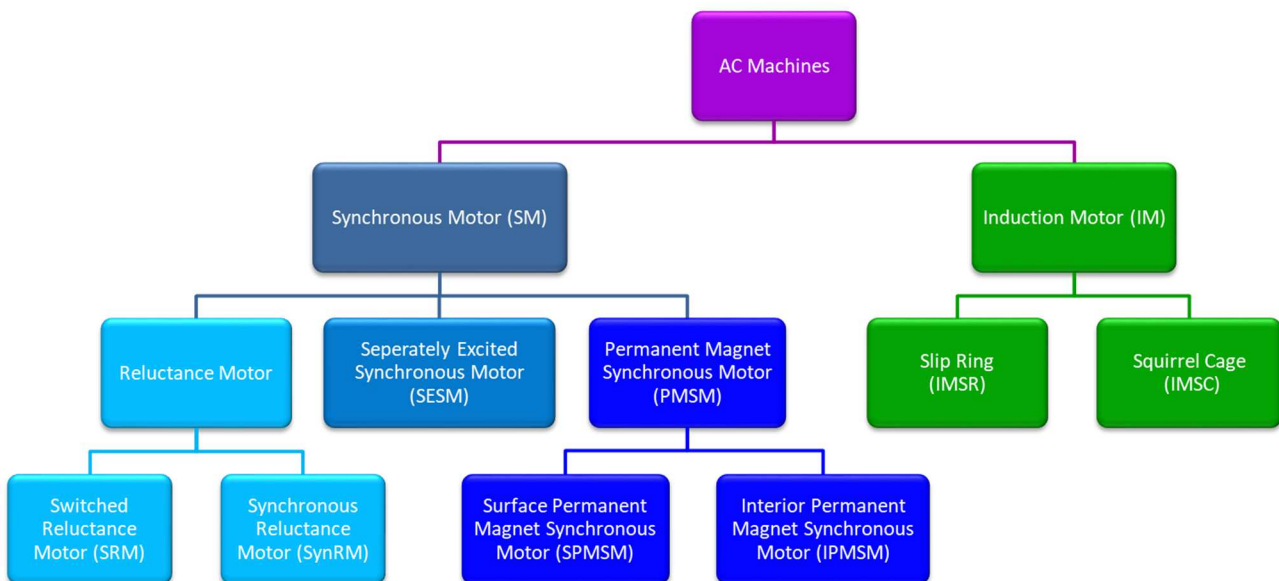


Figure 55. Overview of radial AC machines

For a synchronous motor, the rotor frequency is equal to the rotating frequency of the magnetic field in the stator. For an inductor motor, the rotor frequency is higher (generator mode) or lower (motor mode) as the rotating frequency of the magnetic field in the stator. There are two types of induction motors (IM), the squirrel cage and the slip ring induction motors. The squirrel cage induction motor (IMSC) has rotor bars inside the rotor, which are short-circuited at both ends of the motor. The slip ring induction motor (IMSR) has a winding system inside the rotor. The rotor windings are connected through slip rings to external resistors. By adjusting the resistors, it is possible to influence the speed/torque characteristic of the motor. Induction motors have a good high-speed capability, and they are rather cheap, but they suffer from reduced motor efficiency and power density.

There are three kinds of synchronous motors, the reluctance motors, the permanent magnet synchronous motors, and the separately excited synchronous motors. The reluctance motor has a specially formed rotor, which is only built with electrical steel. No permanent magnets or windings are present inside the rotor, thus reducing the motor's cost and complexity. The disadvantages are the low power density and the high torque ripple. The synchronous reluctance motor (SynRM) has a distributed winding system inside the stator, supplied with sinusoidal currents. The switched reluctance motor (SRM) has distributed windings inside the stator, and the single coils have to be supplied in the right order depending on the rotor position. The separately excited synchronous motor (SESM) has concentrated windings inside the rotor to produce the rotor magnetic field. A slip ring is necessary to supply the rotor windings. This increases the maintenance effort and reduces the power

density. The advantage is that, with an adjustment of the rotor field, the speed/torque characteristic of the motor can be influenced. Another advantage is that no permanent magnets, produced with rare earth elements, are needed, thus leading to lower costs. The most common motor in electrified vehicles is the permanent magnet synchronous machine (PMSM). The magnets inside the rotor can be attached to the surface of the rotor (surface permanent magnets synchronous motor = SPMSM), or they can be inserted inside the rotor core close to its outer surface (interior permanent magnets synchronous motor = IPMSM). The disadvantage of this kind of motor is that permanent magnets are needed, thus, leading to higher costs. The main advantages are the high power density and the high efficiency. A qualitative comparison between different AC machines types is shown in Table 51.

Table 51. Comparison of different AC machine types [101]

Parameter	SRM	SynRM	SESM	SPMSM, IPMSM	IMSR	IMSC
Efficiency base speed	-	+	+	++	O	+
Efficiency field-weakening	+	O	+	+	+	++
High-speed capability	++	-	-	+	-	++
Torque density	-	+	+	++	O	O
Power density	++	+	+	++	O	O
Control effort	--	O	--	-	-	+
Maintenance effort	+	+	--	+	--	+
Power factor	--	O	++	++	+	+
Cost	++	+	-	--	-	O
Noise	--	+	++	++	++	++
Torque ripple	--	+	++	++	++	++

Evaluation scheme: ++ = very good, + = good, O = neutral, - = bad, -- = very bad

For a hybrid or all-electric aircraft application, the motor efficiency and the power density to keep the weight of the motor as small as possible, are more important than the cost. If the motor efficiency is increased, then the battery size can be reduced, allowing weight savings. Considering the crucial role that weight plays, it can be concluded that permanent magnet synchronous machines (PMSM) are the most suitable option for the electric drives in the GENESIS project for the short-term horizon (2025-2035). For the medium-term and long-term horizon, hydrogen will be stored on the plane. With liquid hydrogen the usage of partially (i.e., only with a superconducting rotor) or fully superconducting separately excited synchronous motor machines is possible. This option will be investigated in the following deliverable D2.2.

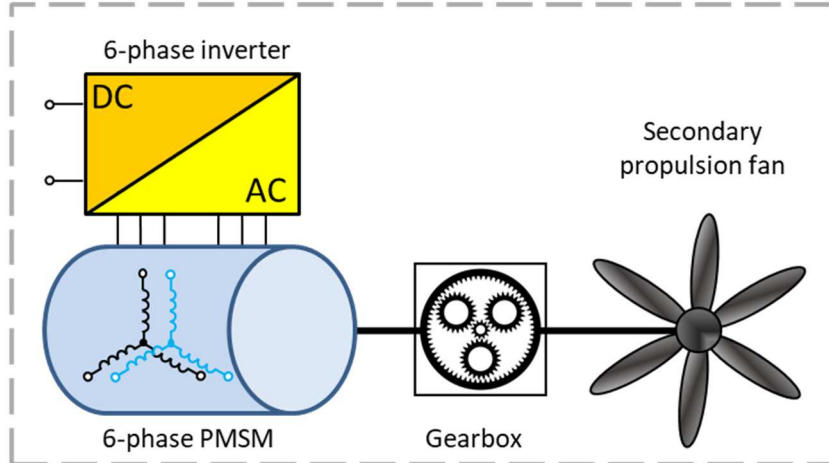
6.2. Configuration of primary and secondary drive train components

Table 52 shows the power demand of the electric machines for different time periods. The secondary electric machines always have half of the power demand of the primary electric machines. Therefore, it is suggested to reuse the components of the secondary electric machines in the primary machines. For the primary machines, two secondary machines are stacked together and connected with a common rotor shaft. This principle is not new. For example, the motor manufacturers EMRAX and MagniX recommend this variant to double the motor power and torque. Figure 56 shows how such a configuration would, in principle, look like. Not only the secondary motors but also the motor drive inverters for the secondary machines can be reused. Two motor drive inverters will be used in combination as the generator drive inverter for the primary motors. As described in Chapter 5.4, multi-phase motors and inverters will be used to enable fail-operational capabilities and limit the current demand for single parts. The secondary machine will be a six-phase machine, which will be driven by a six-phase motor drive inverter. The primary machine will be two stacked six-phase machines, each driven by two six-phase motor inverters.

Table 52. Power demand of electric machines for different time frames

Motor	Number of units	Reference Power in kW		
		Short-Term Year 2025-2035	Medium-Term Year 2035-2045	Long-Term Year 2045-2055
Primary electric machine	2	1200	1200	1500
Secondary electric machine	8	600	600	750

Secondary electric drivetrain



Reuse of components

Primary electric drivetrain

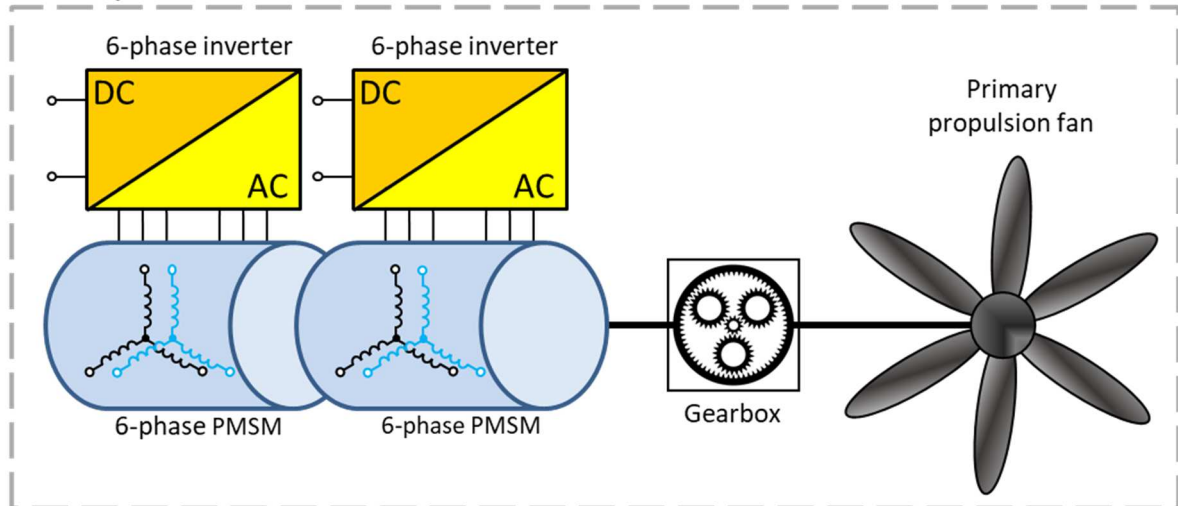


Figure 56. Reuse of secondary electric drive train components to build up the primary electric drive train

6.3. Design analysis results for the electric drive train

A six-phase 600 kW liquid-cooled PMSM motor was designed to meet the requirements for the secondary electric machine. The design of an electric machine depends on many different parameters like stator current density, magnetic field density, pole pair number, number of slots, rotor diameter, rotor length, and the stator geometry defined by yoke thickness, teeth height, and teeth width [85]. The power density of an electric machine is given by [85]:

$$\frac{P}{m} = k_{geometry} \cdot B_g \cdot A \cdot n_{rot} \cdot \eta_{EM}$$

Where P is the electrical motor power, m is the motor mass, B_g is the magnetic field density in the air gap, A is the stator current density, n_{rot} is the motor speed and η_{EM} is the motor efficiency. The geometry parameters $k_{geometry}$ include, e.g., the geometrical details of the teeth (e.g., width and height) and of the rotor, the winding geometry, etc.

The power density is directly proportional to the magnetic field density in the air gap B_g . Therefore, neodymium iron boron (NdFeB) magnets were chosen. They are expensive, but this material has the highest magnetic flux density and thus enables the highest power density. The power density also increases with the stator current density A , which is limited by the cooling of the stator. For a water-jacked cooled motor, a typical value of 10 A/mm² is possible. With direct liquid-cooled windings, a value of 25 A/mm² can be reached. For superconducting machines, the current density can even be greater than 500 A/mm². However, the ohmic losses of the stator windings will also increase with higher current density leading to reduced efficiency. For the current motor design, presented at the end of the chapter, a conventional water-jacked cooled motor was chosen to have a baseline for future investigations. It will be interesting to develop a motor design with directly cooled stator windings in the future and compare it with the current design. The motor power density also increases with the rotational speed n_{rot} . For the GENESIS project in general, the rotational speed of the electric machines can be set by choosing the gearbox transmission ratio. A direct drive of the propulsion fans is not possible. The gearbox ratio was chosen to 1:10 to limit the motor speed to 14,000 rpm during the “Cruise phase”. This is a common value for machines for electric powertrains. The mechanical parameters of the primary and secondary drivetrain are listed in Table 53 and Table 54. A high rotational speed positively influences the motor power density, but it negatively affects the AC motor losses. Moreover, a higher PWM switching frequency is necessary but this will lead to higher inverter losses. Overall, it can be said that if the rotational speed is increased too much, the motor efficiency will suffer.

Table 55 shows the design results for the secondary electric machine during “Take off” for the short-term period (2025-2035). This is the most crucial operating point, as it has the highest output power demand. The motor efficiency was estimated to be about 96 %. The power density for active parts is about 10.6 kW/kg. With a total motor weight of 86.5 kg, the total power density is calculated to 6.4 kW/kg. This lies above the state-of-the-art power densities, which are between 2 and 5 kW/kg. To increase the copper fill factor and power density, a hairpin winding (rectangular winding) was chosen, achieving a copper fill factor of about 0.60.

Table 53. Mechanical parameters for the secondary drive train for the short-term period (2025-2035)

	Use Case	Take off	Climb	Cruise	Data Origin
Secondary propeller	Mission time in min	0.34 / 0.37	21 / 24	12 / 97	from TLAR
	$P_{\text{Propeller}}$ in kW	407	--	--	from TLAR
	$T_{\text{Propeller}}$ in Nm	6900	--	--	from TLAR
	$n_{\text{Propeller}}$ in rpm	563	--	--	calculated
	$\eta_{\text{Propeller}}$ in %	75	--	--	from TLAR
Secondary electric motor	η_{Gearbox} in %	98	--	--	from TLAR
	Gearbox ratio	1:10	--	--	determined
	$P_{\text{Motor,mech}}$ in kW	554	--	--	calculated
	T_{Motor} in Nm	939	--	--	calculated
	n_{Motor} in rpm	5633	--	--	calculated

Table 54. Mechanical parameters for the primary drive train for the short-term period (2025-2035)

	Use Case	Take off	Climb	Cruise	Data Origin
Primary propeller	Mission time in min	0.34 / 0.37	21 / 24	12 / 97	from TLAR
	$P_{\text{Propeller}}$ in kW	340	1266	1136	from TLAR
	$T_{\text{Propeller}}$ in Nm	5760	12173	7780	from TLAR
	$n_{\text{Propeller}}$ in rpm	564	993	1394	calculated
	$\eta_{\text{Propeller}}$ in %	63	84	85	from TLAR
Primary electric motor	η_{Gearbox} in %	98	98	98	from TLAR
	Gearbox ratio	1:10	1:10	1:10	determined
	$P_{\text{Motor,mech}}$ in kW	1224	233	209	calculated
	T_{Motor} in Nm	2074	224	143	calculated
	n_{Motor} in rpm	5637	9931	13943	calculated

Table 55. Results of technology analysis for 6-phase secondary electric machine for the operating point “Take off” for the short-term period (2025-2035)

Parameter	Value	Unit
DC link voltage	800	V
Nominal phase current 3-phase	770	A _{RMS}
Nominal phase current 6-phase	385	A _{RMS}
Nominal power	554	kW
Nominal torque	993	Nm
Nominal speed	5633	rpm
Maximum speed	15000	rpm
Estimated efficiency	96	%
Effective length	180	mm
Total length	215	mm
Stator outer diameter / inner diameter	265 / 217	mm
Rotor inner diameter	80	mm
Air gap	1	mm
Number of Poles / Slots	16 / 96	--
Number of windings per phase	2	/
Wire cross section	2.91 x 2.3	mm
Magnet dimensions	15.5 X 5.0	mm
Magnet material	G48UH	
Stator material	M270-35A	
Rotor material	M270-35A HS	
Magnet weight	3.4	kg
Windings weight	5.6	kg
Stator weight	20.2	kg
Rotor weight	23.1	kg
Active parts weight	52.3	kg
Rotor shaft weight	12.4	kg
Housing weight	18.8	kg
Miscellaneous weight	3.0	kg
Total weight	86.5	kg
Power density for active parts	10.6	kW/kg
Total power density	6.4	kW/kg

Figure 57 shows the winding scheme of the secondary electric machine. In Figure 58, the final design of the active parts of the secondary electric motor is shown, and a closer look at the orientation of the permanent magnets inside the rotor is presented (left). This magnet configuration helps to increase the motor torque. Figure 59 shows the mechanical motor design with the water-cooled housing, bearings, and rotor shaft. In Figure 60, the mechanical design of the primary electric machine, as a stacked version of two secondary electric machines, is shown.

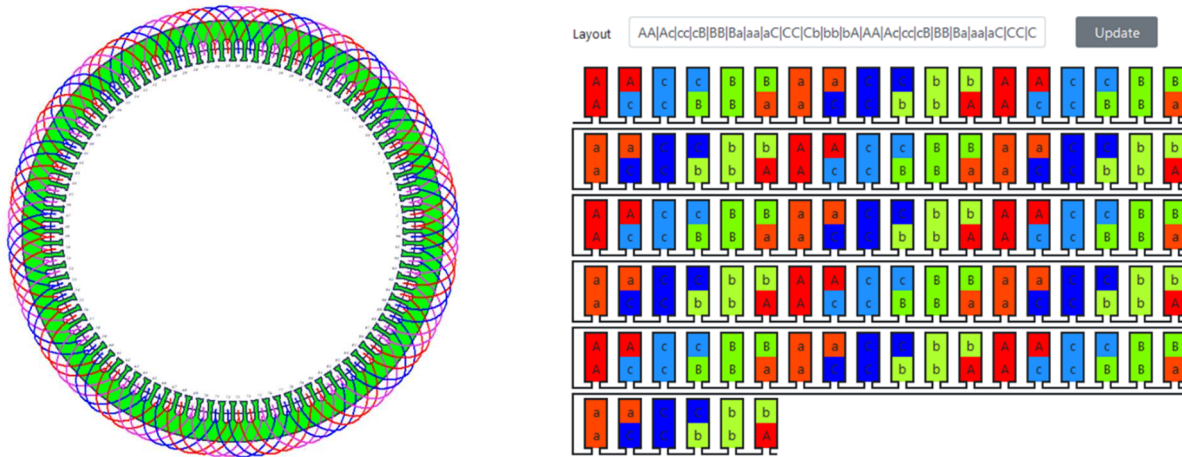


Figure 57. Winding scheme of the secondary electric machine

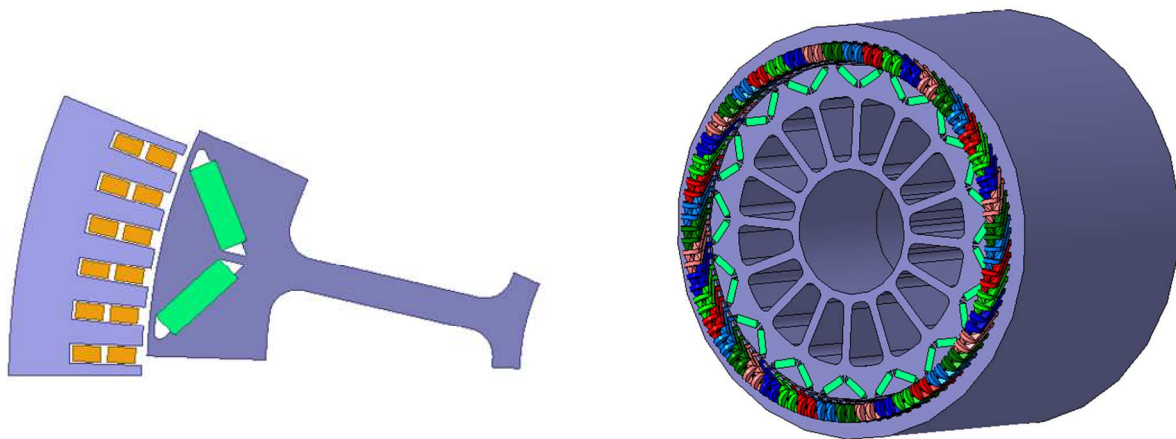


Figure 58. Orientation of the permanent magnets inside the rotor (left) and mechanical design of the secondary electric machine without housing (right)

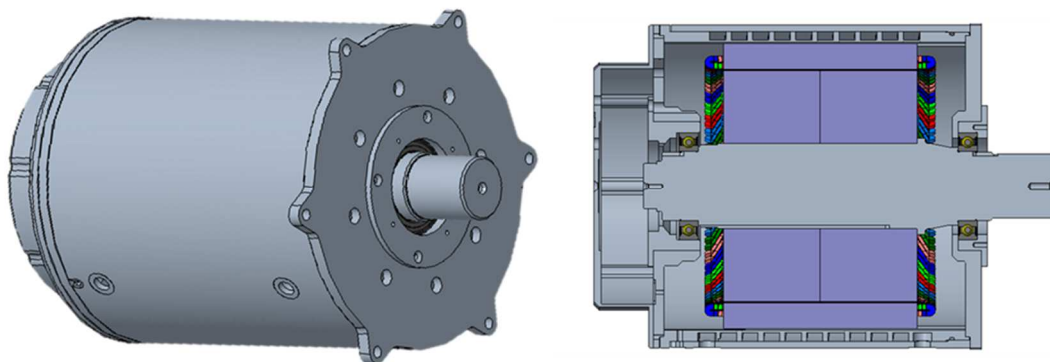


Figure 59. Mechanical design of the secondary electric machine with housing and rotor shaft

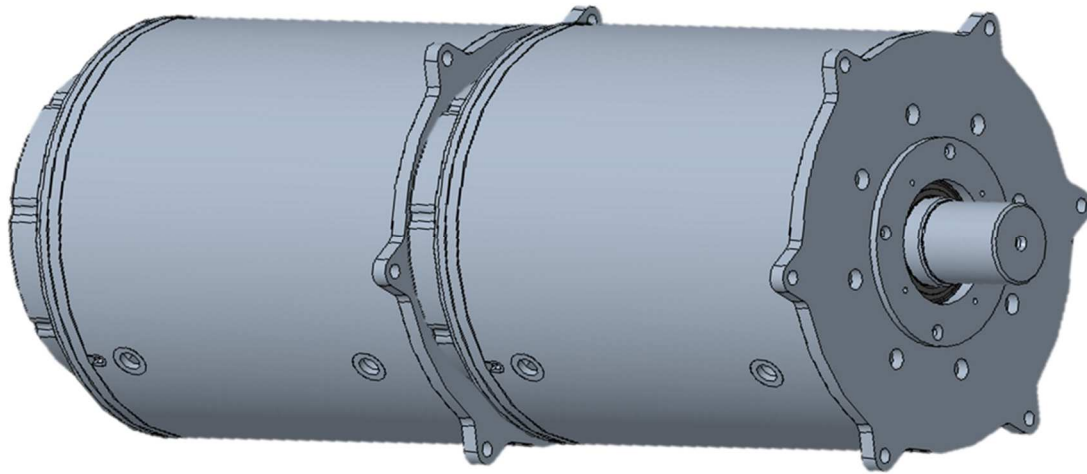


Figure 60. Mechanical design of the primary electric machine as a stacked version of two secondary electric machines

The presented motor design is a state-of-the-art design, which is used in many battery electric vehicles today. With the needed time for qualification and series production build-up, a market entry in 2025 seems realistic. The two topics Halbach array and direct-cooled copper windings will be further investigated in the project to improve motor efficiency and power density. With a Halbach magnet array, a more sinusoidal magnetic field in the air gap can be achieved compared to a traditional PMSM. The magnet field density in the air gap is increased, and the iron losses are decreased. With direct-cooled copper windings, the current density and, therefore, the power density can be increased. A higher current density can lead to higher ohmic losses and, therefore, reduced motor efficiency. Hence, a sophisticated investigation is necessary. The primary electric machine can also be further optimized if a new motor housing is designed, which will enclose the active parts of two secondary machines.

7. On-ground energy supply technology analysis

7.1. Introduction

The on-ground energy supply technology analysis focuses on analyzing appropriate energy supply technologies for on-ground energy storage, grid connection, and energy transfer to aircraft. It is planned that the involvement of a regional airport in GENESIS, via subcontracting, provides specific data and modelling experience for the energy supply systems covering different technological streams, incl. hydrogen supply and local electricity grid systems. However, the initiation of the subcontract has been delayed in the project, compelling this deliverable to be limited in its addressing the on-ground energy supply technology analysis in a short-term perspective (this will be adjusted in the next deliverable D.2.2).

Therefore, the present chapter only presents general technology considerations for the electric on-ground energy supply and DC fast-charging stations. A basic overview is given, and different possibilities for grid technologies and charging stations are discussed. The concepts can be further evaluated and concretized when the information exchange with the subcontracted airport is started. Open questions, which have to be answered among other things, are the total energy demand, connection to the electrical grid, number of hybrid/electric aircraft that have to be charged, maximum available charging time, possibilities to install local photovoltaic systems and energy storage units. Only then can a charging profile for the aircraft batteries be evaluated, and the peak power demand can be assessed. If the peak power demand is too high and cannot be covered with local energy storage units, the possibility of swapping batteries has to be investigated in detail.

For the medium-term time frame (2035-2045), the aircraft will use a fuel-cell system, and therefore the on-ground hydrogen storage and supply will play an important role. This topic will be investigated and presented in the following deliverable D2.2, regarding the medium-term technology analysis for all major technologies.

7.2. Basic technologies for electric on-ground energy supply

The electrification of aircraft comes with immense stress to the electrical system of the airport due to the vastly increased power demand for charging airplanes. A mid-to-long-term infrastructure should aim to improve the airports' entire energy system, including IT and control systems, lighting, and general-use low voltage supply. The cost/benefit potential of sector-coupling should also be evaluated. Instead of overhauling the existing system as a whole, the short-term analysis will focus on an electrical grid with the sole purpose of charging electric vehicles on the airfield.

As such, the components that make up the infrastructure are limited to the following:

- Charger for aircraft
- Charger for airfield support vehicles
- Connection to the main grid
- Local photovoltaic supply
- Local battery storage

Even with local supply and storage, the grid feed-in, for an infrastructure capable of charging multiple aircraft and other airfield support vehicles, will need to be connected to the medium-voltage grid (6 kV to 60 kV) due to the high power demand. The distribution network on the airport premises should then be realized on a low-voltage level ($< 1000 V_{AC}$ or $< 1500 V_{DC}$ according to the low voltage directive 2014/35/EU) due to safety reasons.

The first concept is utilizing a common AC bus for the distribution system [102], depicted in Figure 61. A standard low-frequency transformer is used to connect to the medium-voltage grid and the entire distribution network. It is a standard electrical installation as it is common in most of the world.

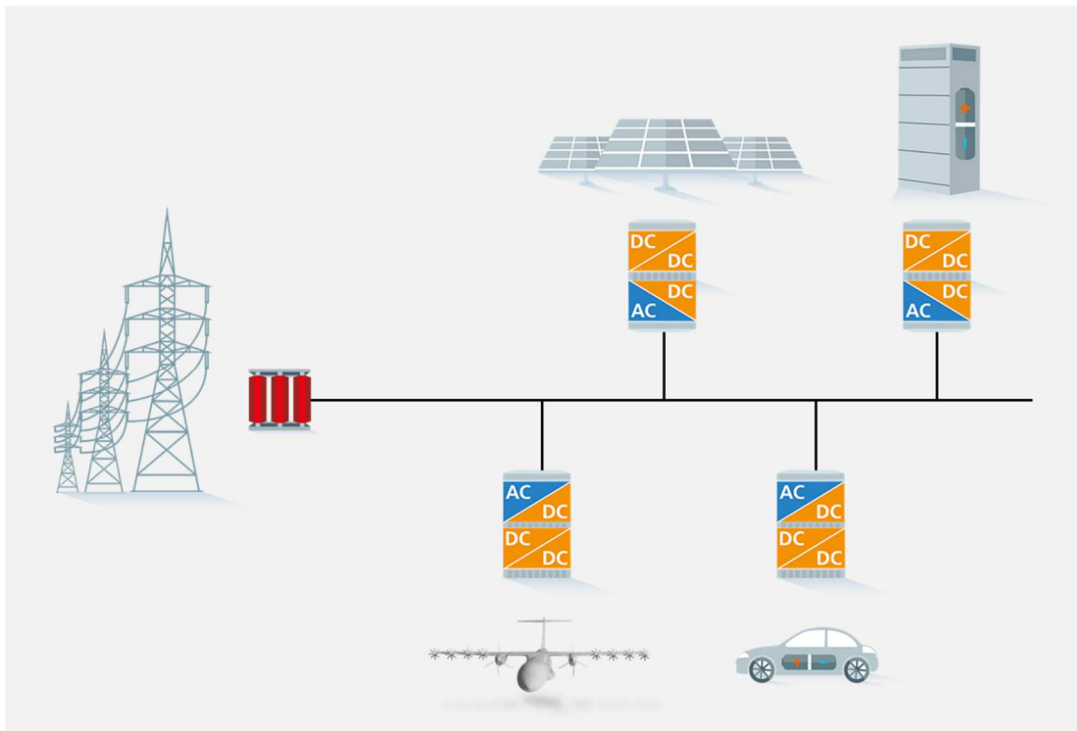


Figure 61. Basic principle of an AC based grid

Photovoltaic generation and stationary battery storage, as well as mobile batteries in aircraft and support vehicles, are inherently DC-based. As such, the second concept links all components with a low-voltage DC grid instead, shown in Figure 62 [102].

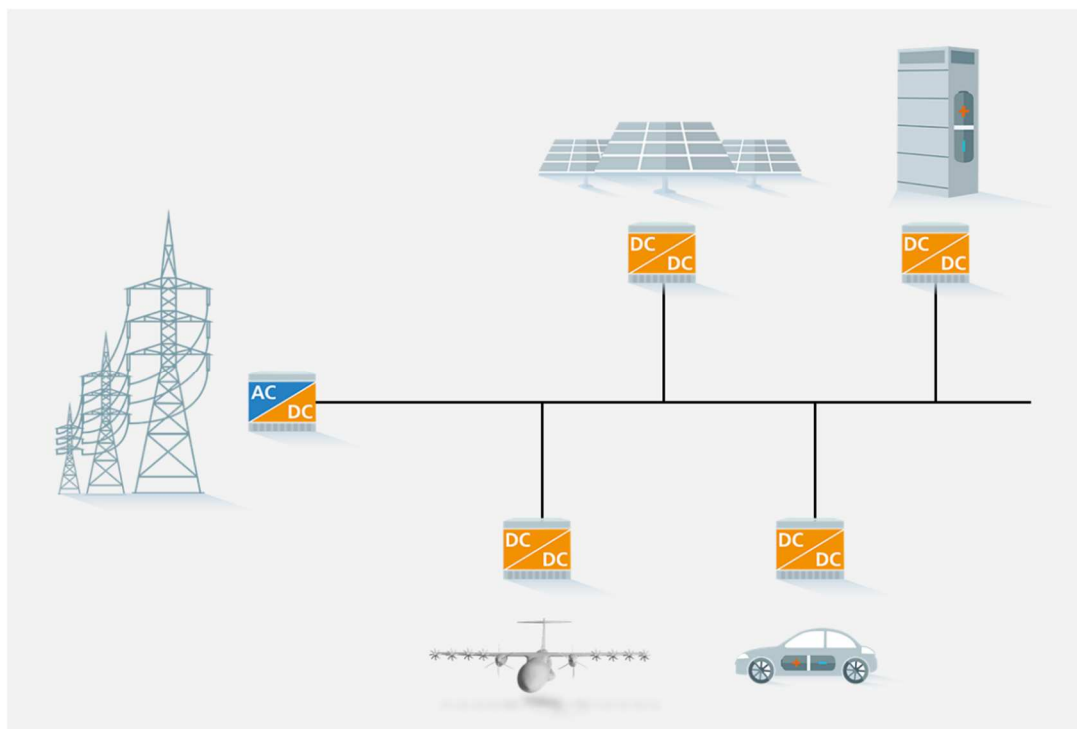


Figure 62. Basic principle of a DC based grid

Comparing those two basic principles, the AC-based approach benefits from being the currently established technology. Therefore, a large selection of installation components is available and technical staffs are trained for working with standard grids. However, from a technical perspective, the DC approach has multiple benefits. The integration of additional battery storage units and photovoltaic systems is simplified. The AC/DC or DC/AC conversation stages for all DC-based devices are eliminated. Therefore, the number of conversation stages between local battery storage, photovoltaic generators, and consumers (e.g. DC chargers) are minimized. This increases system efficiency and decreases complexity. Additionally, DC-connected systems are easier to control than AC-connected systems [102]. There is also an advantage regarding the power distribution cables. In an AC system, a four-wire setup for the power distribution network is used. As such, the transported power results in:

$$P_{AC} = \sqrt{3} \cdot U_{peak} \cdot I_{eff} \cdot \cos(\varphi)$$

With I_{eff} the effective current, U_{peak} the peak voltage and $\cos(\varphi)$ the power factor. Using the same four-wire setup for a DC system with two wires used for positive and negative respectively, the maximum current per wire matches the effective AC current not to overload the conductor. For AC systems, the insulation is rated for the peak voltage. As such, the nominal voltage in a DC system can be U_{peak} and the power in a four-wire DC system results in:

$$P_{DC} = 2 \cdot U_{peak} \cdot I_{eff}$$

Comparing the DC and AC power results in:

$$\frac{P_{DC}}{P_{AC}} = \frac{2 \cdot U_{peak} \cdot I_{eff}}{\sqrt{3} \cdot U_{peak} \cdot I_{eff} \cdot \cos(\varphi)} = \frac{2}{\sqrt{3} \cdot \cos(\varphi)}$$

Even with the assumption of a power factor $\cos(\varphi)$ of 1, the same wire system can transport about 15 percent higher power using a DC system. When using the reciprocal, the required copper cross-section of the wire system for the same power can be reduced to approximately 85 percent.

AC/DC converters are usually built as a two-stage system: the first stage is the power factor compensation (PFC) needed to reduce reactive power and provides a stable DC link voltage. This supplies the second stage, a DC/DC converter, to establish the wanted DC output. In a DC system, the converter can be reduced to the second stage, and as such, the volume, weight, and costs can be reduced. In addition, the converter efficiency can be raised, as the rectifying stage adds no more losses. Figure 63 shows a power supply with the PFC stage highlighted in red. With additional benefits in control design and resilience, selecting the basic technology of an innovative on-ground energy supply falls to a DC system.

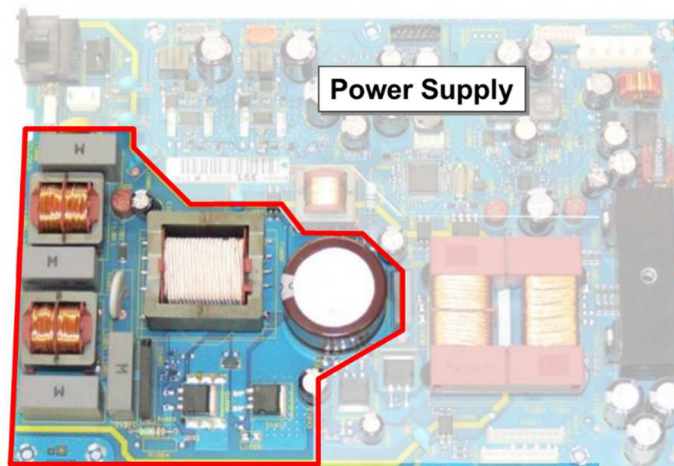


Figure 63. Power supply with highlighted rectifying stage

7.3. Dimensioning of charging converters

For the further design of the energy supply system, the single components need to be dimensioned first. There is a wide variety of airfield support vehicles that prevents from dimensioning chargers for each type specifically. The limits of the combined charging system (CCS) standard for electric vehicles should be used as a reference. The CCS is the preferred charging standard used in Europe and Northern America. It currently allows charging with up to 350 kW and a maximum voltage of 1000 V. For the short-term analysis, it is a reasonable estimate that market-available DC fast chargers will suffice to charge any airfield support vehicle to 80 % state-of-charge (SoC) within half an hour.

For the aircraft charger, the WP2 battery design is taken into consideration. The parameters of the battery are summarized in Table 56. A battery configuration of 317 cells in series and 11 cells in parallel is considered for the system level.

Table 56 Electrical parameters of the aircraft battery system

Parameter	Cell level	System level
Upper voltage limit	4.2 V	1331.4 V
Nominal voltage level	3.7 V	1172.9 V
Lower voltage limit	3.0 V	951.0 V
Capacity	30 Ah	390 kWh
Charging current	30 A (1C), 60 A (2C)	330 A (1C), 660 A (2C)

The battery's voltage limits set the output range of the charger, while the 2C rate defines the maximum output current. Therefore, a DC fast-charging station with a power of 780 kW is needed. The aircraft has two identically 390 kWh battery packs. Therefore, two DC fast-charging stations per aircraft are needed. Overall, the charging requirements and the size of the battery pack are comparable to battery-electric trucks, like the Tesla Semi. A new charging standard, called "Megawatt Charging System" (MCS), for high power charging of commercial vehicles is under development by CharIN (Charging Interface Initiative e.V). The maximum charging power will be 3.75 MW with a voltage limit of 1250 V and a current limit of 3000 A [103]. The MCS standard will meet the charging requirements for the aircraft in the GENESIS project for all time horizons.

Due to safety concerns, a galvanically isolated charger has to be used. While there are currently no standards that would prevent using non-isolated converters, the application is comparable to the current standards for road vehicles. Each charging point needs to be isolated from the next due to safety concerns. For the short-term analysis, unidirectional power flow (charging of the aircraft) is sufficient but should be investigated again for the mid- and long-term analyses.

Due to the high power demand, building a modular charging system with single modules in the < 100 kW range is recommended to reduce the strain on single components. Using the same modules but with a different total number for the aircraft charger and the other chargers for airfield support vehicles is viable. Topology-wise, the power requirement alone disqualifies simple switching converter topologies, like the Flyback converter, since they would require bulky transformer and filter components. In order to utilize the entire operating range of the transformer and reduce the strain on the semiconductors, a full bridge topology should be used on the primary side. The most common topologies resulting from that would be the Dual-Active-Bridge (DAB) and the resonant LLC converter in full-bridge implementation, as shown in Figure 64 and Figure 65.

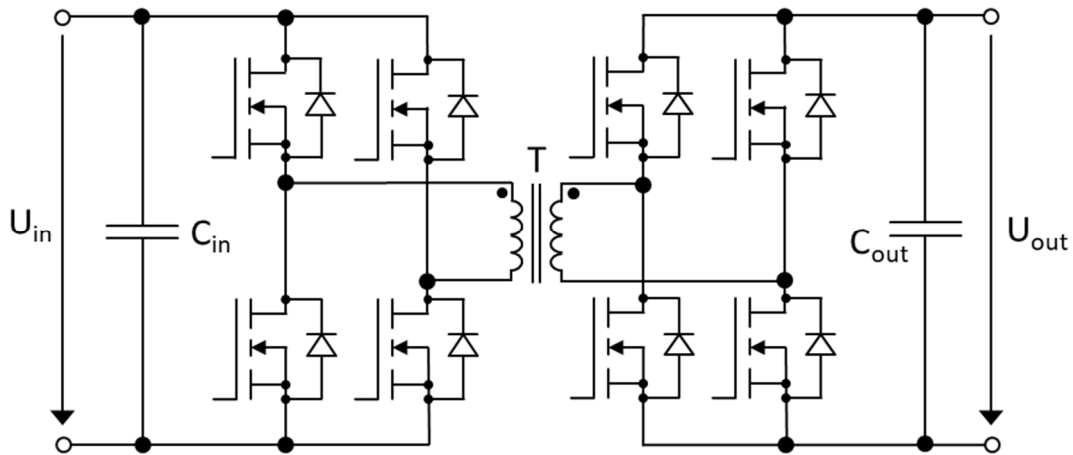


Figure 64. Dual-Active-Bridge converter

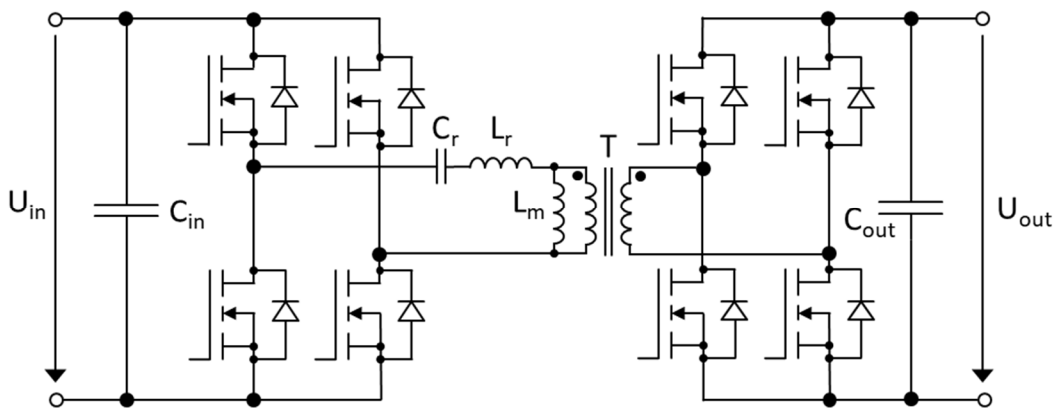


Figure 65. LLC resonant converter

As it can be seen, the primary switching circuits are the same, but the transformer path is different. With both topologies, ZVS (Zero-Voltage-Switching) and ZCS (Zero-Current-Switching) can be achieved to increase the switching frequency, optimize the magnetic components, and increase the efficiency. The LLC offers a very good EMC behavior and high efficiency at its nominal operating point, but its efficiency falls considerably outside the nominal area. The efficiency of the DAB is high over a broader operating area, although it does not meet the peak efficiency and the EMC performance of the LLC. Depending on the modularization, both topologies can be used for realizing the charging systems.

7.4. Grid Topology

For this application, multiple grid topologies are possible. The four most sensible solutions are depicted in Figure 66. The tree structure is a more classical approach found in most installations as it offers a hierarchical structure, which simplifies the selectivity of safety elements. The bus structure offers a straightforward solution with low installation costs but has drawbacks in larger grids, and safety considerations are more complex. The ring structure reduces cabling losses and offers a higher resilience but requires higher planning efforts, especially for the safety elements. Finally, the zonal structured ring provides the most increased resilience of all four grid topologies, reduces distribution losses the most, but has the highest costs and efforts in planning and installation.

The on-ground energy supply has a high potential for large distributed photovoltaic energy generation. As such, the tree structure is not beneficial since its top-down hierarchy is usually a

supply-load hierarchy and because distributed energy generation works against the main benefit of simplified selectivity. The bus structure shows its main drawbacks with the large expansiveness and high power demand, resulting in significant distribution losses. As such, this is also not recommended.

The ring topology reduces those losses and works better with distributed generation than the tree structure. Still, the aircraft charging systems have a high power demand compared with other consumers. Even with the maximum voltage of 1500 V, defined in the low voltage directive 2014/35/EU, currents are above 500 A and, thus, large cabling diameters are required. Therefore, it is reasonable to set up battery storage systems close to the aircraft chargers to reduce the strain on the distribution grid during peak charging. Depending on the local layout of the airport and the location of photovoltaic plants, the additional benefits of a zonal structured ring may justify the extra planning and installation costs.

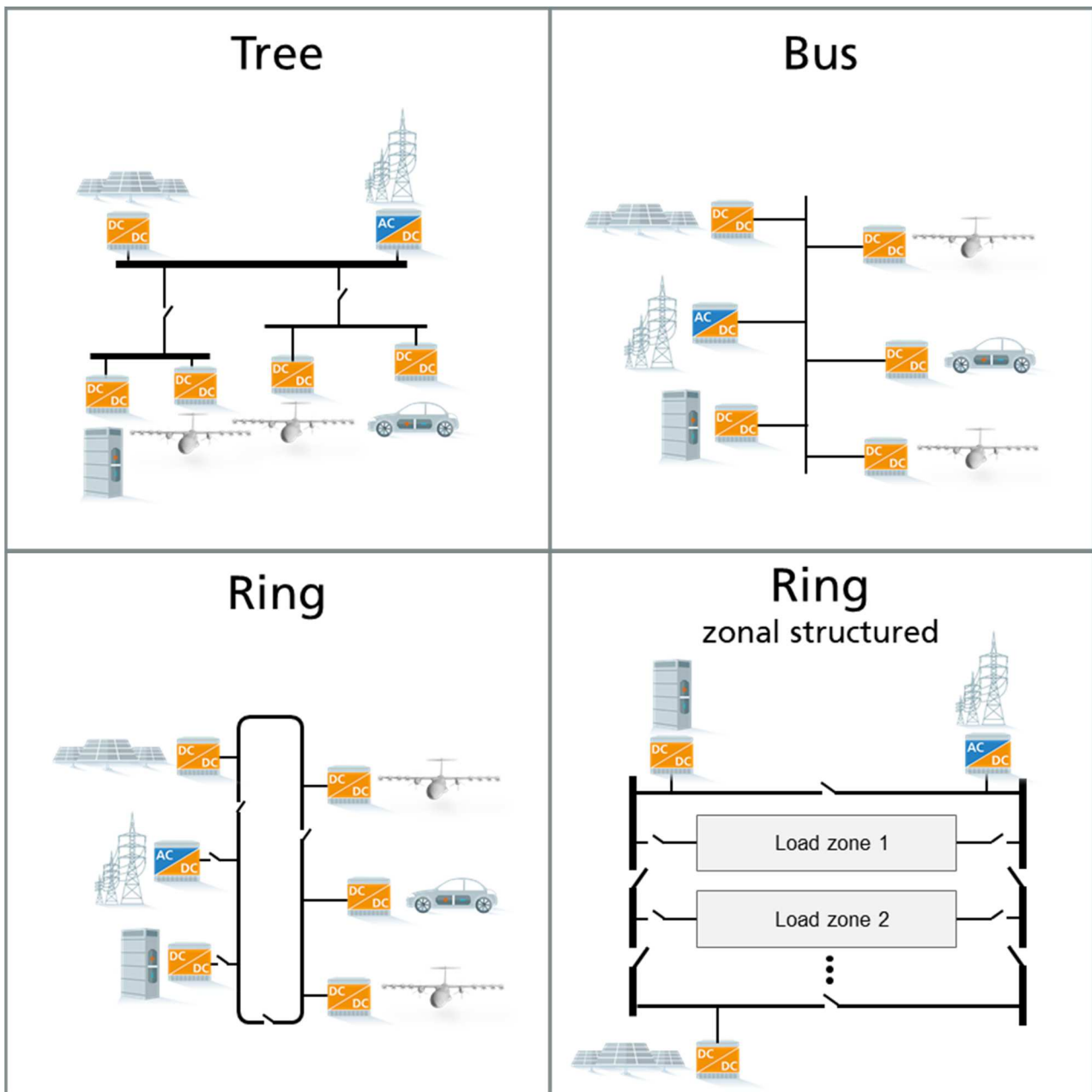


Figure 66. Overview grid topologies

8. Conclusions and outlook

The previous chapters presented the short-term (2025-2035) technology foresight analysis for the powertrain components, energy storage, and on-ground energy supply. Each chapter of the deliverable was dedicated to one specific task and key element in the aircraft system (batteries, fuel cells, gas turbines, power electronics, electric drives, and on-ground infrastructures).

Li-ion batteries with nickel manganese cobalt oxide chemistry are the primary solution for the battery technology. The energy density is expected to rise from 280 Wh/kg in 2025 to 400 Wh/kg in 2035, allowing a significant weight reduction over the years. However, that is lower than the needed energy density of 600 Wh/kg for a fully electric aircraft in the regional class. Therefore, a hybrid electric solution with a gas turbine is needed for the short-term perspective.

Solid oxide fuel cells and polymer electrolyte membrane fuel cells are the two most promising candidates for the fuel cell technology. However, with a power density of 0.86 kW/kg, they lay below the minimum value of 2 kW/kg at which fuel cells can be utilized for an aircraft application. Fuel cell technology is not ready yet and will not be incorporated for the short-term analysis. Furthermore, the required hydrogen storage will also add a mass penalty for the tank (e.g., 2.15 tons for 150 kg of gaseous hydrogen) to the aircraft. In this regard, different hydrogen storage possibilities in the gaseous, liquid, and solid state have been discussed.

A surrogate model for a gas turbine engine for the short-term scenario with performance, emissions, weight, main dimensions, and cost evaluation was provided. Validation of the model has been provided. Additionally, the consequences of using different biofuel blending ratios have been investigated.

For the power electronics converters, the motor traction drive inverter, generator traction drive inverter, bidirectional battery DC/DC converter, fuel cell DC/DC converter, DC/AC grid converter, and isolated DC/DC converter for low voltage supply have been investigated in detail. For each converter type, the efficiency and power density values were determined. The choice of the HV DC bus voltage and power semiconductors was discussed. The voltage was set to 800 V and it was illustrated that silicon carbide wide-bandgap power semiconductors should be used for all power electronics converters.

For electric drives, different types of AC machines have been compared with the result that the permanent magnet synchronous machine is the best option for the short-term horizon. Furthermore, a possible design of the primary and secondary electric machines has been presented.

Finally, the possibilities of the on-ground energy supply, focusing on the electric on-ground energy supply and ultra-fast DC charging stations, were described. It is recommended to use a DC-based distribution grid in a (zonal structured) ring topology. The DC ultra-fast chargers need to provide a maximum output power of 780 kW, and they should be built with silicon carbide-based building blocks of 100 kW power. Table 57 summarizes the recommended main technologies for all key technology components for the short-term perspective.

Table 57. Summary of the main recommended technologies for the short-term perspective

Key technology components	Recommended main technologies for the short-term perspective	Main technical parameters and values
Batteries (Task 2.1)	Li-ion with nickel manganese cobalt oxide (NMC) chemistry	Energy density: 280 Wh/kg in 2025 to 400 Wh/kg in 2035
Fuel cells (Task 2.2)	None (power density too low)	Actual power density: 0.86 kW/kg Needed power density: > 2 kW/kg
Gas turbines (Task 2.3)	Conventional gas turbine sized according to the application with usage of up to 100 % biofuel	Fuel consumption: 0.23 kg/(kW*h) Dry mass: 285 kg Maximum diameter: 608 mm
Power electronics converters (Task 2.4)	Silicon carbide (SiC) power semiconductors, foil capacitors, multi-phase/interleaved topologies	HV DC bus voltage: 800 V Inverter efficiency: ≈ 99 % Inverter power density: 63 kW/kg
Electric drives (Task 2.5)	Multiphase permanent magnet synchronous machine (PMSM) with hairpin winding	Efficiency: ≈ 96 % Total power density: 6.4 kW/kg Mass for 600 kW motor: 86.5 kg
On-ground infrastructure (Task 2.6)	DC-based distribution grid in a (zonal structured) ring topology, silicon carbide-based DC fast charges	DC charging power: 2x 780 kW

Figure 67 shows the GENESIS activities and the time plan of the project. The technology foresight analysis for the short-term perspective has been finished in M10 with this deliverable D2.1. It highlights knowledge gaps, technological challenges, and potential solutions to meet 50 passenger regional aircraft requirements. The analyses will feed back into the aircraft conceptual design for potential refinements. They will also serve as inputs for the generation of LCI data (materials extraction, production, use, recycling, and disposal) and economic evaluation. The technology foresight analysis for the medium-term perspective (2035-2045) will be presented in the following deliverable D2.2 in M16.

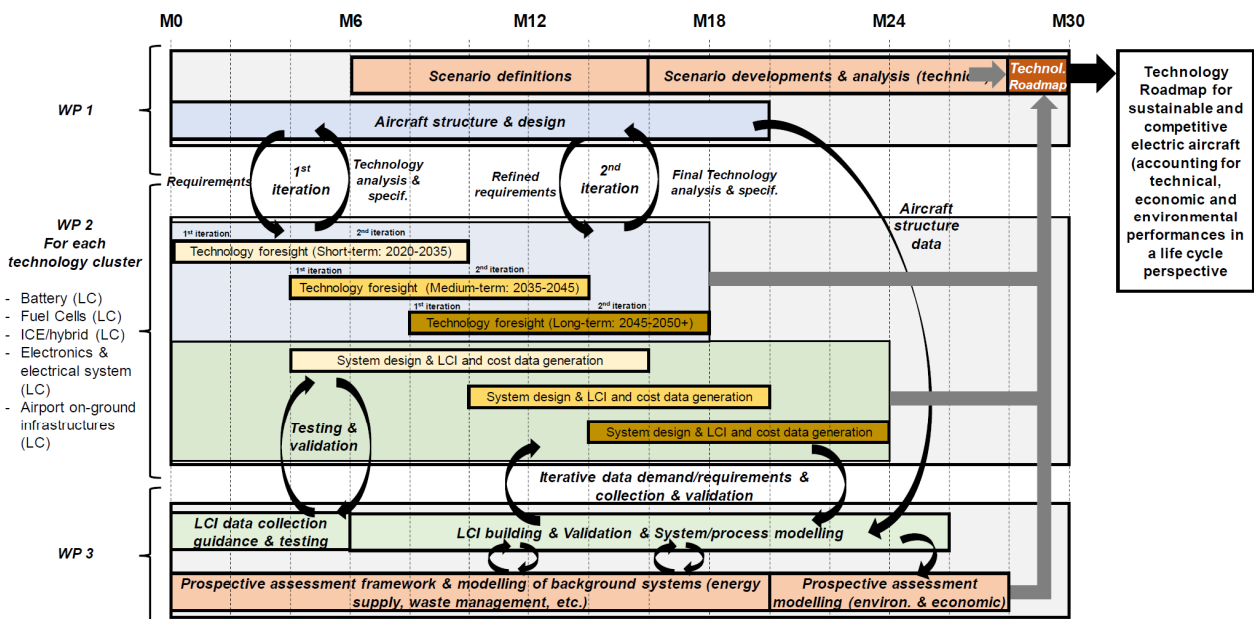


Figure 67. GENESIS activities and time plan

9. References

- [1] M. Ruocco, M. Di Stasio, V. Marciello, S. Corcione, F. Orefice and F. Nicolosi, "GENESIS Deliverable D1.1 - Overall Requirements for (hybrid) electric 50 pax regional class A/C," CLEAN SKY 2 JTI-CS2-2020-CFP11-THT-13, Naples, 2021.
- [2] Y. Gibbs, "X-57 Maxwell - Electric Propulsion Airplane," 7 August 2017. [Online]. Available: https://www.nasa.gov/centers/armstrong/multimedia/imagegallery/electric_propulsion_aircraft/X-57_maxwell_water.html. [Accessed 15 November 2021].
- [3] J. Dahl, "Jet engine.svg CC BY-SA 4.0," <<https://creativecommons.org/licenses/by-sa/4.0/>>, via Wikimedia Commons, 2007.
- [4] N. Nitta, F. Wu, J. T. Lee and G. Yushin, "Li-ion battery materials: present and future," *Materials Today*, vol. 18, 2015.
- [5] "Impact climatique du transport aérien," Wikipedia, 2021. [Online]. Available: https://fr.wikipedia.org/wiki/Impact_climatique_du_transport_a%C3%A9rien#%C3%89missions_de_CO2.
- [6] J. Van Bogaert, "Assessment of Potential Fuel Saving Benefits of Hybrid-Electric Regional Aircraft," TU Delft, 2015.
- [7] A. W. Schäfer et al., "Technological, economic and environmental prospects of all electric aircraft," *Nature Energy*, p. 160–166, 2018.
- [8] A. Bills, S. Sripad, W. L. Fredericks, M. Singh and V. Viswanathan, "Performance Metrics Required of Next-Generation Batteries to Electrify Commercial Aircraft," *American Chemical Society Energy Letters*, pp. 663-668, 2020.
- [9] T. Kim, W. Song, D.-Y. Son and L. K. Ono, "Lithium-ion batteries: outlook on present, future, and hybridized technologies," *Journal of Materials Chemistry*, vol. 7, 2019.
- [10] "BU-216: Summary Table of Lithium-based Batteries," Battery University, 25 October 2021. [Online]. Available: <https://batteryuniversity.com/article/bu-216-summary-table-of-lithium-based-batteries>.
- [11] "Lithium-ion batteries," Panasonic, [Online]. Available: <https://eu.industrial.panasonic.com/products/batteries-energy-products/secondary-batteries-rechargeable-batteries/lithium-ion-batteries/series/cylindrical-type/ACI4001?reset=1>.
- [12] R. Lindsay, "Additional Data Center Applications for Lithium-Ion Batteries," August 2018. [Online]. Available: <https://datacenterfrontier.com/data-center-lithium-ion-batteries/>.
- [13] "Lithium cells: differences, uses and how to choose the best ones," Flash Battery, 23 January 2020. [Online]. Available: <https://www.flashbattery.tech/en/cells-lithium-batteries-industrial/>.
- [14] C. Randall, "Panasonic presents prototype 4680 cells," 2021. [Online]. Available: <https://www.electrive.com/2021/10/26/panasonic-presents-prototype-4680-cells/>.
- [15] Y. Miao, P. Hynan, A. von Jouanne and A. Yokochi, "Current Li-Ion Battery Technologies in Electric Vehicles and Opportunities for Advancements," *Energies*, vol. 12, 2019.
- [16] M.F.R. Zwicker et al., "Automotive battery pack manufacturing – a review of battery to tab joining," *Journal of Advanced Joining Processes*, 2020.
- [17] P. Lima, "Simple solution for safer, cheaper and more energy-dense batteries," 12 04 2020. [Online]. Available: <https://pushevs.com/2020/04/12/simple-solution-for-safer-cheaper-more-energy-dense-batteries/>.

- [18] X. Meng, "The Next-Generation Battery Pack Design: from the BYD Blade Cell to Module-Free Battery Pack," 31 Oct 2020. [Online]. Available: <https://medium.com/batterybits/the-next-generation-battery-pack-design-from-the-byd-blade-cell-to-module-free-battery-pack-2b507d4746d1>.
- [19] K. Edström and S. Perraud, "Inventing the sustainable batteries of the future," BATTERY 2030+ Roadmap, 2020.
- [20] P. Molloy, "Run on Less with Hydrogen Fuel Cells," RMI, October 2019. [Online]. Available: <https://rmi.org/run-on-less-with-hydrogen-fuel-cells/>.
- [21] R. S. Khurmi, Materials Science, S.Chand & Company Ltd, 2014.
- [22] X. Ren et al., "Current progress of Pt and Pt-based electrocatalysts used for fuel cells," *Sustainable Energy & Fuels*, vol. 4, pp. 15-30, 2020.
- [23] D. Akinyele, E. Olabode and A. Amole, "Review of Fuel Cell Technologies and Applications," *Inventions*, vol. 5, 2020.
- [24] L. Giorgi, "Fuel cells: Technologies and Applications," *Open Fuel Cells Journal*, vol. 6, 2013.
- [25] K.A. Adamson, Stationary Fuel Cells, Amsterdam: Elsevier Science, 2007.
- [26] Y. Haseli, "Maximum conversion efficiency of hydrogen fuel cells," *International Journal of Hydrogen Energy*, pp. 9015-9021, May 2018.
- [27] J. C. Ho et al., "Technological barriers and research trends in fuel cell technologies: A citation network analysis," *Technological Forecasting & Social Change*, vol. 82, pp. 66-79, 2014.
- [28] R. J. Braun, M. Gummalla, and J. Yamanis, „System Architectures for Solid Oxide Fuel Cell-Based Auxiliary Power Units in Future Commercial Aircraft Applications,“ *Journal Fuel Cell Science and Technology*, 2009.
- [29] S. Porstmann, T. Wannemacher and T. Richter, "Overcoming the Challenges for a Mass Manufacturing Machine for the Assembly of PEMFC Stacks," *Machines*, p. 66, October 2019.
- [30] S.Porstmann, T.Wannemacher and W.-G.Drossel, "A comprehensive comparison of state-of-the-art manufacturing methods for fuel cell bipolar plates including anticipated future industry trends," *Journal of Manufacturing Processes*, vol. 60, pp. 366-383, December 2020.
- [31] B. Eska and M. Corneille, "Planning guideline for fuel cell back-up power supplies - Uninterruptible Power Supply (UPS) and Emergency Power Systems (EPS) with fuel cells," 2018. [Online]. Available: <http://www.cleanpowernet.de/wp-content/uploads/2019/03/Planning-Guideline-UPS-and-EPS-with-Fuel-Cells.pdf>.
- [32] "Fuel Cell Guide - Alkaline Fuel Cells," Fuelcell.co.uk., [Online]. Available: <http://www.fuelcell.co.uk/alkaline-fuel-cells/>.
- [33] S. Sabihuddin, A.E Kiprakis snf M. Mueller, "A numerical and graphical review of energy storage technologies," *Energies*, vol. 8, pp. 172-216, 2015.
- [34] X. Li, Fuel cells, Boca Raton, FL, USA., 2017.
- [35] A. Kirubakaran, S. Jain and R.K. Nema, "A review on fuel cell technologies and power electronic interface," *Renew. Sustain. Energy Rev*, vol. 13, pp. 2430-2440, 2009.
- [36] Deloitte and Ballard, "Fueling the Future of Mobility: Hydrogen and fuel cell solutions for transportation," 2020.
- [37] "Hyundai NEXO," [Online]. Available: <https://www.hyundai.com/worldwide/en/eco/nexo/because-of-you>. [Accessed 17 October 2021].

- [38] "Alstom unveils Coradia iLint hydrogen fuel cell powered train for European regional market," *Fuel Cells Bulletin*, no. 9, 2016.
- [39] C. Spiegel, "Stationary Fuel Cell Power Applications," 10 08 2019. [Online]. Available: <https://www.fuelcellstore.com/blog-section/stationary-fuel-cell-power-applications>.
- [40] E. Padgett and G. Kleen, "Automotive Fuel Cell Targets and Status," DOE Hydrogen and Fuel Cells Program Record, 2020.
- [41] Ministry of ecology, energy, sustainable development and town and country planning, "Accidentology involving hydrogen," 2009. [Online]. Available: https://www.aria.developpement-durable.gouv.fr/wp-content/files_mf/SY_hydrogen_GB_2009.pdf.
- [42] G. Pourcelly, „Stockage de l'hydrogène, Piles à combustible,“ Paris, 2013.
- [43] M. Legault, "The first commercial Type V composite pressure vessel," *Composites World*, 2012. [Online]. Available: <https://www.compositesworld.com/articles/next-generation-pressure-vessels>. [Accessed 2021 October 15].
- [44] H. Barthélémy, "Hydrogen Storage – Industrial Prospectives," Air Liquide, Paris.
- [45] Y. Su, H. Lv, W. Zhou, and C. Zhang, "Review of the Hydrogen Permeability of the Liner material of Type IV On-Board Hydrogen storage Tank," *World Electric Vehicle Journal*, no. 12, p. 130, 2021.
- [46] Office of Energy Efficiency & Renewable Energy, "Hydrogen storage," [Online]. Available: <https://www.energy.gov/eere/fuelcells/hydrogen-storage>. [Accessed 22 10 2021].
- [47] Office of Energy Efficiency & Renewable Energy, "Liquid Hydrogen Delivery," [Online]. Available: <https://www.energy.gov/eere/fuelcells/liquid-hydrogen-delivery>. [Accessed 25 10 2021].
- [48] E. Rivard, M. Trudeau and K. Zaghbi, "Hydrogen Storage for Mobility: A Review," Quebec, 2019.
- [49] Kawasaki Heavy Industries, Ltd, "Technologies of hydrogen liquefaction, transport and storage - paving the way to a hydrogen fueled future," *Kawasaki Technical Review*, no. 176, pp. 52-58, 2016.
- [50] Linde, "Liquid hydrogen distribution technology," Brussels, 2019.
- [51] K. Kunze and O. Kircher, "Cryo-Compressed Hydrogen Storage," Oxford, 2012.
- [52] R. Rhodes, "Explosive lessons in hydrogen," *Ask magazine*, pp. 46-50.
- [53] College of the Desert, "Hydrogen Fuel Cell Engines and Related Technologies," 2001.
- [54] M. Dornheim, "Thermodynamics of Metal Hydrides: Tailoring Reaction Enthalpies of Hydrogen," *Thermodynamics - Interaction Studies - Solids, Liquids and Gases*, 2011.
- [55] [Online]. Available: https://en.wikipedia.org/wiki/ATR_42. [Accessed 18 October 2021].
- [56] [Online]. Available: <https://www.pwc.ca/en/products-and-services/products/regional-aviation-engines/pw100-150>. [Accessed 18 October 2021].
- [57] [Online]. Available: https://www.mitma.gob.es/recursos_mfom/comodin/recursos/in-052-2019_final_report_nm2.pdf. [Accessed 18 October 2021].
- [58] M. Daly, Jane's Aero Engines, Jane's Information Group, 2002.
- [59] [Online]. Available: <https://www.aerocontact.com/en/virtual-aviation-exhibition/catalog/77-atr-42-500-brochure#lg=1&slide=0>. [Accessed 18 October 2021].
- [60] [Online]. Available: <https://www.easa.europa.eu/sites/default/files/dfu/EASA%20IM.E.041%20TCDS%20Issue%204.pdf>. [Accessed 21 October 2021].

- [61] E. Hosking, D.P. Kenny, R.I. McCormick, S.H. Moustapha, P. Sampath and A.A. Smailys, "The PW100 Engine: 20 Years of Gas Turbine Technology Evolution," in *RTO AVT Symposium*, 1198.
- [62] [Online]. Available: <https://www.gasturb.de/index.php>. [Accessed 18 October 2021].
- [63] H. Grieb, *Projektierung von Turboflugtriebwerken*, Basel: Springer, 2004.
- [64] P. Walsh and P.P. Fletcher, *Gas Turbine Performance* 2nd edition, Blackwell Science, 1998.
- [65] J. Gauntner, "Algorithm for calculating turbine cooling flow and the resulting decrease in turbine efficiency," in *NASA Technical Memorandum*, 1980.
- [66] F. Yin and A. Gangoli Rao, "Performance analysis of an aero engine with inter-stage turbine burner," in *Aeronautical Journal*, 2017.
- [67] K.G. Kyprianidis, *Future Aero Engine Designs: An Evolving Vision*, IntechOpen, 2011.
- [68] J. Mattingly, H. Heiser and T. Pratt, *Aircraft engine design* 2nd edition, AIAA, 2002.
- [69] E. Torenbeek, *Synthesis of Subsonic Airplane Design*, Springer, 1982.
- [70] S. Gudmundsson, *General Aviation Aircraft Design*, Butterworth-Heinemann, 2013.
- [71] [Online]. Available: <https://www.jet-engine.net/>. [Accessed 18 October 2021].
- [72] O. Younossi, M.V. Arena, R.M. Moore, M. Lorell, J. Mason and J.C. Graser, *Military Jet Engine Acquisition: Technology Basics and Cost-Estimating Methodology*, RAND, 2002.
- [73] J. Kurzke, *GasTurb 11: Design and Off-Design Performance of Gas Turbines*, GasTurb GmbH., 2007.
- [74] A. Filippone and N. Bojdo, "Statistical model for gas turbine engines exhaust emissions," in *Transportation Research*, 2018.
- [75] [Online]. Available: <https://www.easa.europa.eu/domains/environment/icao-aircraft-engine-emissions-databank>. [Accessed 20 October 2021].
- [76] [Online]. Available: [24] <https://www.eurocontrol.int/publication/forecasting-civil-aviation-fuel-burn-and-emissions-europe-interim-report>. [Accessed 20 October 2021].
- [77] F. Wolters, R.-G. Becker and M. Schaefer, "Impact of alternative fuels on engine performance and CO₂-emissions," in *ICAS 2012*, 2012.
- [78] C. Bayona-Roa, J.S. Solis-Chaves, J. Bonilla, A.G. Rodriguez-Melendez and D. Castellanos, "Computational simulation of PT6A gas turbine engine operating with different blends of biodiesel: A transient-response analysis," in *Energies*, 2019.
- [79] [Online]. Available: <https://aviationbenefits.org/environmental-efficiency/climate-action/sustainable-aviation-fuel/producing-sustainable-aviation-fuel/>. [Accessed 20 October 2021].
- [80] [Online]. Available: [https://www.europarl.europa.eu/RegData/etudes/BRIE/2020/659361/EPRS_BRI\(2020\)659361_EN.pdf](https://www.europarl.europa.eu/RegData/etudes/BRIE/2020/659361/EPRS_BRI(2020)659361_EN.pdf). [Accessed 20 October 2021].
- [81] Forecast International, *The Market for Aviation Turboprop Engines: 2010-2019*, Forecast International, 2010.
- [82] A.J.B. Jackson, "Optimization of Aero and Industrial Gas Turbine Design for the Environment," Cranfield University, 2009.
- [83] [Online]. Available: <https://it.mathworks.com/help/stats/regression-learner-app.html>. [Accessed 27 October 2021].
- [84] R. Weiss, "Coordination of insulation," Semikron Application Note AN1405, Nürnberg, 2017.

- [85] M. Filipenko, S. Biser, M. Boll, M. Corduan, M. Noe, and P. Rostek, "Comparative Analysis and Optimization of Technical and Weight Parameters of Turbo-Electric Propulsion Systems," *Aerospace*, vol. 7, no. 8, p. 107, 27 July 2020.
- [86] C. Felgemacher, S. V. Araújo, P. Zacharias, K. Neemann and A. Gruber, "Cosmic radiation ruggedness of Si and SiC power semiconductors," in *28th International Symposium on Power Semiconductor Devices and ICs*, Prague, 2016.
- [87] S. Dixon-Warren, "TechInsights," 31 October 2019. [Online]. Available: <https://www.techinsights.com/blog/evolution-sic-mosfet-technology-retrospective>.
- [88] S. Davis, "Power Electronics," 1 März 2010. [Online]. Available: <https://www.powerselectronics.com/technologies/discrete-power-semis/article/21857697/enhancement-mode-gallium-nitride-mosfet-delivers-impressive-performance>. [Accessed 15 October 2021].
- [89] E. Dogmus, A. B. Slimane and P. Chiu, "Power SiC Materials, Devices and Applications," Yole Development, 2020.
- [90] A. B. Slimane and P. Chiu, "GaN Power 2021: Epitaxy, Devices, Applications and Technology Trends report," Yole Development, 2021.
- [91] L. Han, L. Liang, Y. Kang and Y. Qiu, "A Review of SiC IGBT: Models, Fabrications, Characteristics, and Applications," *IEEE Transactions on Power Electronics*, vol. 36, no. 2, pp. 2080-2093, 30 June 2020.
- [92] A. Wintrich, U. Nicolai, W. Tursky and T. Reimann, Application Manual Power Semiconductors, Nürnberg: SEMIKRON International GmbH, 2015, p. 465.
- [93] B. Basler, T. Greiner and P. Heidrich, "Reduction of DC link capacitor stress for double three-phase drive unit through shifted control and phase displacement," in *11th International Conference on Power Electronics and Drive Systems*, Sydney, 2015.
- [94] M. Vujacic, O. Dordevic and G. Grandi, "Evaluation of DC-Link Voltage Switching Ripple in Multiphase PWM Voltage Source Inverters," in *IEEE Transactions on Power Electronics*, 2019.
- [95] J. W. Kolar, T. M. Wolbank and M. Schrod, "Analytical calculation of the RMS current stress on the DC link capacitor of voltage DC link PWM converter systems," in *Ninth International Conference on Electrical Machines and Drives*, Canterbury, UK, 1999.
- [96] "600 kW XM3 High Performance Dual Three-Phase Inverter," [Online]. Available: <https://www.wolfspeed.com/products/power/reference-designs/crd600da12e-xm3>. [Accessed 21 October 2021].
- [97] G. Grandi and J. Loncarski, "Evaluation of current ripple amplitude in three-phase PWM voltage source inverters," in *2013 International Conference-Workshop Compatibility And Power Electronics*, Ljubljana, Slovenia, 2013.
- [98] R. N. Beres, X. Wang, M. Liserre, F. Blaabjerg and C. L. Bak, "A Review of Passive Power Filters for Three-Phase Grid-Connected Voltage-Source Converters," *IEEE Journal of Emerging and Selected Topics in Power Electronics*, vol. 4, no. 1, pp. 54-69, March 2016.
- [99] Y. Ting, "DC-DC Converters with a Wide Load Range and a Wide Input-Voltage Range," TU Delft, Delft, 2015.
- [100] C. Gillmor, "Comparison of PSFB and FB-LLC for high power DC/DC conversion," Texas Instruments, 2018.
- [101] C. Müller, U. Schwarzer, F. Qi, D. Scharfenstein and C. Weiss, Motor Handbook, Munich: Infineon, 2019.

- [102] S. Srdic and S. Lukic, "Toward Extreme Fast Charging: Challenges and Opportunities in Directly Connecting to Medium-Voltage Line, no. 1," *IEEE Electrification Magazine*, vol. 7, no. 1, pp. 22-31, 1 March 2019.
- [103] "Megawatt Charging System (MCS)," [Online]. Available: <https://www.charin.global/technology/mcs/>. [Accessed 18 November 2021].
- [104] E. Rivard, M. Trudeau and K. Zaghbi, "Hydrogen Storage for Mobility: A Review," *Functional Materials for Energy Conversion and Storage*, vol. 12, no. 12, 2019.